TU Delft

Delft University of Technology

Document Version
Final published version

Licence
CC BY-NC-ND

Citation (APA)
Huo, R. (2026). *High-throughput Super-resolution Microscopy Using Advanced Fluorescent Labels*. [Dissertation (TU Delft), Delft University of Technology]. https://doi.org/10.4233/uuid:911c13bd-417c-4351-8507-2dc2185dc3f5

Important note
To cite this publication, please use the final published version (if applicable).
Please check the document version above.

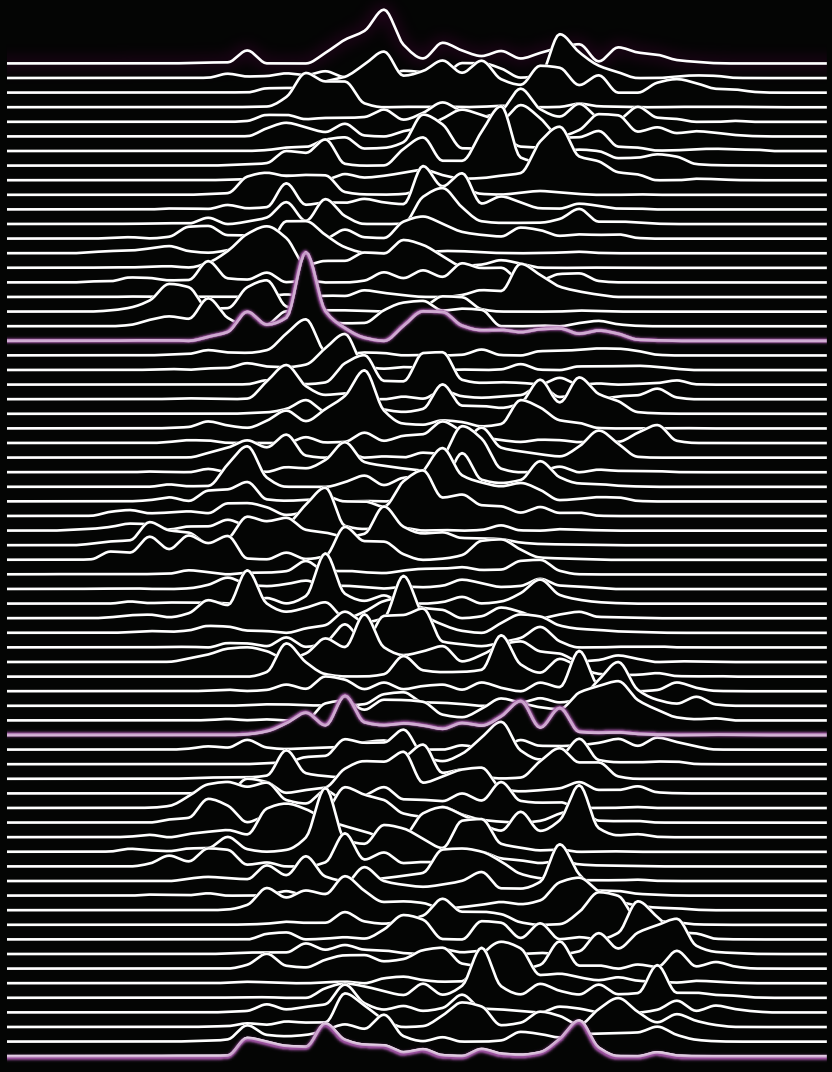
Copyright
In case the licence states “Dutch Copyright Act (Article 25fa)”, this publication was made available Green Open Access via the TU Delft Institutional Repository pursuant to Dutch Copyright Act (Article 25fa, the Taverne amendment). This provision does not affect copyright ownership.
Unless copyright is transferred by contract or statute, it remains with the copyright holder.

Sharing and reuse
Other than for strictly personal use, it is not permitted to download, forward or distribute the text or part of it, without the consent of the author(s) and/or copyright holder(s), unless the work is under an open content license such as Creative Commons.

Takedown policy
Please contact us and provide details if you believe this document breaches copyrights.
We will remove access to the work immediately and investigate your claim.

This work is downloaded from Delft University of Technology.

High-throughput Super-resolution Microscopy Using Advanced Fluorescent Labels



Ran Huo

High-throughput Super-resolution Microscopy Using Advanced Fluorescent Labels

Dissertation

for the purpose of obtaining the degree of doctor
at Delft University of Technology
by the authority of the Rector Magnificus, prof. dr. ir. H. Bijl,
chair of the Board for Doctorates
to be defended publicly on Wednesday 30 September 2026 at 10:00

by

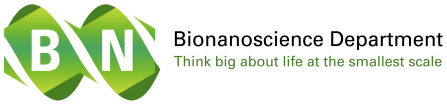
Ran HUO

This dissertation has been approved by the (co)promotors.

Composition of the doctoral committee:

Rector Magnificus,	chairperson
Prof. dr. C. Joo,	Promotor, Delft University of Technology
Dr. rer. nat. K.S. Grußmayer,	Copromotor, Delft University of Technology
Independent members:	
Prof. dr. J. Enderlein,	University of Göttingen, Germany
Prof. dr. rer. nat. J.C. Hohlbein,	Brandenburg University of Technology, Germany
Dr. K.A. Ganzinger,	AMOLF
Prof. dr. S. Stallinga,	Delft University of Technology
Reserve member:	
Prof. dr. J.P. Hoogenboom,	Delft University of Technology







Printed by: Proefschriftenprinten.nl

Cover design: Joyplot of temporal fluctuations in single molecule fluorescence on the front; mosaic of spatial detection of single molecule fluorescence on the back. Data and design by R. Huo.

Copyright © 2026 by R. Huo

ISBN 978-94-6518-424-1

An electronic copy of this dissertation is available at
https://repository.tudelft.nl/.

We see with a microscope,
but it is naïve to suggest that we see through a microscope.

Ian Hacking

Contents

1 Introduction **1**
1.1 Microscopic imaging: the ideal . . . 1
1.2 From blinking to fluctuation: single molecule microscopy . . . 2
1.3 Blinking strategy of fluorescent labels . . . 4
1.4 Current challenges of single molecule microscopy . . . 7
1.5 Outline . . . 9
References . . . 10

2 Open Blink: Low-cost TIRF Microscopy for Super-resolution Imaging **15**
2.1 Introduction . . . 16
2.2 Hardware design and performance . . . 17
2.2.1 Quad-line homogeneous high-power laser combiner . . . 17
2.2.2 Home-built TIRF microscope body with large FOV and dual-channel detection . . . 20
2.2.3 Active focus stabilization . . . 24
2.3 Control software development . . . 24
2.3.1 Microscope control scheme . . . 24
2.3.2 μManager integration . . . 25
2.4 Verification with single molecule super-resolution imaging . . . 27
2.5 Discussion . . . 27
2.6 Materials and Methods . . . 30
2.7 Data Availability . . . 33
2.8 Appendix . . . 34
References . . . 38

3 High-throughput Single Molecule Microscopy with Adaptable Resolution Using Exchangeable Oligonucleotide Labels **43**
3.1 Introduction . . . 44
3.2 High-resolution SOFI with oligonucleotide labels . . . 45
3.3 Acquisition time reduction with DNA-PAINT and SOFI . . . 48
3.4 High-throughput imaging with adaptive resolution . . . 49
3.5 Discussion . . . 52
3.6 Materials and Methods . . . 54
3.7 Data Availability . . . 60
3.8 Appendix . . . 60
References . . . 66

4 Rapid Sequence Selection by Parallel Kinetic Characterization of DNA Hybridization 71
4.1 Introduction . . . 72
4.2 Design of a single-molecule parallel DNA hybridization assay . . . 73
4.3 Parallel kinetic profiling of 128 DNA sequences . . . 73
4.4 Super-resolution imaging with an order of magnitude higher sampling rate 74
4.5 Discussion . . . 77
4.6 Methods and Materials . . . 77
4.7 Data Availability . . . 81
4.8 Appendix . . . 82
References . . . 86

5 Towards Multiplexed Live-cell Super-resolution Imaging with Enzymatic Labels 89
5.1 Introduction . . . 90
5.2 Characterization of self-labeling protein tags for SOFI . . . 92
5.2.1 Exchangeable HaloTag ligands (xHTLs) . . . 92
5.2.2 Spontaneously blinking HaloTag ligands . . . 93
5.2.3 Dual-color live-cell super-resolution combining xHTLs and SBFs . . 96
5.3 Roadmap to multiplexed live-cell imaging with SOFI . . . 96
5.4 Discussion . . . 98
5.5 Methods and Materials . . . 101
5.6 Data Availability . . . 107
5.7 Appendix . . . 108
References . . . 110

6 Discussion and Outlook 113
6.1 Balancing trade-offs in super-resolution microscopy: leverage biochemistry and technology . . . 113
6.2 Open microscopy as the platform for next-generation smart microscopy . . 116
6.3 Concluding remarks . . . 117
References . . . 117

Summary 121

Samenvatting 123

Epilogue 125

Acknowledgments 127

Curriculum Vitæ 129

List of Publications 131

1

Introduction

1.1. Microscopic imaging: the ideal

What is an ideal microscope? Since Antonie van Leeuwenhoek's first observation of living micro-organisms in 17th-century Delft, microscopy has been used as an extension of the human eye to look at life at the smallest scale [1, 2]. The building blocks of life, cells, crowded with various organelles and numerous biomolecules including proteins, DNAs and RNAs, reveal themselves under microscopes which have led biologists to extraordinary discoveries. An ideal microscope should, first and foremost, be able to resolve its target, spanning from Angstrom-scale molecules to micrometer-scale cells. Dynamism is one of the most prominent features of living organisms, and to capture the ever-changing cellular and sub-cellular processes ranging from mitosis over minutes or hours to protein diffusion within milliseconds requires a microscope with sufficient temporal resolution. Tissues, cells, organelles, and molecules are embedded in dense and complex environments, making high contrast and high signal-to-noise ratio crucial to distinguish them. Undoubtedly, one cannot truly understand life without studying it in its native, living state. While *in vitro* imaging provides plentiful insights, *in situ* and *in vivo* imaging is of irreplaceable value to observe life, ideally without intrusion or disturbance. Lastly, high-throughput screening, volumetric and multi-color imaging extend the reach of a microscope in different dimensions, supporting data-driven approaches such as smart microscopy, or applications such as drug discovery.

For more than a century, biologists benefit from fluorescence microscopy which remains still today one of the most powerful tools for biological and biomedical researches [3, 4]. With the abundant choices of fluorescent labels, such as fluorescent proteins, organic dyes, quantum dots, that can be adorned on the molecules of interests, fluorescence microscopy provides incomparable specificity and contrast for imaging. Imaging with light is deemed a relatively gentle approach to keep living organisms structurally intact as well. However, conventional fluorescence microscopy is at a distance from the ideal. Like all light microscopy techniques, the spatial resolution of fluorescence microscopy is dictated by the diffraction limit. Coined by Ernst Abbe in 1873, the image of an arbitrary point light source by a lens-based microscopy system is a blurry spot named Airy disk due to diffraction, described as the point spread function (PSF) [5]. Under the Rayleigh criterion, this translates to a limitation of spatial resolution

of approximately 300 nm when imaging with visible light, while most cellular structures are well below this size. Increasing the spatial resolution thus has driven microscopists for generations.

In the last three decades, various super-resolution microscopy (SRM) techniques bypassing the diffraction limit emerged. SRM techniques can be categorized loosely into three several groups: methods based on imaging scanning such as stimulated emission depletion (STED) and minimal fluorescence photon fluxes (MINFLUX) microscopy [6, 7]; methods with patterned excitation light source known as structure illumination microscopy (SIM) [8]; methods based on single molecules represented by single molecule localization microscopy (SMLM) and super-resolution fluctuation imaging (SOFI) [9–12]. While each method has its own strength and pushes the conventional fluorescence microscopy closer towards the ideal along its unique path, SMLM stands out for its high spatial resolution routinely achievable between 20 to 70 nm, with simple wide-field microscope configuration. It has become increasingly popular and has contributed to a large number of new biological discoveries. How far is SMLM from an ideal microscope?

1.2. From blinking to fluctuation: single molecule microscopy

In conventional wide-field fluorescence microscopy, all the fluorescent labels are excited at once, resulting in a blurred image consisting of overlapping PSFs. Single molecule localization microscopy (SMLM) exploits the photophysical properties of fluorescent labels in order to separate them temporally to achieve spatial sparsity. Instead of one single snapshot, SMLM requires an image stack with tens of thousands of image frames, where each frame contains only a small subset of distinguishable fluorescent labels. The PSF of each fluorescent label is fitted, for example, by a Gaussian function whose centroid is determined with sub-pixel precision. Repeating such process for all the labels in every image frame creates a list of coordinates indicating the locations of the fluorescently labeled molecules, which is used to reconstruct the final super-resolution image by superimposing all the localizations (Fig. 1.1). The limit of localization precision θ_{loc} of SMLM is estimated by the Cramer-Rao lower bound (CRLB), which depends on the photon number N and the standard deviation of the PSF θ_0 in its simplified form:

$$\theta_{\text{loc}} \geq \theta_0 / \sqrt{N} \tag{1.1}$$

The spatial resolution of SMLM is estimated as $R = 2.3 \times \theta_{\text{loc}}$, approximately 20 – 30 nm. Experimental results often do not reach as high due to background and camera readout noise, heterogeneous molecular orientation and distorted PSF.

The realization of SMLM relies on the stochastic and independent blinking of the fluorescent labels. The fluorescent emitters undergo cycles of fluorescent on- and off-states, where the off-time lasts thousands of times longer than the on-time, leading to the majority of the fluorophore population being in the dark off-states at a given time. Since the sparse density condition is at the core of SMLM, regulating the blinking kinetics of fluorescent labels remains the focus in SMLM implementations. Tight control over the duty cycle of the blinking fluorescent labels, defined by the ratio of on-time over the total of on-time and off-time, is necessary to achieve the sparse condition and to ensure sufficient labeling efficiency of structures varying in molecular density. Such control

usually involves optical and chemical manipulation of photophysics contributing to sample toxicity, as detailed in Section 1.3.

The remarkable spatial resolution of SMLM is achieved at the expense of low temporal resolution and throughput. The large number of frames to reconstruct one final image equals 30 min to hours of acquisition time for sufficient sampling, restricting its application from fast dynamics studies or high-throughput screening.

Super-resolution optical fluctuation imaging (SOFI), as an alternative to SMLM, has great potential to overcome the drawbacks of SMLM as an ideal microscopy method. Without rigorous localization, SOFI enhances spatial resolution by computing high-order correlation analysis of a time series of blinking fluorescent labels. In SOFI, fluorescence signals can appear as fluctuating brightness levels rather than distinctive blinks in SMLM (Fig. 1.1). SOFI is therefore flexible regarding the blinking kinetics of fluorescent labels and relaxes the illumination requirement, eliminating the need for a sparse blinking condition.

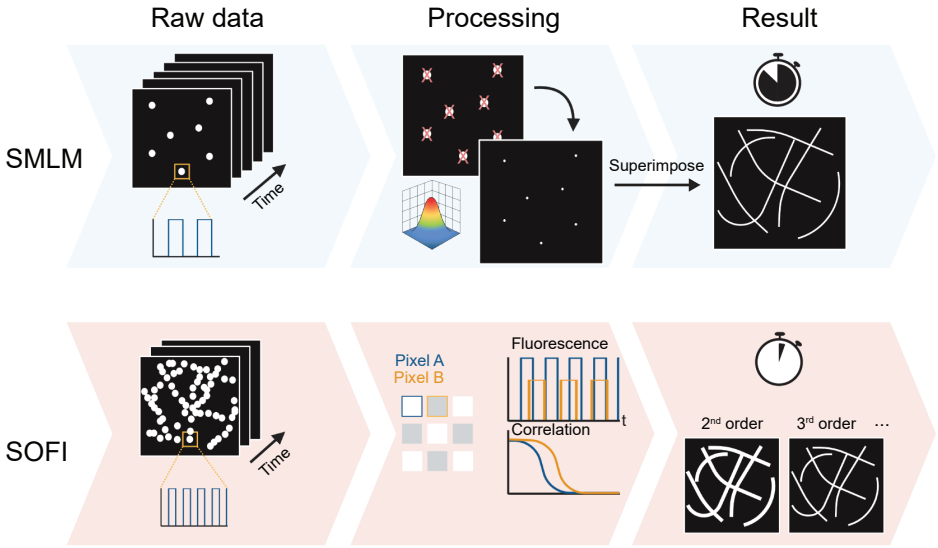


Figure 1.1: **Comparison of principles of two single molecule super-resolution techniques.** Single molecule localization microscopy (SMLM) localizes sparsely distributed individual emitters with high precision. Localizations are superimposed into the final image. Super-resolution fluctuation imaging (SOFI) extracts high-resolution information from the time-variant fluorescence signals by correlation analysis. Both methods require a series of images with blinking fluorophores.

The super-resolving power of SOFI stems from the fact that the fluorescence signal from the same label switching between on- and off-states independently and stochastically is correlative spatially and temporally, while non-correlative signals from different labels or

noise are suppressed by the correlation analysis. The time-variant fluorescence signals I detected on camera from N independent fluorophores positioned at $\mathbf{r}$ is:

$$I(\mathbf{r},t) = \sum_{k=1}^{N} U(\mathbf{r}-\mathbf{r}_k)\cdot\epsilon_k\cdot s_k(t) + b(\mathbf{r},t). \tag{1.2}$$

where $U(\mathbf{r})$ represents the point spread function (PSF) of the imaging system, and $b(\mathbf{r},t)$ describes the background signal. The fluorescence from the molecules is described by $\epsilon_k \cdot s_k(t)$, where ϵ_k denotes the constant brightness and $s_k(t)$ represents a time-dependent fluctuation component. Mathematically, SOFI performs correlation analysis of different orders with calculation of n^{th}-order order cumulant of $I(\mathbf{r},t)$. In general, spatiotemporal cumulants can be calculated using various time lags and combinations of camera pixels. For simplicity, we demonstrate here with a time lag of zero and with cross-cumulants between adjacent pixels, generating interpolated virtual pixels. The n^{th}-order cross-cumulants κ_n thus inherently provide a finer sampling of the super-resolved image:

$$\kappa_n\{I(\mathbf{r},t)\} = \sum_{k=1}^{N} U^n(\mathbf{r}-\mathbf{r}_k)\epsilon_k^n\kappa_n\{s_k(t)\} + \kappa_n\{b(\mathbf{r},t)\}. \tag{1.3}$$

Assuming $b(\mathbf{r},t)$ remains constant and uncorrelated across space and time, Equation 1.3 describes image formation with a PSF raised to the power of n, leading to the narrowing of the Gaussian PSF by a factor of $\sqrt{n}$, thus enhancing the spatial resolution by the same factor. Deconvolution enables a final resolution improvement that scales linearly with the order of the cumulant of n. While there are no theoretical limitations to the resolution enhancement, the order of analysis is restricted by the signal-to-noise ratio and signal-to-background ratio, and ultimately by the statistics hidden within the fluctuation of fluorescence signals.

SOFI also opens a new path for multiplexed imaging. The time-variant component $s_k(t)$ can be described as a binary function taking the value 1 in the on-state and 0 in the off-state based on a two-state emission model. $s_k(t)$ thus follows a Bernoulli distribution with probability ρ, i.e., the on-time ratio or the duty cycle of emitters. The cumulant of $\kappa_n\{s_k(t)\}$ can be approximated by a n^{th}-order polynomial function of ρ as in $f_n(\rho) = \rho(1-\rho)\frac{\partial f_n}{\partial \rho}$. Hence, we can estimate the n^{th}-order cumulant of fluorescence signals in Equation 1.3 with a zero time lag as a function of ρ:

$$\kappa_n\{I(\mathbf{r},t)\} \approx N(\mathbf{r})\cdot f_n(\rho)\sum_{k=1}^{N} U^n(\mathbf{r}-\mathbf{r}_k)\cdot\epsilon_k^n. \tag{1.4}$$

Equation 1.4 shows the dependence of SOFI on blinking kinetics characterized by on-time ratio ρ, brightness ϵ_k, and molecular number N. At $n \geq 3$, these three parameters, unique to different fluorescent labels, can be solved analytically, exploitable for classification of labels or for quantitative information about the labeled molecules.

1.3. Blinking strategy of fluorescent labels

Both SMLM and SOFI are fueled by the stochastic blinking behavior of fluorescent labels (Fig. 1.2(a)). A handful of fluorophores and mechanisms inducing blinking

suitable for single molecule microscopy are available. Photoswitchable, photoactivable or photoconvertible organic dyes are widely used for SMLM implementation such as stochastic optical reconstruction microscopy (STORM) [11]. For example, Alexa Fluor 647 dye and other cyanine-based dye commonly used in dSTORM [13], initially start in the singlet fluorescent on-state (S_1) then are quenched to the triplet state (T_1) by high-intensity red-light excitation (10-20 kW/cm^2) via intersystem crossing pathway. From the triplet state, the molecules can react with reduction agent thiols and enter a long-lived dark state, which can be restored partially to the ground state (S_0) using UV-shifted light, turning a small set of fluorophores *on* for localization (Fig. 1.2(b)). To prevent permanent photobleaching from the triplet state via oxidation-reduction processes, an oxygen-scavenger system is often added to dSTORM buffer. The photoswitching ability and the switching kinetics are highly dependent on the illumination intensity, reduction agent type and concentration, and the presence of oxygen, which differs for each dye and requires individual optimization for achieving the sparse blinking condition of SMLM.

Recently, spontaneously blinking fluorophores (SBFs), which do not require UV lasers or additional chemicals for photoswitching, have seen applications in SMLM and SOFI [14–16]. The SBFs derive from the rhodamine dyes and spontaneously switch between a fluorescent state and a non-fluorescent state, rooted in an intramolecular spirocyclization reaction in thermal equilibrium, with the spirocyclic open form being fluorescent (Fig. 1.2(d)). Modifying the rhodamine scaffold and chemical groups of SBFs shifts the equilibrium, useful for tuning the blinking kinetics of SBFs [17]. Other local micro-environmental factors, including pH, also affect the spirocyclization equilibrium [18].

Photosensitive fluorescent proteins (FPs) can undergo transitions between different fluorescent states upon UV-shifted light excitation, as applied in photoactivated localization microscopy (PALM) [10]. While the mechanism of photoactivable and photoswitchable fluorescent proteins is not as clear as organic dyes, it is generally understood that the switching between on- and off-states involves a cis-trans isomerization of the chromophore in FPs [19]. The structure of the chromophore, protein folding, and maturation can affect the properties of FPs, including blinking kinetics, photostability, and brightness.

Another widely adopted SMLM implementation is through transient binding labels, represented by DNA points accumulation for imaging in nanoscale topography (DNA-PAINT), which utilizes the reversible hybridization of single strand DNA molecules [20]. A short DNA oligo named docking strand attached to the target molecule can temporarily bind to its complementary DNA oligo named imager strand. The imager strands are conjugated with fluorescent dyes and present in abundance in the imaging medium. A fluorescent on-signal is registered upon the binding of the docking and the imager strand, followed by the unbinding, completing a blink (Fig. 1.2(c)). Due to the replenishing fluorophores from the imager strands, DNA-PAINT is more resistant to photobleaching. The blinking kinetics are determined by factors including the DNA sequence, the concentration of imager strands, and other chemicals in the imaging medium.

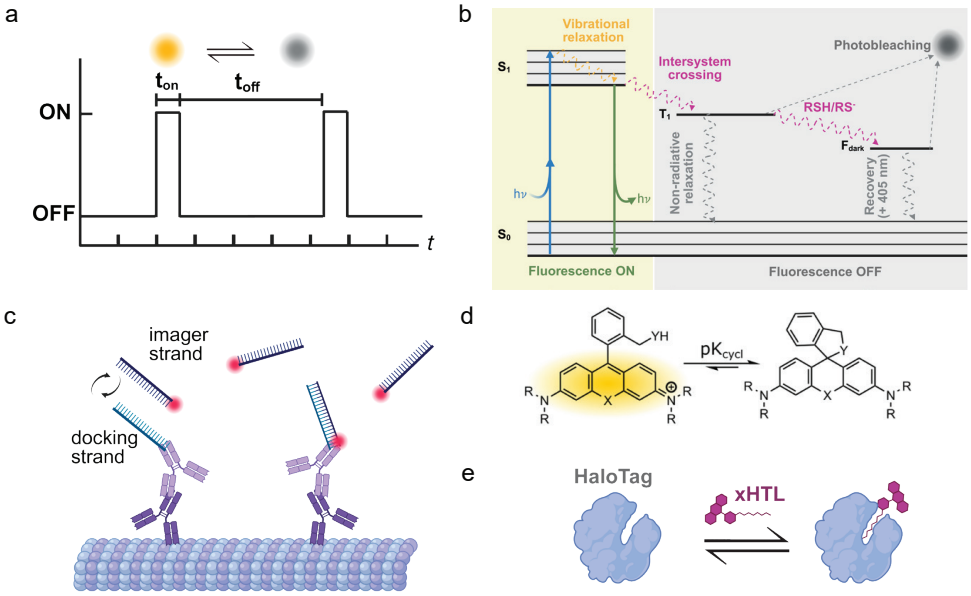


Figure 1.2: **Various strategies of blinking fluorescent labels used in single molecule super-resolution microscopy. (a)** Schematic representation of the fluorescence intensity time trace of a blinking label switching between on- and off-states. The durations of the on- and off-states are defined as the on-time and off-time, respectively. **(b)** Jablonski diagram of photophyical states visited by photoswitching organic dyes. In dSTORM, dyes undergo intersystem crossing to the triplet state T_1 from the excited state S_1, and later enter a reversible dark state F_{dark} through interaction with a reducing agent RSH. **(c)** In DNA-PAINT, blinking signals arise from transient binding between complementary DNA oligos in DNA-PAINT named docking and imager strands. **(d)** Molecular structure of spontaneously blinking dyes cycling through fluorescent on-state and off-state. **(e)** With exchangeable HaloTag ligands (xHTLs), blinking signals arise from the reversible non-covalent binding between HaloTags and xHTLs. Illustration created with BioRender.

1.4. Current challenges of single molecule microscopy

Imaging throughput

Since single molecule microscopy, as a super-resolution imaging technique, gains spatial resolution by acquiring a series of image frames with blinking fluorophores, the low temporal resolution and throughput place a significant barrier to their use in high-content screening and dynamics investigations. Increasing the fluorophores' blinking speed and density reduces the number of frames needed for SMLM; hence, continuous efforts have been made to accelerate the blinking kinetics for all types of labels mentioned in the previous section.

For photoswitchable and photoactivable organic dyes, careful optimization of dye-specific buffer composition and illumination could reach a balance of photostability, brightness-dependent resolution gain, and the acquisition time [21]. Electrochemical modulation by applying external oscillating potential can also increase the switching speed [22]. However, the use of high-intensity excitation and additional chemicals limits their application in live-cell imaging, besides their poor cell permeability. SBFs without such limitations thus hold more potential in fast, live-cell imaging. The well-defined mechanism of rhodamine-based SBFs has recently driven the development of a new array of dyes through rational design shifting the spirocyclization equilibrium. Many SBFs demonstrate kinetics suitable for the fast and gentle approach of SOFI [15], however they are mostly selected and evaluated for SMLM imaging and their performance for SOFI is yet unknown [23].

DNA-PAINT decouples the blinking from excitation, whose blinking kinetics are in principle programmable. One approach to accelerating blinking kinetics for DNA-PAINT is carefully choosing DNA sequence with high hybridization rate from low-throughput *in vitro* screening [24], or using mismatches to increase the dehybridization rate [25]. Since the sequence itself does not inform well about the hybridization kinetics of DNA, optimizing sequence alone from numerous possibilities is not yet feasible. Ago-PAINT is independent of the DNA sequence and has shown a 10-fold acceleration by forming favorable structures for hybridization of imager strands mediated by proteins [26]. Another approach is to increase the binding event frequency by using repetitive motifs in docking strand which has expanded into a handful orthogonal repeating sequences for sequential DNA-PAINT imaging [27]. The drawback is that lengthy docking strands impede localization precision, as recently investigated [28]. Increase of the imager strand concentration also contributes to increasing binding frequency, however necessitates the usage of fluorogenic or self-quenching imager strands in order to alleviate the overwhelming background signal from the high concentration imager strands [29–31]. Similar background suppression methods include using FRET donor-acceptor pairs such that the imager fluorescence is not detected [32, 33], or using a UV-light-activatable imager [34]. Other factors such as buffer salinity and DNA duplex destabilizers can also be used for DNA hybridization modulation [24].

However, there exists an upper limit of blinking kinetics acceleration for SMLM. High emitter density risks localization artifacts from overlapping PSFs [35]. Low on-time and fewer photons harvested hinder the localization precision and consequently resolution. Machine learning algorithms could tolerate 10-100 times higher density [36, 37], albeit an expensive training process is needed for each optical and sample condition. SOFI, though

less prevalent than SMLM, is compatible with a much larger range of blinking behaviors and illumination modalities, providing an opportunity for single molecule microscopy to be explored.

Multiplexing capacity

Multiplexed super-resolution imaging enables precise mapping of complex cellular organization and interaction. Simple multi-color imaging using dyes with large spectral distance apart can introduce chromatic aberration up to 50 nm, nullifying the advantage of high resolution of SMLM in co-localization studies [38]. The spatiotemporal separation of fluorescence signals of single molecule microscopy makes it complicated for the classification and registration of each color channel. Sequential imaging for DNA-PAINT, known as Exchange-PAINT, applies buffers containing different imager strands one at a time for imaging corresponding targets with matching docking strands [25, 39, 40]. This allows for use with a single laser and single-color detection and does not require additional modification in the optics. Combining with removable secondary adapters between the target molecule and the docking strand, sequential DNA-PAINT has been demonstrated for 30-plex imaging, with the significant shortcoming of long acquisition times [41, 42].

Another pathway for multiplexed SMLM is through spectral separation. Spectral demixing utilizes dyes with overlapping emission spectra which are simultaneously excited at the same wavelength and detected in two optical channels [43, 44]. The ratio of fluorescence intensity of the two channels can be used to register the localizations. Splitting the fluorescence lowers the photon budget used for localization, and the number of distinguishable colors is constrained by available dyes and dichroic mirrors. Optimizing blinking kinetics for different photoswitchable dyes within the same sample is also challenging. Other characteristics of dyes can be exploited for classification, usually demanding in optical configuration and data analysis. For example, spectroscopic SMLM detects spectral differences of dyes by applying dispersive optical elements in the detection [45]. fm-DNA-PAINT and fm-STORM distinguish emission responses of different dyes by using frequency-modulated excitation lasers [46]. PSF engineering encodes colors in the subtle geometrical distinctions of optically-modified PSFs of the microscope [47, 48]. Fluorescence lifetime is also a multiplexable dimension accessible only with specialized detectors [49, 50].

Blinking kinetics intrinsic to the fluorescent labels are a wealth of information without additional probing beyond the camera detection for single molecule imaging. Kinetics multiplexing has been shown in *in vitro* DNA origami imaging [51]. High-order SOFI is sensitive to brightness and blinking kinetics, as shown in Section 1.2, offering a promising avenue for multiplexing.

Live-cell compatibility

Most SRM techniques see limitations in live-cell imaging due to high laser exposure, either from increased laser intensity or acquisition time. It is perhaps most challenging for single molecule microscopy where the blinking fluorophores call for conditions harmful for live cells. Besides the lengthy acquisition that increases the phototoxicity,

challenges also include the use of UV light and thiol buffer in the case of photoswitchable organic dyes, if they are permeable to cells in the first place. Fluorescent proteins can be expressed together with target protein in live cells; however, their lack of brightness and photostability and limited options for multiplexing hamper high-quality super-resolution images. SBFs, with the advantages of organic dyes but free from high-power lasers and chemical usage, are seen as a direct answer to live-cell SMLM. They have also been demonstrated for high resolution SOFI, while emerging new SBFs blinking too fast for SMLM hold great promises.

HaloTag-PAINT, an analog of DNA-PAINT, uses the non-covalent reversible binding of self-labeling enzymatic protein tags and fluorescent ligands, known as the exchangeable HaloTag ligands or xHTLs (Fig. 1.2(e)) [52]. Not only is HaloTag-PAINT suitable for live-cell labeling, but the strategies for speeding up DNA-PAINT could be deployed similarly. HaloTags are also great platforms for introducing SBFs into live cells.

Instrumentation

Though less complex in optical configuration than other SRM methods, single molecule microscopy has special requirements for instrumentation. Firstly, photoswitching needs to be enabled by high-lower multi-line lasers. The weak fluorescence of single molecules requires detection on sensitive and low-noise cameras, with sCMOS cameras now the standard. In addition, the lengthy acquisition times subject it to sample drift and demand active focus stabilization. The high spatial resolution requires high optical and mechanical stability in general. Such features found in commercial SMLM systems are pricey and high maintenance, constraining the broader access to single molecule microscopy.

1.5. Outline

This dissertation aims to present methodologies addressing the challenges of current super-resolution fluorescence microscopy towards the ideal functionalities for high-throughput and live-cell imaging, by optimizing single molecule imaging processing and applying novel fluorescent labels.

To achieve the goal, a microscope for said single molecule imaging has to be established. The comparably simpler hardware requirement of SMLM and SOFI, does not dismiss the demand in laser excitation and complexity in software. Chapter 2 details the design and construction of a state-of-the-art TIRF microscope named Open Blink, along with its control software implementation. Open Blink joins a young yet fast-growing community of open-source microscopy in the ambition to provide access of super-resolution imaging techniques.

To increase the throughput of super-resolution microscopy in fixed cells, we present a method combining DNA-PAINT and SOFI in Chapter 3. The characteristic programmable blinking kinetics in DNA-PAINT finds synergy with SOFI's capability to analyze blinking to fluctuating fluorescence signals. Leveraging the easy modification of blinking kinetics during DNA-PAINT imaging, we also present a workflow that enables real-time adjustment of temporal and spatial resolution.

In the same vein as Chapter 3, Chapter 4 aims to further increase the blinking kinetics in DNA-PAINT by identifying sequences with high association rates. We demonstrate how a novel rapid sequence kinetics screening technique is used for such selection. We propose a new speed-optimized DNA-PAINT sequence and open up more sequence possibilities for both SMLM and SOFI.

We expand the high-throughput single molecule super-resolution venues towards live-cell applications in Chapter 5. We benchmark two labeling systems based on enzymatic protein tags: spontaneously blinking fluorophores and transiently binding exchangeable ligands on HaloTags, and evaluate their compatibility with live-cell SOFI. We take initial steps toward multiplexed imaging with SOFI.

Lastly, in Chapter 6, I address the limitations of single molecule super-resolution microscopy using SMLM, SOFI, and the labeling systems proposed, and outline further considerations to achieve the goal of high-throughput, multiplexed live-cell super-resolution imaging. Additionally, I also discuss how open microscopy could enable this objective.

References

[1] A. V. Leeuwenhoek, Mr. Leewenhoecks letter written to the publisher from Delft the 14th of May 1677, concerning the observations by him made of the carneous fibres of a muscle, among others. Philosophical Transactions 12, 899–905 (1677). DOI: 10.1098/rstl.1677.0027.

[2] A. v. Leeuwenhoek, III. Part of a letter from Mr. Lewenhoek, concerning the circulation and globules of the blood in butts, Philosophical Transactions 22, 552–560 (1700). DOI: 10.1098/rstl.1700.0027.

[3] M. Renz, Fluorescence microscopy—A historical and technical perspective, Cytometry Part A 83, 767–779 (2013). DOI: 10.1002/cyto.a.22295.

[4] R. Yuste, Fluorescence microscopy today, Nature Methods 2, 902–904 (2005). DOI: 10.1038/nmeth1205-902.

[5] E. Abbe, Beiträge zur Theorie des Mikroskops und der mikroskopischen Wahrnehmung, Archiv für Mikroskopische Anatomie 9, 413–468 (1873). DOI: 10.1007/BF02956173.

[6] S. W. Hell, J. Wichmann, Breaking the diffraction resolution limit by stimulated emission: stimulated-emission-depletion fluorescence microscopy, Optics Letters, Vol. 19, Issue 11, pp. 780-782 (1994). DOI: 10.1364/OL.19.000780.

[7] F. Balzarotti, Y. Eilers, K. C. Gwosch, A. H. Gynnå, V. Westphal, F. D. Stefani, J. Elf, S. W. Hell, Nanometer resolution imaging and tracking of fluorescent molecules with minimal photon fluxes, Science 355, 606–612 (2017). DOI: 10.1126/science.aak9913.

[8] M. G. Gustafsson, Surpassing the lateral resolution limit by a factor of two using structured illumination microscopy, Journal of Microscopy 198, 82–87 (2000). DOI: 10.1046/J.1365-2818.2000.00710.X.

[9] E. Betzig, Proposed method for molecular optical imaging, Optics Letters 20, 237–239 (1995). DOI: 10.1364/OL.20.000237.

[10] E. Betzig, G. H. Patterson, R. Sougrat, O. W. Lindwasser, S. Olenych, J. S. Bonifacino, M. W. Davidson, J. Lippincott-Schwartz, H. F. Hess, Imaging Intracellular Fluorescent Proteins at Nanometer Resolution, Science 313, 1642–1645 (2006). DOI: 10.1126/science.1127344.

[11] M. J. Rust, M. Bates, X. Zhuang, Sub-diffraction-limit imaging by stochastic optical reconstruction microscopy (STORM), Nature Methods 3, 793–795 (2006). DOI: 10.1038/nmeth929.

[12] T. Dertinger, R. Colyer, G. Iyer, S. Weiss, J. Enderlein, Fast, background-free, 3D super-resolution optical fluctuation imaging (SOFI), Proceedings of the National Academy of Sciences 106, 22287–22292 (2009). DOI: 10.1073/pnas.0907866106.

[13] S. van de Linde, A. Löschberger, T. Klein, M. Heidbreder, S. Wolter, M. Heilemann, M. Sauer, Direct stochastic optical reconstruction microscopy with standard fluorescent probes, Nature Protocols 6, 991–1009 (2011). DOI: 10.1038/nprot.2011.336.

[14] S.-n. Uno, M. Kamiya, T. Yoshihara, K. Sugawara, K. Okabe, M. C. Tarhan, H. Fujita, T. Funatsu, Y. Okada, S. Tobita, Y. Urano, A spontaneously blinking fluorophore based on intramolecular spirocyclization for live-cell super-resolution imaging, Nature Chemistry 6, 681–689 (2014). DOI: 10.1038/nchem.2002.

[15] K. L. Holland, S. E. Plutkis, B. P. English, T. A. Daugird, A. Sau, J. B. Grimm, Q. Zheng, A. Sharma, S. Dave, A. Schmidt, F. Rahman, L. Xie, P. Dong, A. N. Tkachuk, T. A. Brown, R. H. Singer, Z. J. Liu, S. M. Musser, W. R. Legant, C. G. Galbraith, L. D. Lavis, A series of spontaneously blinking dyes for super-resolution microscopy, Nature Methods 23, 909–913 (2026). DOI: 10.1038/s41592-026-03062-5.

[16] K. Grussmayer, T. Lukes, T. Lasser, A. Radenovic, Self-Blinking Dyes Unlock High-Order and Multiplane Super-Resolution Optical Fluctuation Imaging, ACS Nano 14, 9156–9165 (2020). DOI: 10.1021/acsnano.0c04602.

[17] N. Lardon, L. Wang, A. Tschanz, P. Hoess, M. Tran, E. D'Este, J. Ries, K. Johnsson, Systematic Tuning of Rhodamine Spirocyclization for Super-resolution Microscopy, Journal of the American Chemical Society 143, 14592–14600 (2021). DOI: 10.1021/jacs.1c05004.

[18] R. Tachibana, M. Kamiya, A. Morozumi, Y. Miyazaki, H. Fujioka, A. Nanjo, R. Kojima, T. Komatsu, T. Ueno, K. Hanaoka, T. Yoshihara, S. Tobita, Y. Urano, Design of spontaneously blinking fluorophores for live-cell super-resolution imaging based on quantum-chemical calculations, Chemical Communications 56, 13173–13176 (2020). DOI: 10.1039/d0cc05126h.

[19] F. M. Jradi, L. D. Lavis, Chemistry of Photosensitive Fluorophores for Single-Molecule Localization Microscopy, ACS Chemical Biology 14, 1077–1090 (2019). DOI: 10.1021/acschembio.9b00197.

[20] J. Schnitzbauer, M. T. Strauss, T. Schlichthaerle, F. Schueder, R. Jungmann, Super-resolution microscopy with DNA-PAINT, Nature Protocols 12, 1198–1228 (2017). DOI: 10.1038/nprot.2017.024.

[21] R. Diekmann, M. Kahnwald, A. Schoenit, J. Deschamps, U. Matti, J. Ries, Optimizing imaging speed and excitation intensity for single-molecule localization microscopy, Nature Methods 17, 909–912 (2020). DOI: 10.1038/s41592-020-0918-5.

[22] Y. Yang, Y. Ma, J. F. Berengut, L. K. Lee, R. D. Tilley, K. Gaus, J. J. Gooding, Electrochemically controlled blinking of fluorophores for quantitative STORM imaging, Nature Photonics 18, 713–720 (2024). DOI: 10.1038/s41566-024-01431-0.

[23] Y. Zheng, Z. Ye, X. Zhang, Y. Xiao, Recruiting Rate Determines the Blinking Propensity of Rhodamine Fluorophores for Super-Resolution Imaging, Journal of the American Chemical Society 145, 5125–5133 (2023). DOI: 10.1021/jacs.2c11395.

[24] F. Schueder, J. Stein, F. Stehr, A. Auer, B. Sperl, M. T. Strauss, P. Schwille, R. Jungmann, An order of magnitude faster DNA-PAINT imaging by optimized sequence design and buffer conditions, Nature Methods 2019 16:11 16, 1101–1104 (2019). DOI: 10.1038/s41592-019-0584-7.

[25] R. Jungmann, M. S. Avendaño, J. B. Woehrstein, M. Dai, W. M. Shih, P. Yin, Multiplexed 3D cellular super-resolution imaging with DNA-PAINT and Exchange-PAINT, Nature Methods 2014 11:3 11, 313–318 (2014). DOI: 10.1038/nmeth.2835.

[26] M. Filius, T. J. Cui, A. N. Ananth, M. W. Docter, J. W. Hegge, J. van der Oost, C. Joo, High-Speed Super-Resolution Imaging Using Protein-Assisted DNA-PAINT, Nano Lett. 20, 2264–2270 (2020). DOI: 10.1021/acs.nanolett.9b04277.

[27] S. Strauss, R. Jungmann, Up to 100-fold speedup and multiplexing in optimized DNA-PAINT, Nature methods 17, 789–791 (2020). DOI: 10.1038/s41592-020-0869-x.

[28] D. A. Helmerich, M. Budiarta, P. Eiring, M. Sauer, S. Doose, G. Beliu, Impact of Docking Strand Design on Spatial Resolution in DNA-Points Accumulation for Imaging in Nanoscale Topography, ChemPhysChem 27, e202500803 (2026). DOI: 10.1002/cphc.202500803.

[29] K. K. H. Chung, Z. Zhang, P. Kidd, Y. Zhang, N. D. Williams, B. Rollins, Y. Yang, C. Lin, D. Baddeley, J. Bewersdorf, Fluorogenic DNA-PAINT for faster, low-background super-resolution imaging, Nature Methods 19, 554–559 (2022). DOI: 10.1038/s41592-022-01464-9.

[30] L. F. Kessler, A. Balakrishnan, N. S. Deußner-Helfmann, Y. Li, M. Mantel, M. Glogger, H.-D. Barth, M. S. Dietz, M. Heilemann, Self-quenched Fluorophore Dimers for DNA-PAINT and STED Microscopy, Angewandte Chemie International Edition 62, e202307538 (2023). DOI: 10.1002/anie.202307538.

[31] A. Ghosh, M. Meub, D. A. Helmerich, S. Doose, M. Sauer, Fast, whole-cell DNA-PAINT imaging with dual-labeled self-quenched imager probes, bioRxiv (2023). DOI: 10.1101/2023.10.09.561472.

[32] J. Lee, S. Park, S. Hohng, Accelerated FRET-PAINT microscopy, Molecular Brain 11, 70 (2018). DOI: 10.1186/s13041-018-0414-3.

[33] A. Auer, M. T. Strauss, T. Schlichthaerle, R. Jungmann, Fast, Background-Free DNA-PAINT Imaging Using FRET-Based Probes, Nano Letters 17, 6428–6434 (2017). DOI: 10.1021/acs.nanolett.7b03425.

[34] S. Jang, M. Kim, S.-H. Shim, Reductively Caged, Photoactivatable DNA-PAINT for High-Throughput Super-resolution Microscopy, Angewandte Chemie 59, 11758–11762 (2020). DOI: 10.1002/anie.201915377.

[35] I. Costello, S. Cox, Analysing errors in single-molecule localisation microscopy, The International Journal of Biochemistry & Cell Biology 134, 105931 (2021). DOI: 10.1016/j.biocel.2021.105931.

[36] E. Nehme, L. E. Weiss, T. Michaeli, Y. Shechtman, Deep-STORM: super-resolution single-molecule microscopy by deep learning, Optica 5, 458–464 (2018). DOI: 10.1364/OPTICA.5.000458.

[37] P. Zhang, D. Ma, X. Cheng, A. P. Tsai, Y. Tang, H.-C. Gao, L. Fang, C. Bi, G. E. Landreth, A. A. Chubykin, F. Huang, Deep learning-driven adaptive optics for single-molecule localization microscopy, Nature Methods, 1–11 (2023). DOI: 10.1038/s41592-023-02029-0.

[38] M. Erdelyi, E. Rees, D. Metcalf, G. S. K. Schierle, L. Dudas, J. Sinko, A. E. Knight, C. F. Kaminski, Correcting chromatic offset in multicolor super-resolution localization microscopy, Optics Express 21, 10978–10988 (2013). DOI: 10.1364/OE.21.010978.

[39] F. Schueder, M. T. Strauss, D. Hoerl, J. Schnitzbauer, T. Schlichthaerle, S. Strauss, P. Yin, H. Harz, H. Leonhardt, R. Jungmann, Universal Super-Resolution Multiplexing by DNA Exchange, Angewandte Chemie International Edition 56, 4052–4055 (2017). DOI: https://doi.org/10.1002/anie.201611729.

[40] S. S. Agasti, Y. Wang, F. Schueder, A. Sukumar, R. Jungmann, P. Yin, DNA-barcoded labeling probes for highly multiplexed Exchange-PAINT imaging, Chemical Science 8, 3080–3091 (2017). DOI: 10.1039/C6SC05420J.

[41] F. Schueder, F. Rivera-Molina, M. Su, Z. Marin, P. Kidd, J. E. Rothman, D. Toomre, J. Bewersdorf, Unraveling cellular complexity with transient adapters in highly multiplexed super-resolution imaging, Cell 187, 1769–1784.e18 (2024). DOI: 10.1016/j.cell.2024.02.033.

[42] M. D. Lycas, S. Manley, DNA-PAINT adaptors make for efficient multiplexing, Cell Reports Methods 4, 100801 (2024). DOI: 10.1016/j.crmeth.2024.100801.

[43] A. Schönle, S. W. Hell, Fluorescence nanoscopy goes multicolor, Nature Biotechnology 25, 1234–1235 (2007). DOI: 10.1038/nbt1107-1234.

[44] M. Bossi, J. Fölling, V. N. Belov, V. P. Boyarskiy, R. Medda, A. Egner, C. Eggeling, A. Schönle, S. W. Hell, Multicolor far-field fluorescence nanoscopy through isolated detection of distinct molecular species, Nano Letters 8, 2463–2468 (2008). DOI: 10.1021/nl801471d.

[45] C. Butler, G. E. Saraceno, A. Kechkar, N. Bénac, V. Studer, J. P. Dupuis, L. Groc, R. Galland, J.-B. Sibarita, Multi-Dimensional Spectral Single Molecule Localization Microscopy, Frontiers in Bioinformatics 2, 813494 (2022). DOI: 10.3389/fbinf.2022.813494.

[46] P. A. Gómez-García, E. T. Garbacik, J. J. Otterstrom, M. F. Garcia-Parajo, M. Lakadamyali, Excitation-multiplexed multicolor superresolution imaging with fm-STORM and fm-DNA-PAINT, Proceedings of the National Academy of Sciences 115, 12991–12996 (2018). DOI: 10.1073/pnas.1804725115.

[47] J. Broeken, B. Rieger, S. Stallinga, Simultaneous measurement of position and color of single fluorescent emitters using diffractive optics, Optics Letters 39, 3352–3355 (2014). DOI: 10.1364/OL.39.003352.

[48] M. Li, W. Shi, S. Liu, S. Fu, Y. Fei, L. Zhou, K. Fang, Y. Li, Fast and universal single-molecule localization using multi-dimensional point spread functions, Optics Express 32, 42601–42615 (2024). DOI: 10.1364/OE.531588.

[49] J. C. Thiele, D. A. Helmerich, N. Oleksiievets, R. Tsukanov, E. Butkevich, M. Sauer, O. Nevskyi, J. Enderlein, Confocal Fluorescence-Lifetime Single-Molecule Localization Microscopy, ACS Nano 14, 14190–14200 (2020). DOI: 10.1021/acsnano.0c07322.

[50] N. Oleksiievets, Y. Sargsyan, J. C. Thiele, N. Mougios, S. Sograte-Idrissi, O. Nevskyi, I. Gregor, F. Opazo, S. Thoms, J. Enderlein, R. Tsukanov, Fluorescence lifetime DNA-PAINT for multiplexed super-resolution imaging of cells, Communications Biology 5, 38 (2022). DOI: 10.1038/s42003-021-02976-4.

[51] O. K. Wade *et al.*, 124-Color Super-resolution Imaging by Engineering DNA-PAINT Blinking Kinetics, Nano Letters 19, 2641–2646 (2019). DOI: 10.1021/acs.nanolett.9b00660.

[52] J. Kompa, J. Bruins, M. Glogger, J. Wilhelm, M. S. Frei, M. Tarnawski, E. D'Este, M. Heilemann, J. Hiblot, K. Johnsson, Exchangeable HaloTag Ligands for Super-Resolution Fluorescence Microscopy, J. Am. Chem. Soc. 145, 3075–3083 (2023). DOI: 10.1021/jacs.2c11969.

2

Open Blink: Low-cost TIRF Microscopy for Super-resolution Imaging

Single molecule based super-resolution imaging demands highly in illumination quality and optical stability compared to conventional wide-field imaging. Open microscopy platforms provide flexibility, accessibility and expandability, unmatched by commercial instruments. This chapter describes a home-made TIRF microscope with state-of-the-art features for single molecule microscopy, novel open-source software compatibility and unprecedented low cost, which is used for microscopic imaging in the following chapters.

A modified version of this chapter has been published: R. Huo, J. Komen, M. Engelhardt, A. Millot, J. Extermann, and K. Grußmayer, bioRxiv 10.64898/2026.03.10.710894 (2026). J. Komen and A. Millot were junior researchers supervised by the author.

2.1. Introduction

Super-resolution microscopy techniques revealing information at nanometer scale have contributed to many new discoveries in life science [1, 2]. Among them, single-molecule localization microscopy (SMLM) and super-resolution optical fluctuation imaging (SOFI), based on the stochastic blinking of fluorophores, gained wide popularity because of their high resolution and compatibility with wide-field microscopes [3–6]. Quantitative SMLM requires nanometric stability, homogeneous and high power illumination over a large field of view and precise multi-channel registration, achievable only in high-end instruments. In particular, maintaining uniform blinking kinetics and localization precision over large fields of view remains technically demanding. However, costly equipment and maintenance, in addition to the difficulty of modifying commercial microscopes, hinder the accessibility of SMLM for researchers.

With the continuous advancements of super-resolution microscopy by expert laboratories in recent years, its wider adoption called for affordable and easy-to-use hardware and corresponding control software for SMLM. In response, several open-source microscopes have been developed [7], which either focus on sub-modules such as the excitation source [8, 9], microscope body [10–12], camera [13], focus-lock module [14], and control software [15], or provide a full-system solution as in K2 TIRF [16], miEye [17], NanoPro [18] and a 3D SMLM setup [19]. Those open microscopy projects have demonstrated the benefits of home-made microscopes enabling different types of single molecule imaging, yet typically do not offer fully-integrated open control software, and provide limited laser power or field of view. Nevertheless, the trade-offs between desirable functionalities and cost, as well as between the technical complexity and user friendliness remain a challenge for scientists considering home-made microscopy setups. For example, customized setups are frequently built for specific use cases, with the design dictated by already available components for convenience, and therefore not straightforward to be transferred to another application or another laboratory. Likewise, home-made control electronics and research software are often not designed or optimized for reusability, demanding expertise in both electronics and programming when implementing them.

To address these challenges, we designed Open Blink guided by the objective of achieving high-performance SMLM while ensuring accessibility, ease of use and low maintenance. We made design choices favoring long-term mechanical and optical stability and selected components commonly available and widely acknowledged by the community. Engineering expertise needed in building such as machining and soldering is minimized and easily outsourced. We prioritized software accessibility and scalability and aimed for hardware control and image acquisition schemes that are user-friendly and capable of metadata recording for downstream imaging analysis and data reproducibility. Despite the low cost, Open Blink is equipped with state-of-the-art features for SMLM, including homogeneous illumination, total internal reflection (TIR), and focus stabilization.

Compared to existing solutions, Open Blink demonstrates substantial improvements in several aspects. Firstly, without compromising the illumination qualities and homogeneity, the multimode high-power semiconductor lasers greatly reduce the price of laser sources and offer a high-power open-hardware laser combiner alternative, as

demonstrated in Section 2.2.1. Secondly, the home-made microscope body adapted from the open microscope frame miCube is economical, mechanically stable, and easy to modify[11]. We further reduced the miCube frame size to enable an enlarged field of view (FOV) sized over 200 × 200 μm^2, as shown in Section 2.2.2, while preserving illumination homogeneity and thus localization precision. Together with the focus-lock module '*fg*Focus', which we developed based on *pg*Focus and *qg*Focus[16, 20] to address the absence of an up-to-date and μManager-compatible implementation, this makes Open Blink particularly suitable for long-term high-throughput single molecule based super-resolution microscopy, powerful for biological discovery.

Most open hardware projects develop their customized control software with Python, LabVIEW, or C# [9, 16–18]. Instead of specialized programming and varying graphic interfaces, we opted for the open-source microscopy control software μManager for Open Blink, which is well-known to the bioimaging community for its integrated functions for common microscope hardware control and imaging acquisition tasks. A large number of device adapters from hardware vendors and developers, and customizable development capability enabled by pycroManager, pymmcore-plus and EMU [21–23] make μManager flexible for extension with minimal specialized programming, which we demonstrate in Section 2.3 with our laser combiner controller and focus-lock controller μManager plugins. Communication between hardware and software for Open Blink is established through simple micro-controllers without complex electronics. Metadata containing imaging parameters such as stage positions, laser power, and exposure time are also incorporated for each image acquired, ensuring appropriate documentation for reliable image analysis and reproducible experiments.

Finally, we showcase applications of Open Blink in single molecule super-resolution cell imaging with DNA-PAINT, dSTORM and SOFI respectively in Section 2.4.

In total, Open Blink cuts the cost of a full super-resolution microscope system significantly to approximately 70 000 Euros. Documentation of Open Blink, including the list of components, design files, and compiled ready-to-use μManager plugins, is available at Grußmayer Lab GitHub page. CAD files and example data is downloadable at `https://doi.org/10.4121/bc373b4b-29f1-4108-b166-85420628ff97`. With semi-turnkey components, simple control electronics, and full μManager integration, Open Blink provides a reproducible and scalable platform for high-performance quantitative single-molecule super-resolution microscopy at substantially reduced cost.

2.2. Hardware design and performance

2.2.1. Quad-line homogeneous high-power laser combiner

Single-molecule localization microscopy (SMLM) reconstructs a super-resolved image by precisely localizing the position of individual molecules in tens to hundreds of thousands of images [24–26]. Implementations such as direct stochastic optical reconstruction microscopy (dSTORM) demand high power laser excitation up to 10 kW/cm^2 for photoswitching of organic dyes to achieve sparse single-molecule conditions [27, 28]. High-power excitation sources from single mode lasers contribute to the high cost of SMLM setups. Inspired by Ries lab's laser engine [8], which employed high power-to-cost ratio laser diodes with customized drivers, we built a quad-line laser combiner with

semi-turnkey diode lasers. In a similar layout as Ries lab laser engine, two diode lasers at 638 nm are combined via a polarizing beam splitter to double the excitation power at the far-red wavelength, in parallel to the 405 nm and 488 nm diode lasers (LAB-405-500/LAB-488-2000/LAB-638-1000, Lasertack GmBH), as shown in Fig. 2.1 (a). A diode-pumped solid-state (DPSS) laser at 561 nm (MGL-FN-561, CNI Laser) completes the visible spectrum coverage. All combined laser beams are launched into a multimode optical fiber (MMF) with an aspherical lens.

The use of the semi-turnkey diode lasers is much more cost-effective compared to single mode lasers of similar power (summarized in Fig. 2.1 (b)), amounting to ~29% of the total cost of Open Blink. When compared to using unmounted and uncollimated laser diodes, it also saves one from soldering work and laser driver current calibration. Although the diode lasers selected are supplied with calibrated drivers, they lack modulation units or control software. We developed the control electronics and μManager plugin for the Open Blink laser combiner based on micro-controllers which is detailed in Section 2.3.

SMLM image quality is substantially affected by the homogeneity of excitation across the field of view, as the localization precision is proportional to the number of detected photons, which in turn depends on the excitation laser intensity [29]. The laser excitation also influences the photoswitching or photoactivation behavior of fluorophores, and inhomogeneities in the illumination can lead to variations in molecular densities. A homogeneous illumination thus ensures a consistent resolution over the field of view, crucial for interpreting SMLM rendered images [28]. A typical MMF has an inhomogeneous output intensity profile patterned with speckles due to the interference of all propagating modes. It has been reported that a mode scrambler effectively reduces such speckles, thus achieving homogeneous illumination at the MMF output [8–10]. In a similar design reported by Lam et al. [9], we used a customized MMF (NA 0.22, CeramOptec), whose square core profile of size 70 μm by 70 μm enables TIRF illumination (detailed in Section 2.2.2) and maximizes the effective detection area on the camera chip. The homogeneity of laser illumination is facilitated by a brushed vibrational motor (VM, 5mm - 11mm Type, 304-111, precision microdrives) agitating the MMF connected through a 3D-printed mount (polylactic acid, CAD available), as shown in the zoom-in schematics in Fig. 2.1 (a).

Compared to single mode optical fibers, MMFs have higher numerical apertures (NA), which eases the coupling of input lasers. We measured the MMF coupling efficiency and the maximum output power of the laser combiner at the exit of the MMF. The coupling efficiency for different wavelengths varies between 77% to 94% (Fig. 2.1 (c)), calculated by the ratio of laser intensity exiting and entering the MMF. These values demonstrate that high-power multimode excitation can be achieved with efficiencies comparable to single mode fiber delivery while enabling substantially reduced system cost. Notably, at 638 nm the laser combiner yields a maximum power of 1.3 W, equivalent of intensity of 8.58 kW/cm^2 at the sample plane, sufficient for high-quality SMLM (example image shown in Section 2.4). The homogeneity of the intensity is first verified by imaging the MMF output intensity profile (Fig. 2.1 (d)) using a CMOS camera (U3-3060CP-M-GL Rev 2.2, iDS GmbH). At 5 ms exposure time, the diode lasers at 408 nm, 488 nm, and 638 nm exhibit significantly decreased speckles, quantitatively assessed by the image

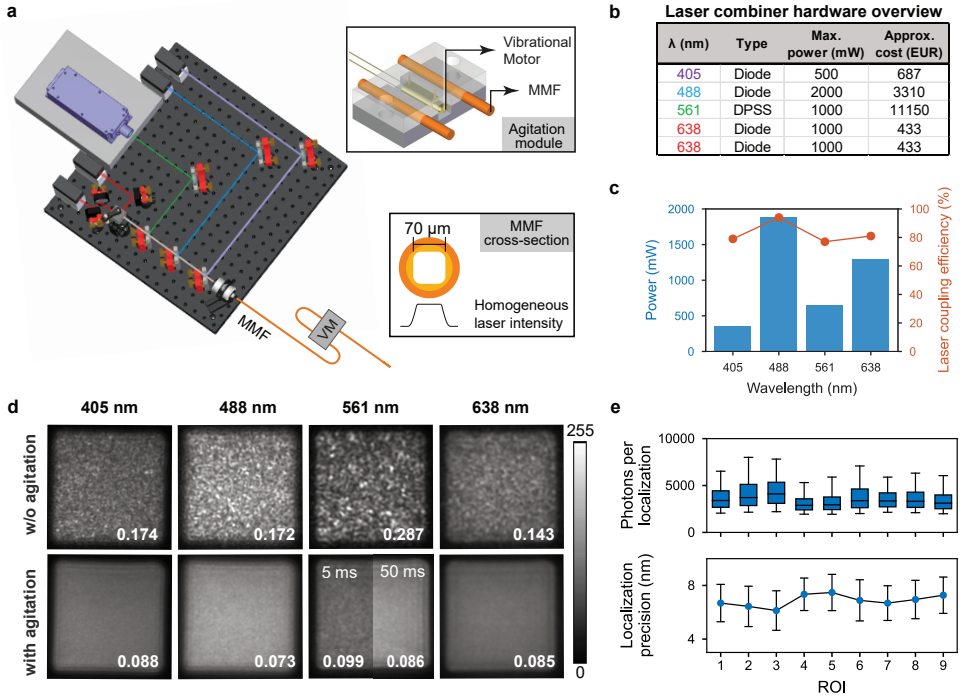


Figure 2.1: **A low-cost high-power laser combiner with multimode fiber (MMF) pigtail delivers homogeneous illumination. (a)** 3D representation of the quad-line laser combiner of Open Blink. Agitation from the vibrational motor (VM) is transmitted to the MMF in a customized mount displayed in the zoom-in image. MMF and VM drawings are not to scale. **(b)** List of the lasers used, their maximum power, and approximate prices. DPSS: Diode-pumped solid-state laser. **(c)** Power performance of the laser combiner at four wavelengths, shown as laser coupling efficiency (orange line) and maximum output power (blue bar) at the exit of the MMF. **(d)** Comparison of laser intensity profile at the MMF output in the presence and absence of agitation from the VM. Images taken directly at the MMF exit with 5 ms exposure time, except for an additional image for 561 nm which has exposure time of 50 ms. Number denotes the contrast of speckles of each image. Each image is sized 2.6 μm by 2.6 μm and color bar corresponds to pixel gray value from 0 to 255. **(e)** Evaluation of sample plane illumination homogeneity by DNA-PAINT imaging at 9 different regions of interest (ROIs) indicated in Fig. 2.2 (c). Top: box plot of average photon count per localization; bottom: average localization precision with error bars indicating the standard deviation. 242,488 localizations analyzed.

contrast which calculates the ratio between the standard deviation and average image intensity. The more coherent single mode DPSS laser at 561 nm results in more speckles and higher contrast value at this fast image acquisition rate, which can be effectively reduced at increased exposure times of 50 ms, well within the typical range of exposure times used for single molecule imaging. Note that, among other MMFs we have tested, the performance of homogeneity from mode scrambling by vibrational motor varies. A small core MMF (M42L05, Thorlabs) compatible with TIRF as used in Kwakwa et al. [10] does not respond to the agitation, while a larger square core MMF (M103L05, Thorlabs) as used in Schroder et al. [8] shows improved homogeneity when agitated. Images of their respective output intensity profile are found in Supplementary Fig. 2.7 in Section 2.8. We suspect that the variations in the coatings applied around the cladding of the MMFs affect the effectiveness of mode scrambling. The more rigid polymer coating in the Thorlabs M103L05 might subject the MMF to increased microbends compared to the acrylate coatings used in the M42L05, thus inducing effective spatial mixing of the propagation modes [30]. Specialized mode scramblers with higher vibrational frequency and amplitude could expand the choices of MMFs.

Next, we examined the effect of homogeneous illumination for super-resolution imaging quality by DNA-PAINT imaging (details in Section 2.4). The sample was imaged under the same laser intensity at five different regions of interest (ROIs) sized 5.4 μm × 5.4 μm distributed across the full illuminated area. The size of each ROI matches the average laser speckle size at the sample plane.The positions of the ROIs are indicated in Fig. 2.2 (c). Fig. 2.1 (e) shows the average photon count per localization and the localization precision which reflect the excitation intensity in each ROI. The spatial consistency of photon counts and localization precision across all ROIs demonstrates homogeneous excitation over the full illuminated field of view, ensuring spatially invariant resolution performance. The diode laser at 638 nm also provides equal homogeneity on the sample plane, using dSTORM sample with Alexa 647 dyes, shown in Fig. 2.8 in Section 2.8.

2.2.2. Home-built TIRF microscope body with large FOV and dual-channel detection

MiCube [11] is an open-source microscope body frame which we adopted for its mechanical stability, accessibility and customizability in comparison to commercial microscopes. It is compatible with brightfield imaging, widefield epifluorescence, highly inclined and laminated optical sheet (HILO) and total internal reflection fluorescence (TIRF) microscopy [16]. TIRF is an effective optical sectioning method typically used to illuminate molecules immobilized on the coverslip or to visualize cellular structures on or in the vicinity of cell membranes at a high signal-to-background ratio (SBR). A small focused excitation beam size at the back focal plane (BFP) of a high-NA objective is critical to enabling TIRF. In practice, the TIRF condition is typically achieved by using a single mode laser with a small beam diameter, or by laser delivery through single mode optical fibers. Lam et al.[9] showed that instead of single mode lasers or single mode fibers, a collimated beam from an MMF with a small core sized 70 μm × 70 μm can be focused by a focusing lens (FL) of 125 mm focal length to meet the TIRF condition.

On the other hand, a large field of view (FOV) in microscopic imaging is highly favorable for high-throughput imaging and studying cell-cell interactions when multiple

targets need to be visualized simultaneously. The availability of sCMOS cameras with large sensor areas has eliminated detection optics as a limiting factor for FOV size. Instead, a large illumination area in the sample plane is desirable for increasing the FOV size, which can be realized by enlarging the excitation beam diameter. However, the beam size is restricted by both the TIRF condition and the physical size of the optical components. Our design, combining the 70 μm × 70 μm core size MMF and a 150 mm focusing lens, results in a large illumination area of 210 μm × 210 μm, while preserving TIRF condition. The calculation for TIRF viability is given as follows according to the method reported in Kwakwa et al.[10]

The width of the TIRF annulus S_a at the back focal plane of the objective is defined by:

$$S_a = \mathrm{EFL} \times (\mathrm{NA} - n_s) \tag{2.1}$$

where EFL is the effective focal length and NA is the numerical aperture of the objective, and n_s is the refractive index of the sample, in this case equals 1.335 for PBS buffer. Our 60× oil objective with EFL of 3 mm and NA of 1.5 leads to S_a = 495 μm which dictates the critical beam size for TIRF.

The theoretical focused beam size S_b is calculated as:

$$S_b = S_c \times F_k / F_{cl} \tag{2.2}$$

where S_c = 70 μm is the MMF core diameter, and the F_{cl} = 30 mm is the MMF collimation lens focal length, leading to S_b = 350 μm, smaller than the critical size S_a, thus allowing the realization with TIRF in our design.

The original miCube employs a 200 mm focusing lens that focuses the excitation beam onto the back focal plane. With the objective effective focal length being 3 mm, using 150 mm reduces the de-magnification factor of the excitation beam diameter from 66.7× to 50×, thus effectively increasing the illumination area in the sample plane. To accommodate the 150 mm focusing lens in our design, we reduced the width of the miCube to 80 mm (Fig. 2.2 (a)) in order to place the focusing lens closer to the miCube. Switching of the illumination modalities between epi-, HILO and TIRF is conveniently enabled by a motorized linear stage on top of which the focusing lens is mounted. The modified miCube accommodates a fixed 60× high-NA objective (UPLAPO60XOHR, Olympus) at the top. A compact sample-positioning stage (three CLS5252 assembled, SmarAct) providing nanometer precision and 31 mm travel range in each axis, is also mounted on top of miCube with an adapter plate in between (customized cut from aluminum, CAD available). The adapter plate extends above the miCube's top surface and functions as the base for the enclosure needed for environmental control (customized cut acrylic plate, CAD available). The sample stage is compatible with a standard circular sample (25 mm diameter) or rectangular sample (35 mm × 76 mm) by attaching corresponding sample holder adapters to the stage.

To gain the flexibility to choose between a large FOV size and a high illumination intensity, a beam size reducer consisting of two achromatic lenses in a telescope configuration that halves the beam diameter can be added after the collimation lens at the MMF output. With the simple insertion or removal of the beam size reducer, the FOV can be switched between the small and large configuration easily. The halved beam size

translates to a quartered FOV size and a four times higher power density at the sample plane, facilitating dSTORM and other power-demanding wide-field imaging. Table 2.1 shows the laser intensity measured at the sample plane at the large and small FOV sizes. Raw images from single molecule imaging experiments in small and large FOV settings are shown respectively in Fig. 2.2 (b) and Fig. 2.2 (c). The higher intensity in small FOV enables the sparse blinking condition in dSTORM imaging of microtubules (Fig. 2.2 (b), detection in red channel), while the large FOV is suitable for DNA-PAINT imaging where more cells are visualized at the same time (Fig. 2.2 (c), detection in green channel).

	405 nm	**488 nm**	**561 nm**	**638 nm**
Transmission efficiency from MMF exit to sample plane	64%	85%	91%	73%
Maximum power at sample plane (mW)	228	1600	594	964
Sample plane max. intensity (Large FOV, kW/cm^2)	0.51	3.63	1.35	2.14
Sample plane max. intensity (Small FOV, kW/cm^2)	2.07	14.51	5.39	8.58

Table 2.1: **Sample plane excitation intensity at the two different FOV configurations**. The maximum laser power of each wavelength is measured directly above the objective under epi-illumination. The value is also used to calculate the transmission efficiency between the sample plane and the MMF exit. To calculate the maximum sample plane intensity, the actual illuminated FOV size is measured by imaging a dense fluorescent beads sample under epi-illumination. Note that the measured FOV sizes are smaller than the theoretical size determined by the excitation optics (approximately 210 × 210 μm^2 instead of 264 × 264 μm^2 for the large FOV configuration, and 105 × 105 μm^2 instead of 132 × 132 μm^2 for the small FOV configuration), due to measurement error and the non-collimated component in the MMF output.

Next, we evaluated the effectiveness of TIRF by imaging microtubules in the same cell under different illumination modalities (Fig. 2.2 (d)). Fewer structures are visible due to TIRF's optical sectioning effect. At the same laser power and exposure time, TIRF displays higher SBR (2.0 ± 0.3) than epi-illumination (1.3 ± 0.2).

Multicolor imaging expands the palette of usable fluorophores and enables simultaneous visualization of different molecules which is essential for studying complex cellular structures, protein interaction and cellular dynamics. The detection path of Open Blink is configured as dual-channel, split by a dichroic mirror at 595 nm (ET595/50, Chroma). The two channels are imaged side by side on an sCMOS camera (BSI Express, Photometrics) after a 4f relay optics. Final magnification measures at 59.9 ×, corresponding to a camera pixel size of 108.4 nm. An adjustable aperture is placed at the focal point of the tube lens (TTL180-A, Thorlabs) to restrict the image size per channel to half of the camera chip size. We showcase two-color imaging in the Supplementary Fig. 2.10. The full schematic layout of the microscope can be found in Supplementary Fig. 2.5 and Fig. 2.6.

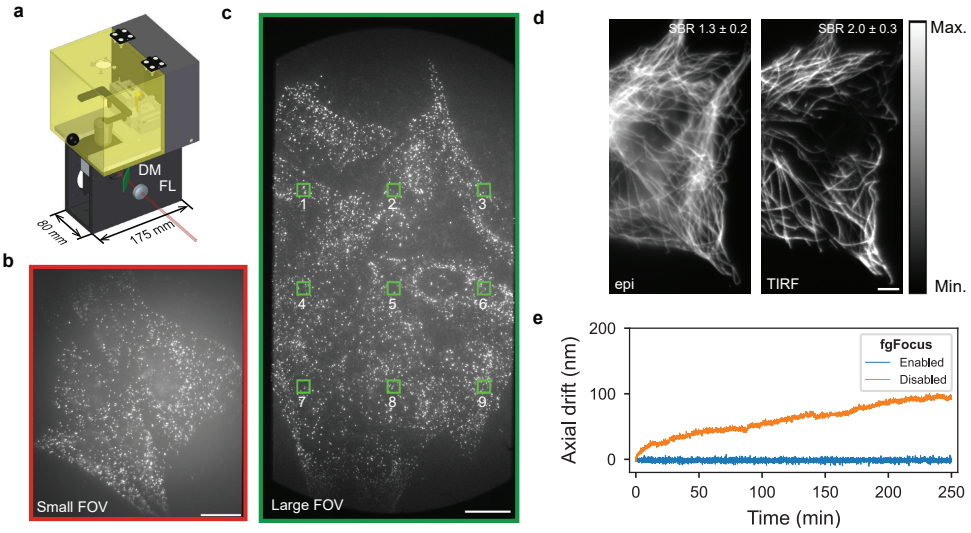


Figure 2.2: **A compact microscope body with large FOV and focus-lock module.** **(a)** CAD representation of the modified MiCube with reduced width, accommodating 150 mm focusing lens (FL) and infrared dichroic mirror (DM). The customized adapter plate serves as the base for the enclosure. **(b)** Raw dSTORM image frame in small FOV setting, showing microtubules in U2OS cells labeled with Alexa Fluor 647. Scale bar = 20 μm. **(c)** Raw DNA-PAINT image frame in the large FOV setting, showing microtubules in U2OS cells labeled with Cy3B imagers, Scale bar = 20 μm. **(d)** Comparison of cell images under epi- (left) and TIRF illumination (right), showing microtubules in COS-7 cells labeled with Alexa Fluor 647 under low illumination intensity. Color bar indicates display from minimum to maximum gray values (145-18233 for epi, 86-1893 for TIRF). Scale bar = 5 μm. Images were taken with identical laser power and exposure time. **(e)** Comparison of axial drift over 250 minutes with and without focus-lock module *fg*Focus.

2.2.3. Active focus stabilization

Super-resolution imaging based on single molecule blinking often requires tens of thousands of frames, leading to long acquisition times, during which focus drift may compromise the imaging quality. An active focus-lock system is beneficial for long time-lapse and automated super-resolution imaging. We implemented a focus-lock module *fg*Focus, short for 'fairly good' and adapted from *pg*Focus and *qg*Focus [16, 20]. Maintaining of the focus is realized by coupling an infrared beam using a dichroic mirror to the microscope excitation path in TIRF configuration. The reflected infrared beam can be detected by a one-dimensional sensor array (TSL1401-DB, Parallex) and is used to determine the sample z-position. The shift of the infrared beam position on the sensor induced by sample drift is fed into a proportional–integral–derivative (PID) controller, which actuates the sample z-stage to compensate for the drift. In our design, the 150 mm focal length of the focusing lens for TIRF poses a challenge to fit in the dichroic mirror in between the focusing lens and the MiCube, since the original MiCube has a focusing lens at 200 mm for TIRF. We thus used a compact kinematic mirror mount (KMS/M, Thorlabs) onto which the dichroic mirror is fixed with silicone glue. *fg*Focus is made compatible with μManager and detailed in Section 2.3. The stability of *fg*Focus is demonstrated by imaging a fluorescent bead slide (T14792, Thermo Fisher) over 250 minutes. The drift of the focus reported by the infrared detector at an exposure time of 1 ms is traced every 2 seconds, both with and without the activation of *fg*Focus. While enabling *fg*Focus, no drifting of focus was visually observable during the experiments, with the measured axial drift averages at –1.58 nm (± 2.00 nm standard deviation), significantly improved compared to the non-enabled case where the final axial drift accumulated to 94.2 nm, demonstrating nanometric axial stability over multi-hour acquisitions required for quantitative SMLM (Fig. 2.2 (e)).

2.3. Control software development

2.3.1. Microscope control scheme

μManager is an open-source microscope control software integrating core microscopy functionalities such as stage control, camera settings and image acquisition tasks in its default graphic user interface (GUI). μManager supports a wide range of hardware components through the so-called device adapters that bridge hardware and software. The ease of use and flexibility of this modular approach to adapt customized microscopes motivated us to integrate full control and image acquisition for Open Blink in μManager. In addition, μManager is available under open source license for all common operating systems (Windows, Mac and Linux) and based on the widely used image processing environment ImageJ, which is particularly popular in the bioimaging community that we target as end users of Open Blink.

Although most components used in Open Blink from mainstream manufacturers come with device adapters for μManager, which include the sample stage, TIRF stage and sCMOS camera, the customized parts, i.e. the laser combiner, vibrational motor, and the infrared detection and z-stage feedback for *fg*Focus at Open Blink require tailored solutions taking care of both the control electronics and communication with μManager. Each device demands different types of control signals. The speed of

the vibrational motor can be controlled by pulse width modulation (PWM) signals. Specifically, the intensity of all lasers is modulated by 0–5 V analog voltages. *fg*Focus, which relies on analysis of the beam profile detected by the infrared detector, needs to receive an analog readout from the infrared sensor. To achieve this, we employed two micro-controllers, which output or read appropriate signals to or from the devices through serial communication with μManager (Fig. 2.3 (a)). Micro-controller 1 is the controller for the laser combiner. A customized PCB integrates a Raspberry Pi Pico, three 12-bit dual-channel digital-analog-converters (DACs) and a MOSFET transistor. The DACs convert the digital signal from the micro-controller into analog voltages to the laser drivers, and the MOSFET modulated by the PWM signal is wired to the vibration motor, facilitating homogeneous illumination. Micro-controller 2 is a thumb-sized lower-power board (XIAO SAMD21, Mouser Electronics) which sends to μManager the analog signal read from the infrared sensor board (TSL1401-DB, Parallax). Both micro-controllers are connected to the computer via USB connection. The PCB design and configuration of both boards are available at https://github.com/GrussmayerLab/LaserController and https://github.com/GrussmayerLab/fgFocus, respectively.

2.3.2. μManager integration

For software integration, existing device adapters of micro-controllers for μManager do not support general DAC output [31]. Commercial data acquisition cards compatible with μManager are pricey and vastly exceed the requirements for simple analog signal generation. They also lack the essential ability to write metadata, which is an advantage of integrating all instrumental control in one place in order to record the relevant device parameters in parallel with the image acquired in μManager. For the laser and vibrational motor controller, we bypass the typical hardware configuration in μManager, and instead use a plugin within the Easier Micro-manager User interface (EMU) [23] facilitating metadata writing in a straightforward GUI (Fig. 2.3 (b)). The 0-100 % range of adjustment corresponds to 0–5 V output of the DACs. We recommend full-range calibration of laser power when using the controller for lasers with analog modulation, as we observed a slight nonlinear deviation for the diode lasers (Supplementary Fig. 2.9).

We provide a similar solution for *fg*Focus software which is the first μManager compatible focus-lock module for the increasingly popular SmarAct sample stage [16, 18, 32–34]. Through an EMU plugin, shown in Fig.2.3 (c), the *fg*Focus GUI displays the reflected beam profile with adjustable exposure time and averaged frame number when *Enabled*. The detected beam is fitted by a Gaussian function using nonlinear least-squares optimization in order to determine its centroid pixel position μ. When in focus, *Calibrate* function scans the z-stage over a ± 1 μm range in 5 steps around the focus position and determines the linear relationship between the axial position and the position of the reflected IR beam on the sensor. After the calibration, the z-stage returns to the focus axial position. Once *Lock* is enabled, the Gaussian centroid at the current focal position is stored as the reference as μ_{ref}. During the closed-loop operation updated every 2 s, each newly acquired sensor profile position, μ_{k}, is compared against the reference to calculate the focus error as $e_{\mathrm{k}} = \mu_{\mathrm{k}} - \mu_{\mathrm{ref}}$. This error is processed by a proportional–integral–derivative (PID) control logic whose parameters configurable within the plugin (we used Kp = 0.71, Ki = 0, and Kd = 0). The actual focus drift is also

displayed in the GUI as *Distance*, converted from the error e_k using the calibration factor. Both EMU plugins for the laser combiner controller and *fg*Focus are pre-compiled and downloadable for immediate use in μManager 2.0 (tested in nightly build 2.0.3, 20250318 version, on Window 10 machine) in the aforementioned repositories.

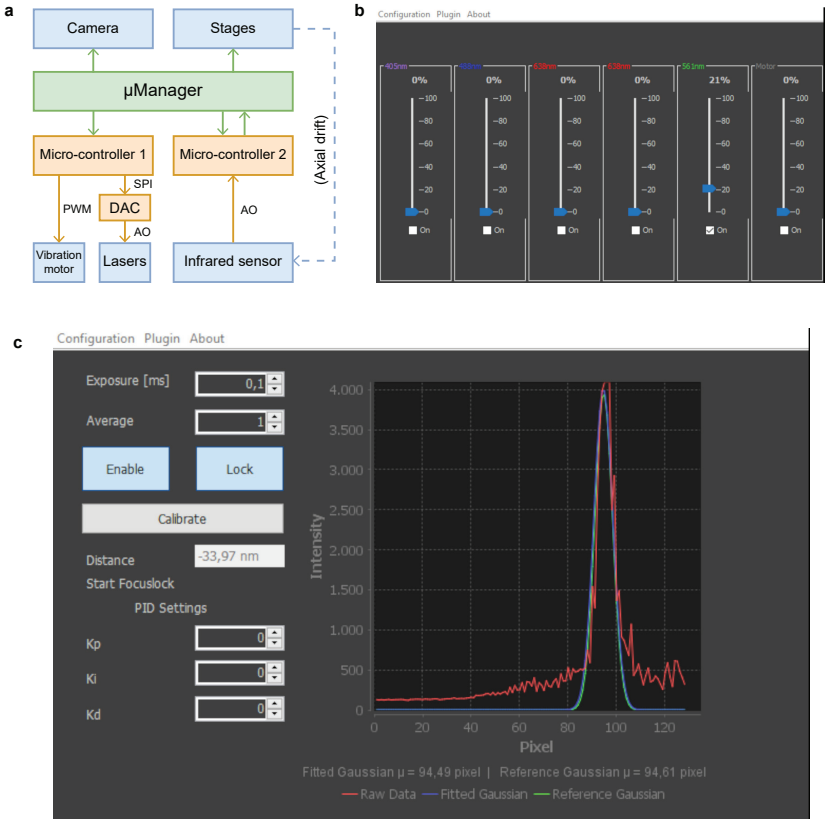


Figure 2.3: **Open Blink integration in μManager. (a)** Control scheme for customized components. Micro-controller 1 controls the laser intensity and vibrational motor speed of the laser combiner; micro-controller 2 reads the intensities from the infrared sensor and provides them as input to the PID-based focus-lock module, which maintains the axial focus by continuously adjusting the sample z-stage in a closed feedback loop. **(b)** Laser controller plugin interface in μManager. Laser power and vibrational motor speed can be adjusted by the sliders; **(c)** *fg*Focus plugin interface in μManager, which displays the infrared beam profile. Distance shows drift of focus. Infrared sensor and PID controller parameters are configurable.

2.4. Verification with single molecule super-resolution imaging

Super-resolution imaging based on localizing single molecules relies on the sparse blinking condition of fluorophores, often enabled by high-intensity illumination as in dSTORM [28]. We showcase the compatibility and versatility of Open Blink with three types of single molecule super-resolution imaging applications that have different illumination requirements: dSTORM, DNA-PAINT and SOFI for 2D high-resolution imaging of microtubules in fixed cells. Typical dSTORM fluorophores such as Alexa Fluor 647 require high laser power in combination with an oxygen scavenger and thiol buffer system to induce blinking [26, 27], i.e. on- and off- switching of fluorescence. Therefore, we used the small FOV configuration in the excitation path at 1.2 kW/cm^2, resulting in sparse single-molecule imaging and reaching a localization precision of 6.81 nm, consistent with the expected photon-limited precision under high-power excitation (Fig. 2.3 (a)). DNA-PAINT uses the reversible hybridization of DNA oligos, namely the docking strand coupled to the imaging target and the imager strand that is supplied in solution at low concentration, to achieve single-molecule binding events [35]. It does not require light to induce blinking, but suffers from background noise arising from the imagers carrying fluorophores floating around the sample, and thus necessitates TIRF illumination for optimal performance. Fig. 2.4 (b) shows a DNA-PAINT image using Cy3B imagers matching the P1 docking strand under the TIRF illumination and the large FOV configuration, with localization precision estimated at 9.43 nm, despite operating under large-FOV TIRF illumination conditions.

SOFI does not require localization of individual molecules and instead improves the resolution n times by n-th order cumulant analysis of fluorescence fluctuation [6], making it particularly advantageous analyzing densely and rapidly blinking data. Using the blinking speed-optimized DNA-PAINT docking strand 5×R1 and a high imager strand concentration at 20 nM [36], we could reconstruct a 2nd-order SOFI with 500 frames of dense and fast blinking data, in the same fashion proposed in Chapter 3. By scanning through a large FOV consisting of a 4 by 4 grid using μManager's multi-position acquisition, high-throughput super-resolution imaging was achieved after stitching the 2nd-order SOFI images reconstructed from each grid, shown in Fig. 2.4 (c). The stitched FOV size is 0.23 mm × 0.23 mm and was acquired within a total camera exposure time of 80 ms.

2.5. Discussion

Open Blink bridges the gap between state-of-the-art quantitative super-resolution imaging performance and broad accessibility. By combining experimentally validated optical performance, including homogeneous large-field illumination, sub–10 nm localization precision, and nanometric axial stability over multi-hour acquisitions, with modular and cost-effective hardware, we demonstrate that high-end SMLM capabilities are not inherently restricted to proprietary commercial platforms. Rather than prioritizing affordability at the expense of performance, Open Blink was designed to maintain the key optical requirements for quantitative single-molecule localization microscopy while reducing technical and financial barriers for adoption.

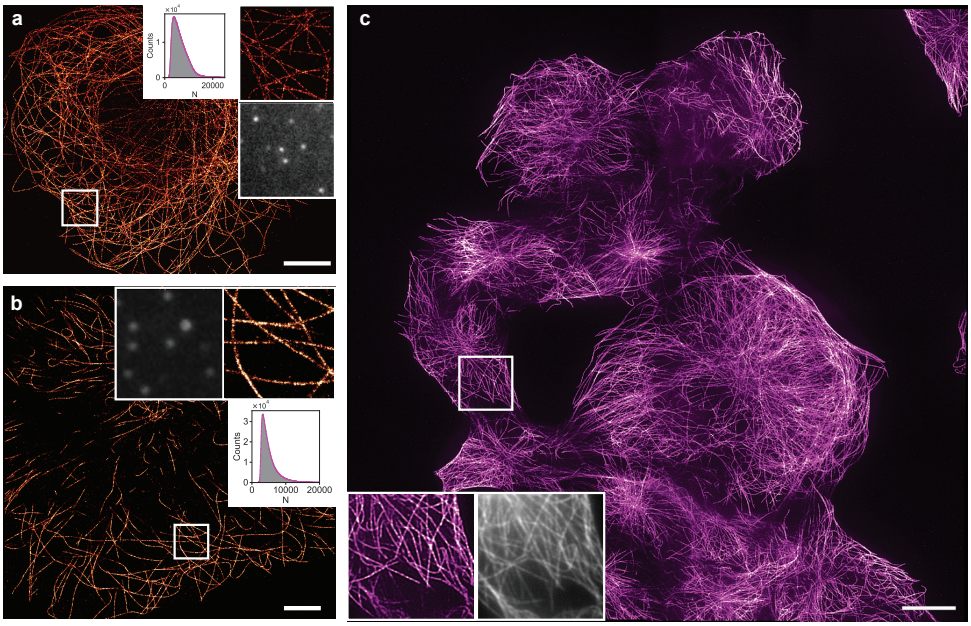


Figure 2.4: **Super-resolution images of microtubules in fixed COS-7 cells by Open Blink.** Each image includes a zoom-in area (colored) and a raw image frame of the same ROI (grayscale). **(a)** dSTORM with label of Alexa Fluor 647. 10 000 frames at 70 ms exposure time and 1.2 kW/cm^2 laser intensity at 638 nm. Inserted plot shows the photon distribution per localization. Localization precision = 6.81 nm, scale bar = 10 μm; **(b)** DNA-PAINT with label of P1 docking strand. 10 000 frames at 100 ms exposure time and 0.39 kW/cm^2 laser intensity at 561 nm. The inserted plot shows the photon distribution per localization. Localization precision = 9.43 nm. Scale bar = 5 μm; **(c)** 2nd-order SOFI with label of 5×R1 DNA-PAINT docking strand, stitching of 4 by 4 tiles, each tile reconstructed with 500 frames at 10 ms exposure time and 0.59 kW/cm^2 laser intensity at 561 nm. Scale bar = 20 μm.

The compact quad-line laser combiner provides uniform high-power excitation for SMLM while enabling homogeneous excitation conditions compatible with spatially consistent localization performance. In addition, it can serve as an add-on excitation source to upgrade a conventional wide-field microscope for super-resolution microscopy, or to enable imaging methods that benefit from homogeneous high-power illumination, such as quantitative fluorescence imaging and single-particle tracking. The affordable diode lasers contribute largely to the overall cost reduction of Open Blink, which could be further lowered with emerging green semiconductor laser sources.

Previous implementations of miCube in TIRF microscopy used single mode lasers. We showed the compatibility of TIRF illumination with multimode optical fibers in miCube by reducing its width and using a shorter 150 mm lens, which simultaneously enlarges the field of view size. The smaller MiCube led to our design of an adaptation plate for both the sample stage and an enclosure chamber without interfering with the optics around the body. This allows the straightforward adoption of environmental control for future live-cell imaging, for example with previously reported cost-effective open solutions [37]. The diode lasers supporting up to 500 kHz modulation could potentially enable sub-frame control for stroboscopic imaging applications.

The complete integration of Open Blink in μManager is a main advantage for users who wish to avoid programming work for microscope control and image acquisition. The firmware and the μManager plugin for our laser control can be readily generalized to control any device from μManager that supports 0–5 V analog modulation or pulse-width modulation through a micro-controller. The plugin enabled metadata writing, addressing this limitation of previous micro-controller plugins available for μManager. Our infrared laser based *fg*Focus fills the missing gap of a μManager compatible focus-lock module. The *fg*Focus firmware and plugin can be easily transferred to other sample stages with an application programming interface (API) similar to that of the SmarAct stages. With the large library of hardware plugins existing for μManager, Open Blink can be deployed as a platform for highly automated smart microscopy [38, 39]. On-the-fly image analysis and microscopy control require informed image acquisition. We prepare Open Blink for these applications with metadata that represents device status and acquisition parameters. For example, the laser power and TIRF stage position associated with each single molecule image can be used to actively modulate the blinking density of single fluorophores.

At substantially reduced cost around 70 000 euros, approximately one quarter of a commercial system for single-molecule localization microscopy, Open Blink demonstrates performance metrics comparable to high-end commercial systems in dSTORM, DNA-PAINT and SOFI imaging. We designed customized mechanical parts for simple in-house machining, whereas the electronics are ready-to-order with PCB files. The remaining high-cost components, such as the high-NA objective, sCMOS camera, and the nanometer-precision sample stage, can be replaced by lower-cost alternatives for specific applications that tolerate the trade-off performance limitations [13, 40].

In summary, Open Blink demonstrates that high-performance quantitative single-molecule super-resolution microscopy can be made broadly accessible without compromising optical quality. By pairing validated optical performance with modular, affordable hardware and fully integrated open-source software, Open Blink lowers the barrier for laboratories to adopt state-of-the-art SMLM techniques. With comprehensive

documentation and ready-to-use software, Open Blink not only expands access to super-resolution microscopy but also encourages innovation and development within the open hardware and software community.

2.6. Materials and Methods

Laser combiner construction

All lasers mentioned in Section 2.2.1 are mounted on a custom-cut aluminum heat sink, which adjusts all beams to the same height of 70 mm. Thermal paste is applied between the laser base plate and the heat sink to ensure efficient heat transfer. The lasers are positioned in parallel in the order of wavelength. Two 638 nm lasers are oriented perpendicular to each other and are combined into a single beam by a polarizing beam splitter (PBS251, Thorlabs) mounted on a kinematic mount (KM100PM/M, Thorlabs). Three longpass dichroic mirrors (DMLP425/DMLP550/DMLP605, Thorlabs) on kinematic mirror mounts (MDI, Radiant Dyes) sequentially combine beams of different wavelengths.

The combined beam is launched into an MMF (NA 0.22, square core profile of size 70 μm by 70 μm, customized, Ceram Optec) with an FC/PC connector (SM1FC, Thorlabs) via a 19 mm aspherical lens (AC127-019-A, Thorlabs) which is mounted in an adjustable lens tube (SM05V10, Thorlabs). Homogeneity via MMF agitation is facilitated with the use of a vibrational motor (5mm – 11mm Type, 304-111, precision microdrives) in proximity to the optical fiber within a 3D printed mount (customized, CAD available). The laser beam is coupled out by a FC/PC connector, after which an achromatic lens of 30 mm (AC254-030-A-ML, Thorlabs) collimates the beam before a laser clean-up filter (ZET 405/488/561/640xv2, Chroma) removing the autofluorescence from the MMF. Collimation is achieved by adjusting the distance between the achromatic lens and the FC/PC connector until the diameter of the laser beam remains unchanged over long distances (> 2 m).

After the collimation lens, the beam size reducer consisting of two aligned achromatic lenses can be used for the small FOV configuration. The two lenses (AC254-050100-A-ML and ACN254-050-A, Thorlabs) mounted in lens tubes can be screwed onto two cage plates (CXY1A, Thorlabs) on the same cage assembly where the MMF adapter and the laser collimation lens are mounted, such that beam size is halved in diameter and remains collimated and aligned along the optical axis. When a larger FOV is needed, the two lenses can be taken down without changing the cage plate positions.

Microscope construction

The construction of Open Blink after the MMF exit is described as follows. In the excitation path, the collimated excitation beam is walked by two elliptical mirrors (BBE1-E02, Thorlabs), after which a 150 mm achromatic lens (AC254-150-A-ML, Thorlabs) focuses the beam onto the BFP of the objective. The precise positioning of the beam on the back focal plane of the objective is facilitated by a linear motorized stage (KMTS25E/M, Thorlabs) where the second elliptical mirror and the 150 mm focusing lens are mounted upon. Sample stage with nanometer precision (assembled with three

identical linear stage, CLS5252, SmarAct) is mounted on a customized adaption plate (aluminum, customized, CAD available) on top of the modified MiCube (aluminum, customized, CAD available). An oil objective (UPLAPO60XOHR, Olympus) is screwed down at a fixed position. Fluorescence collected by the objective is decoupled by a quad-band dichroic mirror (zt405/488/561/640rpc, Chroma) mounted below (DFM1/M, Thorlabs) the objective and inside the miCube. A right angle mirror (KCB1E/M, Thorlabs) directed the fluorescence to be focused by the 180 mm tube lens (TTL180-A, Thorlabs) forming the intermediate image. At the focus of the tube lens, an adjustable slit (VA100/M, Thorlabs) is placed in order to restrict the image size for dual-color imaging. A quad-band filter before the tube lens (ZET405/488/561/640mv2, Chroma) filters out residual excitation light.

Further, the detection path features a dual-channel scheme. A 300 mm achromatic lens (G322336322, Qioptiq) in 4f configuration with the tube lens creating the optical infinity space, allowing for insertion of a long pass dichroic mirror (ZT640rdc-UF3, Chroma) for color splitting, and of a square mirror (BBSQ1-E02, Thorlabs) for maximum collection of the fluorescence passing through the dichroic mirror. Both the dichroic mirror and the mirror are glued on a compact kinematic mount (KMS/M, Thorlabs) with silicone glue (Twinsil, Picodent). The two channels both include a 300 mm achromatic lenses (G322336322, Qioptiq) focusing the short- and long wavelength images side by side onto the sCMOS camera (BSI Express, Teledyn Photometrics). In order to co-focus the two channels, the achromatic lens in the long-wavelength channel is mounted onto a small dovetail stage (DT12/M, Thorlabs), allowing for fine adjustment along the optical axis. Proper bandpass filters can be inserted in either channel according to the fluorophore used.

The focus-lock module *fg*Focus utilizes an 830 nm infrared laser (CPS830S, Thorlabs) at TIRF configuration whose reflection on a linear sensor indicates the position of the sample plane. The infrared beam is first focused by a plano-convex lens (LA1908-B-ML, Thorlabs) and relayed by two mirrors (BBE1-E03, Thorlabs), the second one of which is translated by a 1D manual stage (DTS25/M, Thorlabs) for TIRF. The beam is then coupled into the microscope by a dichroic mirror (zt 775 sp-2p, AHF) overlapping the main excitation path after the TIRF focusing lens. The reflected infrared beam from the sample is decoupled by a 50/50 beam splitter (CCM1-BS014/M, Thorlabs) before being further filtered and focused onto the detection PCB. The reduced MiCube size means less space left in between the excitation TIRF focusing lens and the microscope body, posting challenges into inserting a dichroic mirror coupling the infrared beam into the microscope. We solved this by gluing the dichroic mirror with silicone glue onto a compact kinematic mirror mount (KMS/M, Thorlabs).

Sample preparation

Cell culture and immunostaining

U2OS cells and COS-7 cells (DSMZ GmbH) were cultured in Dulbecco's modified Eagle medium (DMEM) in high glucose (Thermo Fisher) with the addition of 10% fetal bovine serum (FBS; Gibco, Thermo Fisher), 1% L-glutamine (Gibco, Thermo Fisher), 1% sodium pyruvate (Gibco, Thermo Fisher), and 1% penicillin-streptomycin (Gibco, Thermo Fisher).

Cells were seeded one day before immunostaining on coverslips (#1.5 type, Carl Roth) within 6-well plates filled with the culture medium at 37°C and 5% CO_2.

24 h after seeding, the cells were firstly treated for 90 s at room temperature in a pre-warmed extraction buffer which bases on the microtubule-stabilizing buffer Kapitein (80 mM PIPES, 7 mM $MgCl_2$, 1 mM egtazic acid, 150 mM NaCl, 5 mM d-glucose) with addition of 0.3% (v/v) Triton X-100 and 0.25% (wt/vol) glutaraldehyde. After the removal of the extraction buffer, the cells were fixed by the fixation buffer containing 4% (wt/vol) paraformaldehyde in PBS for 10 min at room temperature, followed by three 5-min washes with PBS on an orbital shaker. To quench the autofluorescence, the fixed cells were treated for 7 min under 10 mM freshly dissolved sodium borohydride in PBS and immediately rinsed with PBS before two more 10-min washes. The fixed cells were then permeabilized with 0.25% (v/v) Triton X-100 in PBS for 7 min and then washed for three times with PBS. Afterwards, the cells were blocked for an hour at room temperature with blocking buffer containing 2% (wt/vol) bovine serum albumin, 10 mM glycine, and 50 mM NH_4Cl.

Cells were firstly immunostained with primary antibody against α-tubuluin at 200 times dilution (T5168-.2ML, Merck). For dSTROM in Fig. 2.4 (a), cells were then incubated with anti-mouse secondary antibodies conjugated with Alexa Fluor 647 (A-31571, Thermo Fisher); For DNA-PAINT in Fig. 2.4 (b), cells were incubated with anti-mouse secondary antibody conjugated with P1 docking strand (sequence 5'-3', TTATACATCTA, Massive Photonics). For DNA-PAINT-SOFI in Fig. 2.4 (c), cells were incubated with anti-mouse secondary nanobody conjugated with 5×R1 docking strand(sequence 5'-3': TCCTCCTCCTCCTCCTCCT). Site-specific secondary nanobody conjugation with the docking strands is described in [41] and Chapter 3. Both secondary nanobodies and antibodies were diluted 200 to 300 times with the blocking buffer and applied to the fixed cells on coverslips for a one-hour incubation at room temperature, followed by three 5-min washes with blocking buffer. Finally, samples were incubated for 15 min in post-fixation buffer (2% paraformaldehyde in PBS), and stored in PBS at 4°C until imaging.

Imaging buffer and imaging acquisition

Fixed cells were imaged at room temperature in imaging buffer. For dSTORM imaging, GLOXY buffer with the following components was made freshly on the day of imaging: 33 mM cysteamine, 500 μg/mol glucose oxidase, 40 μg/mL catalase, 10% (w/v) glucose in 50 mM Tris buffer. For DNA-PAINT imaging, buffer consists of 1nM P1 imager (sequence 5'-3': AGATGTAT-Cy3B) in PBS with 500 mM NaCl. For DNA-PAINT-SOFI imaging, buffer consists of 20nM R1 imager (sequence 5'-3': AGGAGGA-Atto655) and 5% ethlyne carbonate in PBS with 500 mM NaCl. Imaging acquisition is through μManager 2.0. For the large FOV DNA-PAINT-SOFI image, 4 by 4 tiles are acquired through multi-position acquisition function with 10% pixel overlap.

Data analysis

SMLM reconstruction

SMLM reconstruction for DNA-PAINT and dSTORM data was done in Picasso software (v0.9.5) using least-squares Gaussian fitting [35, 42]. Photon count per localization is

extracted from the Picasso Localizer output. In detail, the camera pixel value is first converted to photon units as in

$$P_{ij} = \frac{(C_{ij} - B) \times S}{G} \tag{2.3}$$

where C_{ij} is the raw pixel value, P_{ij} is the converted value, B is the camera baseline, S is camera sensitivity and G is EM gain. For each detected localization, a two-dimensional Gaussian plus a constant background b is used for fitting:

$$M_{ij} = \frac{N}{2\pi\sigma_x\sigma_y} \exp\left[-\left(\frac{(x_j - x_0)^2}{2\sigma_x^2} + \frac{(y_i - y_0)^2}{2\sigma_y^2}\right)\right] + b \tag{2.4}$$

with N being the total photon count per localization. The parameters of the fitting, $\theta = (x_0, y_0, N, b, \sigma_x, \sigma_y)$, are found by minimizing the unweighted sum of squared residuals between M_{ij} and P_{ij} as in $\chi^2(\theta) = \sum[P_{ij} - M_{ij}(\theta)]^2$, giving the N values.

Images are subjected lateral drift correction using redundant cross correlation (RCC) embedded in Picasso Render [43]. Localization precision is estimated by Picasso's integrated nearest-neighbor analysis (NeNA) [44]. For each localization at frame t, the distance to localizations in frame $t+1$ is calculated as $d = \sqrt{(x_{t+1} - x_t)^2 + (y_{t+1} - y_t)^2}$. If d is considered from the same stationary emitter, it follows the distribution $p(d) = \frac{d}{2s^2} \exp\left(-\frac{d^2}{4s^2}\right)$, where s is the Gaussian localization uncertainty. NeNA fits the histogram of the next-frame nearest neighbor distance d, and the fitted parameter s is then multiplied by the pixel size, giving the estimated localization precision in nanometer. For dSTORM imaging, raw data frames were first subjected to a Fast Temporal Median Filter before SMLM reconstruction [32].

SOFI reconstruction

SOFI reconstruction was carried out with customized MATLAB script available in `https://www.github.com/kgrussmayer/sofipackage` for individual tile in the large FOV acquisition, afterwards SOFI images were stitched together by the *Stitching* plugin on ImageJ software. The plugin takes into account of the pixel overlap between tiles and uses linear blending for fusion.

Microtubule SBR quantification

Signal-to-background ratio was quantified from the raw images of microtubules under epi- or TIRF illumination in ImageJ. Five filaments of microtubules (average length 4.2 μm ± 1.5 μm) were manually selected using the line segmentation tool in ImageJ with a width of 4 pixels. For each filament, the mean fluorescence intensity was measured along the line segmentation as the signal, while the local background was measured using the parallel ROIs positioned on either side of the filament. SBR was calculated as the ratio between the signal intensity and the averaged background intensity.

2.7. Data Availability

A virtual CAD model of Open Blink, a detailed list of components used and their prices, design files of the customized parts related to Open Blink,

as well as raw image data underlying Fig. 2.4, are available in the online repository 4TU.ResearchData under the license CERN-OHL-S-2.0. An overview of the project is hosted at Grußmayer Lab GitHub page. μManager plugins with instructions are available at https://github.com/GrussmayerLab/LaserController and https://github.com/GrussmayerLab/fgFocus.

2.8. Appendix

Supplementary figures

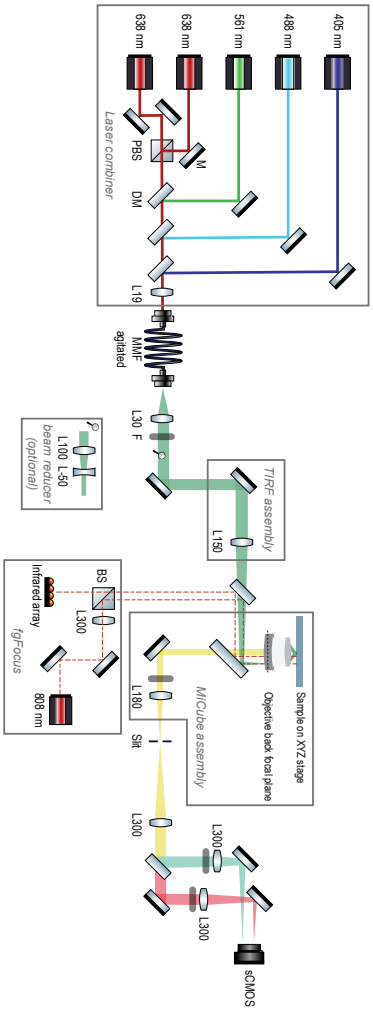


Figure 2.5: **Optical path of Open Blink.** M: mirror. BS: beam splitter. PBS: polarized beam splitter. DM: dichroic mirror. F: filter. MMF: multimode fiber.

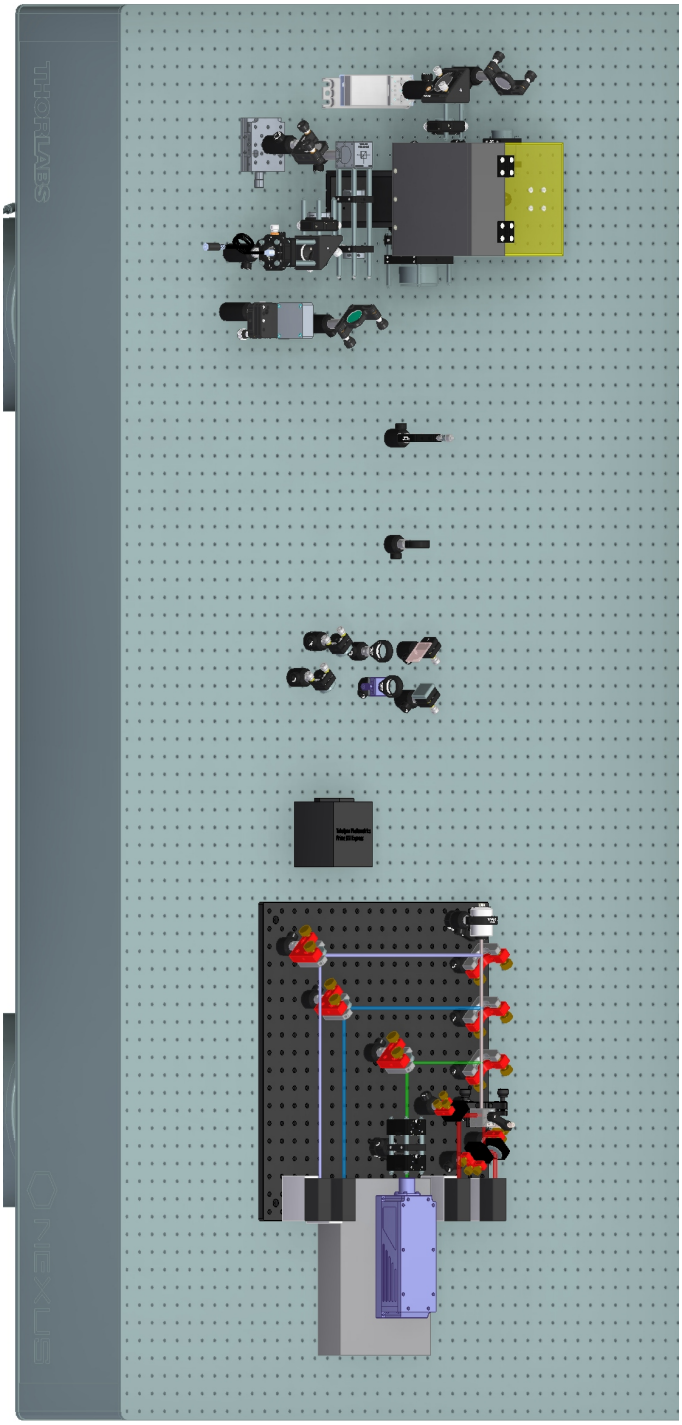


Figure 2.6: Virtual model of Open Blink. Optical fiber and enclosures are not shown.

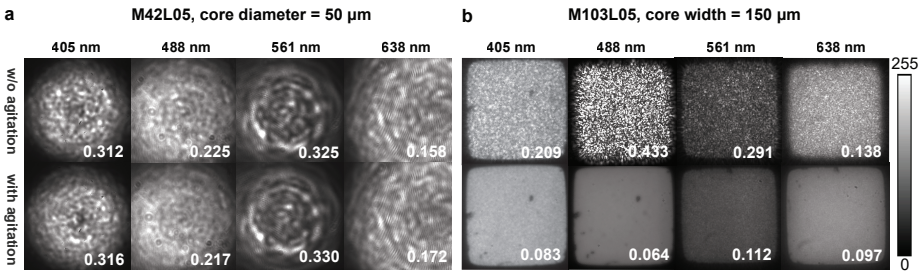


Figure 2.7: **Two alternative multimode fibers (MMFs) respond differently to the agitation.** Images taken at the MMFs exits show laser intensity profiles at different wavelengths in the presence and absence of agitation. Left: circular-core MMF (M42L05, Thorlabs) with diameter of 50 μm, exposure time 50 ms, image width 1314 μm; right: square-core MMF (M103L05, Thorlabs) sized 150 μm by 150 μm, exposure time 30 ms, image width 898 μm. Number shows the contrast value in each image. Colorbar denotes grayscale between 0 – 255.

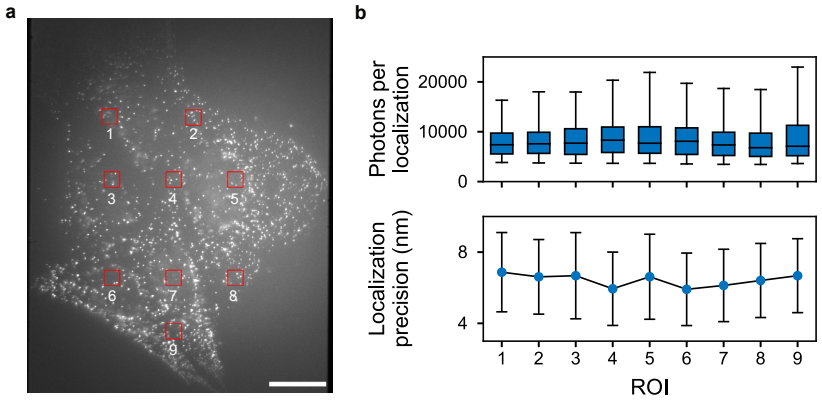


Figure 2.8: **Extra data for evaluation of sample plane illumination homogeneity by dSTORM imaging at 9 different regions of interest (ROIs) (a)** ROIs each sized 5.4 μm by 5.4 μm indicated for Fig.2(b) in the main texts. **(b)** Top: box plot of average photon count per localization; bottom: average localization precision with error bars indicating the standard deviation. 293,043 localizations analyzed.

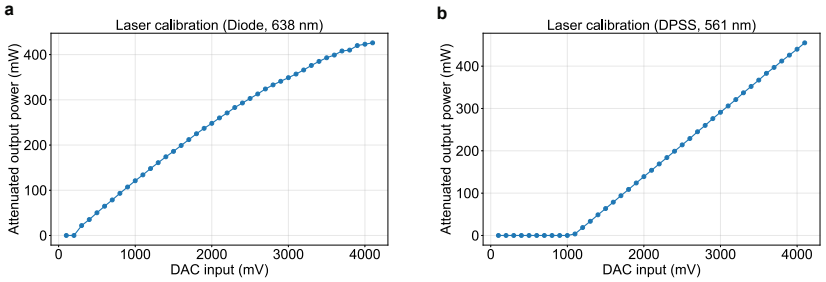


Figure 2.9: **Output power vs. input analog modulation voltage from digital-to-analog converters (DACs) on the laser controller.** (a) Diode laser of 638 nm; (b) DPSS laser of 561 nm. Output power is attenuated for measurement safety and does not reflect the maximum power of the laser combiner.

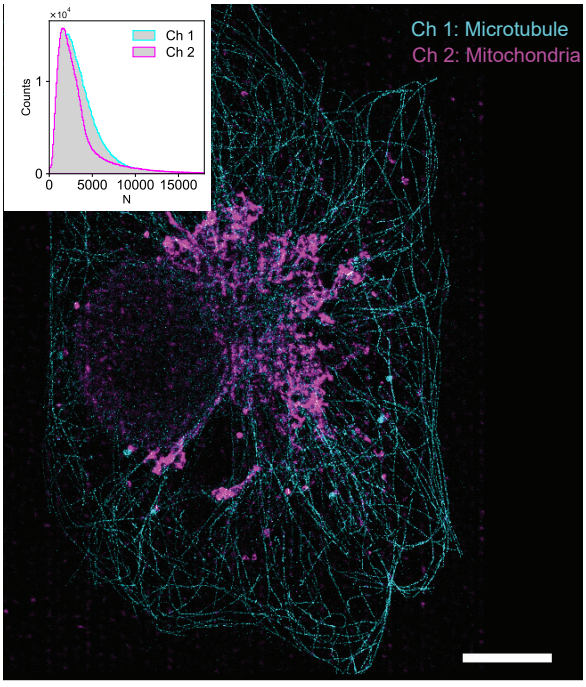


Figure 2.10: **Simultaneous two-color super-resolution imaging by DNA-PAINT** Cyan: microtubules labeled with 5×R1 DNA-PAINT strand and imaged with Cy3B imagers; Magenta: mitochondria labeled with 5×R2 DNA-PAINT strand and imaged with Atto 655 imager. The insert shows the histogram of photons per localization. Scale bar = 10 μm.

Supplementary table

Table 2.2: Summarized information of cell imaging experiments.

Index	Cell type	Labeled structure	Imaging technique	Dye	Laser intensity	Illumination modality	Exposure time	Number of frames
Fig. 2.1**b**	U2OS	Micro-tubules	dSTORM	Alexa Fluor 647	638 nm, 4.67 kW/cm^2	TIRF, small FOV	20 ms	1
Fig. 2.1**c**	U2OS	Micro-tubules	DNA-PAINT	Cy3B	561 nm, 0.39 kW/cm^2	TIRF, large FOV	50 ms	1
Fig. 2.1**d**	COS-7	Micro-tubules	dSTORM (at low intensity)	Alexa Fluor 647	638 nm, 0.05 kW/cm^2	TIRF or epi, large FOV	10 ms	1
Fig. 2.4**a**	COS-7	Micro-tubules	dSTORM	Alexa Fluor 647	638 nm, 1.20 kW/cm^2	TIRF, small FOV	70 ms	10000
Fig. 2.4**b**	COS-7	Micro-tubules	DNA-PAINT	Cy3B	561 nm, 0.39 kW/cm^2	TIRF, large FOV	100 ms	10000
Fig. 2.4**c**	COS-7	Micro-tubules	DNA-PAINT and SOFI	Atto 655	561 nm, 0.59 kW/cm^2	TIRF, large FOV	10 ms	500 per tile
Fig. 2.8	U2OS	Micro-tubules	dSTORM	Alexa Fluor 647	638 nm, 4.67 kW/cm^2	TIRF, small FOV	20 ms	10000
Fig. 2.10	COS-7	Micro-tubules and Mito-chondria	DNA-PAINT	Cy3B and Atto 655	561 nm, 1.17 kW/cm^2 638 nm, 1.74 kW/cm^2	HILO, large FOV	50 ms	10000

References

[1] N. Radmacher, A. I. Chizhik, O. Nevskyi, J. I. Gallea, I. Gregor, J. Enderlein, Molecular Level Super-Resolution Fluorescence Imaging, Annual Review of Biophysics 54, 163–184 (2025). DOI: 10.1146/annurev-biophys-071524-105321.

[2] Y. M. Sigal, R. Zhou, X. Zhuang, Visualizing and discovering cellular structures with super-resolution microscopy, Science 361, 880–887 (2018). DOI: 10.1126/science.aau1044.

[3] M. Lelek, M. T. Gyparaki, G. Beliu, F. Schueder, J. Griffié, S. Manley, R. Jungmann, M. Sauer, M. Lakadamyali, C. Zimmer, Single-molecule localization microscopy, Nature Reviews Methods Primers 1, 39 (2021). DOI: 10.1038/s43586-021-00038-x.

[4] S. Basak, A. Chizhik, J. I. Gallea, I. Gligonov, I. Gregor, O. Nevskyi, N. Radmacher, R. Tsukanov, J. Enderlein, Super-resolution optical fluctuation imaging, Nature Photonics 19, 229–237 (2025). DOI: 10.1038/s41566-024-01571-3.

[5] M. Pawlowska, R. Tenne, B. Ghosh, A. Makowski, R. Lapkiewicz, Embracing the uncertainty: the evolution of SOFI into a diverse family of fluctuation-based super-resolution microscopy methods, Journal of Physics: Photonics 4, 012002 (2021). DOI: 10.1088/2515-7647/ac3838.

[6] T. Dertinger, R. Colyer, G. Iyer, S. Weiss, J. Enderlein, Fast, background-free, 3D super-resolution optical fluctuation imaging (SOFI), Proceedings of the National Academy of Sciences 106, 22287–22292 (2009). DOI: 10.1073/pnas.0907866106.

[7] J. Hohlbein, B. Diederich, B. Marsikova, E. G. Reynaud, S. Holden, W. Jahr, R. Haase, K. Prakash, Open microscopy in the life sciences: quo vadis?, Nature Methods 19, 1020–1025 (2022). DOI: 10.1038/s41592-022-01602-3.

[8] D. Schröder, J. Ries, Cost-efficient open source laser engine for microscopy, Biomedical Optics Express 11, 609–623 (2020). DOI: 10.1364/BOE.380815.

[9] J. Y. Lam, Y. Wu, E. Dimou, Z. Zhang, M. R. Cheetham, M. Körbel, Z. Xia, D. Klenerman, J. S. Danial, An economic, square-shaped flat-field illumination module for TIRF-based super-resolution microscopy, Biophysical Reports 2, None (2022). DOI: 10.1016/j.bpr.2022.100044.

[10] K. Kwakwa, A. Savell, T. Davies, I. Munro, S. Parrinello, M. A. Purbhoo, C. Dunsby, M. A. Neil, P. M. French, easySTORM: a robust, lower-cost approach to localisation and TIRF microscopy, Journal of Biophotonics 9, 948–957 (2016). DOI: 10.1002/jbio.201500324.

[11] K. J. A. Martens, S. P. B. van Beljouw, S. van der Els, J. N. A. Vink, S. Baas, G. A. Vogelaar, S. J. J. Brouns, P. van Baarlen, M. Kleerebezem, J. Hohlbein, Visualisation of dCas9 target search in vivo using an open-microscopy framework, Nature Communications 10, 3552 (2019). DOI: 10.1038/s41467-019-11514-0.

[12] B. Diederich, R. Lachmann, S. Carlstedt, B. Marsikova, H. Wang, X. Uwurukundo, A. S. Mosig, R. Heintzmann, A versatile and customizable low-cost 3D-printed open standard for microscopic imaging, Nature Communications 11, 5979 (2020). DOI: 10.1038/s41467-020-19447-9.

[13] B. Diederich, P. Then, A. Jügler, R. Förster, R. Heintzmann, cellSTORM—Cost-effective super-resolution on a cellphone using dSTORM, PLoS ONE 14, e0209827 (2019). DOI: 10.1371/journal.pone.0209827.

[14] L. Lopez, F. Edorna, F. D. Choque, G. Ferrari, L. A. Masullo, G. Acuna, P. Tinnefeld, A. M. Szalai, P. Zdańkowski, A. Zelcer, F. Stefani, Open-source Sub-Nanometer Stabilization System for Super-resolution Fluorescence Microscopy, Research Square (2025). DOI: 10.21203/rs.3.rs-6131181/v1.

[15] X. Moreno, S. Al-Kadhimi, J. Alvelid, A. Bodén, I. Testa, ImSwitch: Generalizing microscope control in Python, Journal of Open Source Software 6, 3394 (2021). DOI: 10.21105/joss.03394.

[16] C. Niederauer, M. Seynen, J. Zomerdijk, M. Kamp, K. A. Ganzinger, The K2: Open-source simultaneous triple-color TIRF microscope for live-cell and single-molecule imaging, HardwareX 13, e00404 (2023). DOI: 10.1016/j.ohx.2023.e00404.

[17] M. N. Alsamsam, A. Kopūstas, M. Jurevičiūtė, M. Tutkus, The miEye: Bench-top super-resolution microscope with cost-effective equipment, HardwareX 12, e00368 (2022). DOI: 10.1016/j.ohx.2022.e00368.

[18] J. S. H. Danial, J. Y. L. Lam, Y. Wu, M. Woolley, E. Dimou, M. R. Cheetham, D. Emin, D. Klenerman, Constructing a cost-efficient, high-throughput and high-quality single-molecule localization microscope for super-resolution imaging, Nature Protocols 17, 2570–2619 (2022). DOI: 10.1038/s41596-022-00730-6.

[19] R. M. Power, A. Tschanz, T. Zimmermann, J. Ries, Build and operation of a custom 3D, multicolor, single-molecule localization microscope, Nature Protocols 19, 2467–2525 (2024). DOI: 10.1038/s41596-024-00989-x.

[20] K. Bellve, C. Standley, L. Lifshitz, K. Fogarty, Design and Implementation of 3D Focus Stabilization for Fluorescence Microscopy, Biophysical Journal 106, 606a (2014). DOI: 10.1016/j.bpj.2013.11.3354.

[21] H. Pinkard, N. Stuurman, I. E. Ivanov, N. M. Anthony, W. Ouyang, B. Li, B. Yang, M. A. Tsuchida, B. Chhun, G. Zhang, R. Mei, M. Anderson, D. P. Shepherd, I. Hunt-Isaak, R. L. Dunn, W. Jahr, S. Kato, L. A. Royer, J. R. Thiagarajah, K. W. Eliceiri, E. Lundberg, S. B. Mehta, L. Waller, Pycro-Manager: open-source software for customized and reproducible microscope control, Nature Methods 18, 226–228 (2021). DOI: 10.1038/s41592-021-01087-6.

[22] Pymmcore-plus Contributors, pymmcore-plus: Pure python/C++ micro-manager ecosystem (2026).

[23] J. Deschamps, J. Ries, EMU: reconfigurable graphical user interfaces for Micro-Manager, BMC Bioinformatics 21, 456 (2020). DOI: 10.1186/s12859-020-03727-8.

[24] E. Betzig, G. H. Patterson, R. Sougrat, O. W. Lindwasser, S. Olenych, J. S. Bonifacino, M. W. Davidson, J. Lippincott-Schwartz, H. F. Hess, Imaging Intracellular Fluorescent Proteins at Nanometer Resolution, Science 313, 1642–1645 (2006). DOI: 10.1126/science.1127344.

[25] S. T. Hess, T. P. K. Girirajan, M. D. Mason, Ultra-High Resolution Imaging by Fluorescence Photoactivation Localization Microscopy, Biophysical Journal 91, 4258–4272 (2006). DOI: 10.1529/biophysj.106.091116.

[26] M. J. Rust, M. Bates, X. Zhuang, Sub-diffraction-limit imaging by stochastic optical reconstruction microscopy (STORM), Nature Methods 3, 793–795 (2006). DOI: 10.1038/nmeth929.

[27] S. van de Linde, A. Löschberger, T. Klein, M. Heidbreder, S. Wolter, M. Heilemann, M. Sauer, Direct stochastic optical reconstruction microscopy with standard fluorescent probes, Nature Protocols 6, 991–1009 (2011). DOI: 10.1038/nprot.2011.336.

[28] R. Diekmann, M. Kahnwald, A. Schoenit, J. Deschamps, U. Matti, J. Ries, Optimizing imaging speed and excitation intensity for single-molecule localization microscopy, Nature Methods 17, 909–912 (2020). DOI: 10.1038/s41592-020-0918-5.

[29] J. Deschamps, A. Rowald, J. Ries, Efficient homogeneous illumination and optical sectioning for quantitative single-molecule localization microscopy, Optics Express 24, 28080–28090 (2016). DOI: 10.1364/OE.24.028080.

[30] R. Janani, D. Majumder, A. Scrimshire, A. Stone, E. Wakelin, A. H. Jones, N. V. Wheeler, W. Brooks, P. A. Bingham, From acrylates to silicones: A review of common optical fibre coatings used for normal to harsh environments, Progress in Organic Coatings 180, 107557 (2023). DOI: 10.1016/j.porgcoat.2023.107557.

[31] N. Stuurman, Adapter for the Arduino electronics prototyping platform (2026).

[32] A. Jabermoradi, S. Yang, M. I. Gobes, J. P. M. van Duynhoven, J. Hohlbein, Enabling single-molecule localization microscopy in turbid food emulsions, Philosophical Transactions of the Royal Society A: Mathematical, Physical and Engineering Sciences 380, 20200164 (2022). DOI: 10.1098/rsta.2020.0164.

[33] S.-T. Hung, J. Cnossen, D. Fan, M. Siemons, D. Jurriens, K. Grußmayer, O. Soloviev, L. C. Kapitein, C. S. Smith, SOLEIL: single-objective lens inclined light sheet localization microscopy, Biomedical Optics Express 13, 3275–3294 (2022). DOI: 10.1364/BOE.451634.

[34] SmarActGmbH, Super-resolution Kits (2026).

[35] J. Schnitzbauer, M. T. Strauss, T. Schlichthaerle, F. Schueder, R. Jungmann, Super-resolution microscopy with DNA-PAINT, Nature Protocols 12, 1198–1228 (2017). DOI: 10.1038/nprot.2017.024.

[36] S. Strauss, R. Jungmann, Up to 100-fold speedup and multiplexing in optimized DNA-PAINT, Nature methods 17, 789–791 (2020). DOI: 10.1038/s41592-020-0869-x.

[37] R. O'Carroll, J. P. Reynolds, M. Al-Roqi, E. D. Aiyegbusi, D. Dooley, ThermoCyte: an inexpensive open-source temperature control system for in vitro live-cell imaging, Royal Society Open Science 10 (2023). DOI: 10.1098/rsos.231037.

[38] D. Mahecic, W. L. Stepp, C. Zhang, J. Griffié, M. Weigert, S. Manley, Event-driven acquisition for content-enriched microscopy, Nature Methods 19, 1262–1267 (2022). DOI: 10.1038/s41592-022-01589-x.

[39] H. Pinkard, L. Waller, Microscopes are coming for your job, Nature Methods 19, 1175–1176 (2022). DOI: 10.1038/s41592-022-01566-4.

[40] H. Ma, R. Fu, J. Xu, Y. Liu, A simple and cost-effective setup for super-resolution localization microscopy, Scientific Reports 7, 1542 (2017). DOI: 10.1038/s41598-017-01606-6.

[41] K. de Zwaan, **R. Huo**, M. N. Hensgens, H. L. Wienecke, M. Tekpınar, H. Geertsema, K. Grußmayer, High-Throughput Single-Molecule Microscopy with Adaptable Spatial Resolution Using Exchangeable Oligonucleotide Labels, ACS Nano (2025). DOI: 10.1021/acsnano.4c18502.

[42] K. I. Mortensen, L. S. Churchman, J. A. Spudich, H. Flyvbjerg, Optimized localization analysis for single-molecule tracking and super-resolution microscopy, Nature Methods 7, 377–381 (2010). DOI: 10.1038/nmeth.1447.

[43] Y. Wang *et al.*, Localization events-based sample drift correction for localization microscopy with redundant cross-correlation algorithm, Optics Express 22, 15982–15982 (2014). DOI: 10.1364/OE.22.015982.

[44] U. Endesfelder, S. Malkusch, F. Fricke, M. Heilemann, A simple method to estimate the average localization precision of a single-molecule localization microscopy experiment, Histochemistry and Cell Biology 141, 629–638 (2014). DOI: 10.1007/s00418-014-1192-3.

3

High-throughput Single Molecule Microscopy with Adaptable Resolution Using Exchangeable Oligonucleotide Labels

In this chapter, we exploit the high-resolution information hidden in the statistics of fluctuating fluorescence signals manipulable with exchangeable oligonucleotide labels. Combining DNA-PAINT and SOFI reduces the imaging acquisition time, while enabling us to tune spatial and temporal resolutions flexibly according to the application.

A modified version of this chapter has been published: K. de Zwaan* , R. Huo*, M. N. F. Hensgens, H. L. Wienecke, M. Tekpınar, H. Geertsema, and K. Grußmayer, ACS Nano 19, (2025). K. de Zwaan was a master's student supervised by the author. * denotes equal contribution.

3.1. Introduction

Fluorescence microscopy has elucidated important new insights in cellular processes over the past decades. The recent establishment of super-resolution microscopy methods have further pushed the boundaries of fluorescence microscopy to facilitate the visualization of cellular structures, such as nuclear pores and the neuronal cytoskeleton, at resolutions close to the molecular level [1–3].

A particularly promising SMLM method is DNA-PAINT (Point Accumulation for Imaging in Nanoscale Topography) since it can achieve the highest localization accuracy while still posing only modest hardware requirements. DNA-PAINT uses transient hybridization events between fluorophore-coupled single-stranded DNA oligonucleotides (imagers) and target-associated complementary DNA oligonucleotides (docking strands) that can be bound repetitively [4]. The temporary immobilization of imagers yields a distinct fluorescent blink that can be computationally localized with an accuracy of a couple of nanometers. The oligo blinking kinetics are highly programmable by modulating DNA hybridization parameters through sequence design and buffer composition to obtain only a subset of the target-bound oligos to be hybridized to fluorescent imagers, thereby separating single blinking events in space and time [5–11]. Localizations of tens of thousands individual fluorescent blinks then render a super-resolved image. Compared to other SMLM techniques including dSTORM or PALM where photoswitching between on- and off- states are tuned by laser excitation, or chemical reagents, DNA-PAINT blinking events are solely determined by DNA oligo hybridization kinetics and thus uncoupled from fluorophore photophysics allowing for the use of the brightest, photostable organic dyes [11]. DNA-PAINT also facilitates multiplexed imaging of different cellular structures in a single wavelength through use of different imager-binder pairs sequentially, thereby avoiding chromatic aberration [12].

Despite the many advantages of DNA-PAINT, this method is still sparsely deployed, arguably due to its low data throughput. The fluorescent signal of immobilized imagers needs to be segregated from diffusive background fluorescence by utilizing long exposure times of several hundred ms, making DNA-PAINT the slowest super-resolution detection method.

In addition, the cells cannot be visualized at low resolution prior to data acquisition, and because of the sparse fluorescent signal during a DNA-PAINT SMLM experiment, the underlying structure can only be observed after full data reconstruction. Consequently, significant time can be spent on the acquisition of data sets that do not result in informative images. This is a significant problem for expanding this promising visualization technique to advance our understanding of the nanoscopic organization of cellular molecules and is exacerbated in 3D imaging.

Here, we aim to improve the detection speed by combining DNA-PAINT with fluctuation-based imaging using super-resolution optical fluctuation imaging (SOFI) and facilitate high-throughput super-resolution imaging. While both rely on stochastic blinking of single fluorophores, SMLM and SOFI differ in the mechanisms exploiting information below the diffraction limit.

SOFI uses higher-order statistical analysis of time series of blinking molecules (i.e., often a fluctuating signal from several overlapping fluorophores) to reconstruct super-resolution images, and avoids the need to localize individual fluorophores.

Correlations in the blinking signal allow us to perform spatiotemporal cumulant analysis with a moderate amount of frames to construct images with a super-resolution point-spread function raised to the power of the cumulant order n. SOFI is relatively insensitive to background signal, allowing for higher labeling densities, higher blinking on-time ratios, lower signal-to-noise and reduced acquisition times than applicable for DNA-PAINT. Previous work by Glogger et al. showed that SOFI can be combined with exchangeable labels using standard DNA-PAINT to eliminate photobleaching effectively [13]. Building on this, we utilize the programmability of DNA-PAINT kinetics and combine it with advanced SOFI processing to significantly speed up super-resolution imaging.

By tuning DNA-PAINT kinetics complemented with SOFI data processing, we establish super-resolution whole-cell imaging of microtubules and mitochondria with 2nd-order SOFI in 5 seconds (500 frames), and up to 4th-order SOFI in 50 seconds (5000 frames), which is 30-300 times faster compared to SMLM data acquisition. Additionally, our approach allowed us to successfully achieve high-order SOFI up to 6th order, with a resolution of 75 nm. Moreover, we also demonstrate that we can effectively switch between two super-resolution modalities - SOFI and SMLM. As a consequence, high-throughput imaging by SOFI can provide a quick sample overview at improved resolution and deliver the necessary optical sectioning for e.g. identification of rare phenotypes. Subsequent SMLM imaging of selected cells allows the ultimate zoom-in at the highest resolution by leveraging the full resolving power of DNA-PAINT labels.

3.2. High-resolution SOFI with oligonucleotide labels

In this study, we explore the synergistic integration of DNA-PAINT and SOFI to accelerate super resolution imaging. SOFI capitalizes on the fluctuations of fluorescent signals to achieve resolution beyond the diffraction limit [14]. Measuring better blinking statistics will lead to a better SOFI signal, which is critical to exploit higher-order SOFI and thus higher spatial resolution. Therefore, we focus on increasing the frequency of fluorescent fluctuations for SOFI analysis by adapting the binding kinetics of DNA-PAINT probes.

Firstly, we adopted speed optimized docking strand 5xR1 which has repeating motifs on the docking strands, increasing the binding rate of imagers[9]. Secondly, by increasing the imager strand concentration, the probability of hybridization of the DNA oligos is raised (Fig. 3.1a,b). Compared to the initial imager strand concentration (Fig. 3.1a), an increase in signal per frame is observed, indicating more frequent binding upon addition of imager strands. This is confirmed by evaluating the intensity time traces over time (Supplementary Fig. 3.9). Combining the periodic sequence motifs and high imager strand concentration, the off-time is decreased essentially.

However, solely increasing the imager strand concentration has limitations for high-order SOFI reconstructions, as it raises background noise, reducing the SNR and SBR which hinders SOFI signal contrast. Moreover, when the off-time is reduced to the point of continuous occupation of resolvable binding sites, fewer intensity fluctuations are observed, consequently diminishing the SOFI signal. Cevoli et al. performed a parameter optimization for SOFI using a design of experiments approach, where simulated data was used to investigate the parameters influencing the quality of SOFI images [15]. The

analysis indicated that the best SOFI results were achieved when the fluorescent on- and off-times were minimized. Thus, to obtain more intensity fluctuations the on-time should also be minimized.

Prior research has demonstrated the acceleration of DNA dehybridization through the incorporation of ethylene carbonate (EC) [16]. This aprotic solvent increases the solubility of the DNA bases and has been effectively employed to accelerate DNA-PAINT experiments by decreasing the on-time without affecting the off-time [6]. Supplementing the high imager strand concentration buffer with EC leads again to the appearance of single blinks, signifying a notable reduction in on-time (Fig. 3.1c, Fig. 3.6). This observation is confirmed by comparing the intensity time traces over time: upon the addition of EC, single peaks are observed whereas without EC, the intensity fluctuations in the signal are less apparent (Supplementary Fig. 3.9). Further increasing the concentration of EC is eventually hindered likely due to changes in the refractive index of the buffer.

SOFI effectively suppresses background noise and improves optical sectioning; this is already apparent in second-order reconstructions in Fig. 3.2. In contrast, the average image shows prominent out-of-focus background, preventing the clear distinction between adjacent microtubule filaments. Each successive order n in SOFI contributes to resolving finer structural details, providing theoretically an up to n-fold resolution enhancement with subsequent deconvolution [18]. To quantify the SOFI results and confirm the expected resolution increase with successive orders, the spatial resolution is estimated using image decorrelation analysis [17] in Fig. 3.2b and Supplementary Fig. 3.7. The resolution enhancement is in good agreement with theoretical predictions (see Supplementary Fig. 3.7). Specifically, for 6th-order SOFI we achieve a remarkable resolution of approximately 75 nm. As a second metric for resolution, the intensity profile across the microtubule axis is quantified (Fig. 3.2c). These results are consistent with decorrelation analysis, showing an increase in resolution with higher orders. For 6th order, the mean diameter of the microtubule (FWHM) is 70 nm. In addition, we show in Supplementary Fig. 3.5 mitochondrial structures that are also resolved up to 6th-order SOFI with the expected resolution enhancement, demonstrating the versatility of our approach.

Higher-order statistical analysis is challenged by the photophysical properties of the fluorophores used, limiting the usage of most fluorophores. First, the ideal fluorophore for SOFI should be photostable [14, 19]. Photobleaching, a correlated phenomenon, will affect the results and would need to be corrected for in the analysis. DNA-PAINT excels in this regard, as its blinking events are decoupled from the inherent fluorophore photophysics since imager strands are exchangeable and can be continuously replenished from a practically infinite buffer reservoir (see Supplementary Fig. 3.8) [13]. Moreover, calculating higher-order cumulants requires well sampled statistics and homogeneous fluorescence blinking behavior [20]; both is the case for DNA-PAINT labels with fast fluctuations and uniform, programmed oligonucleotide binding-unbinding kinetics. Many fluorophores, however, exhibit inhomogeneous blinking during the measurement time, which limits their utility for analysis beyond 2nd or 3rd-order SOFI and can lead to artifacts [21, 22]. In addition, DNA-PAINT probes enable the use of the brightest organic dyes. Altogether, DNA-PAINT labels tuned towards

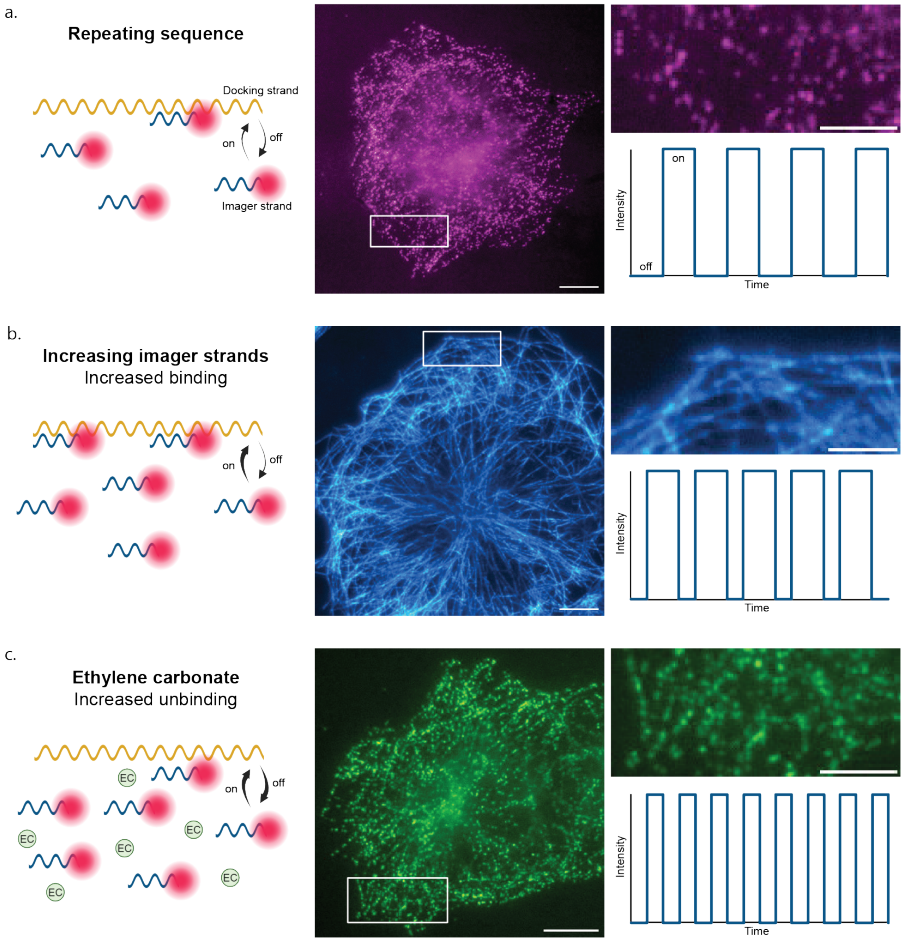


Figure 3.1: **Influence of buffer composition on blinking kinetics. (a)** Raw image frame displaying blinking behavior under low concentration of imager strands of COS7 cells stained for microtubules with repeating docking sequence [9] (scale bar 10 μm). Close up of indicated area (scale bar 5 μm) and representation of corresponding blinking intensity time trace (see Fig. 3.9) **(b)** Blinking behavior with increased imager strand concentration yielding an increased binding frequency. **(c)** Blinking behavior of increased imager strand concentration and addition of ethylene carbonate yielding both an increased binding and unbinding frequency.

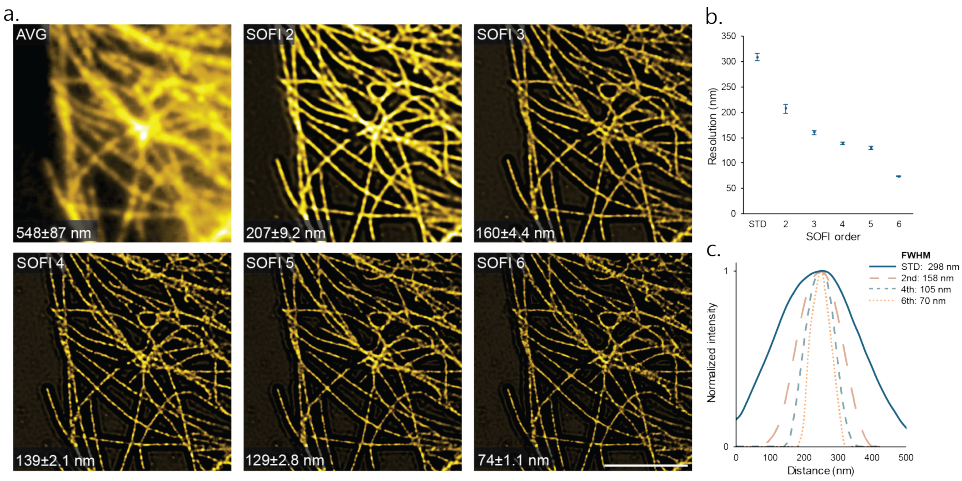


Figure 3.2: **High-order DNA-PAINT SOFI reconstructions** COS7 cells stained for microtubules with repeating docking sequence with resolution increasing for increasing cumulant order. **(a)** Close-ups of diffraction limited average projection of the image sequence, 2nd-, 3rd-, 4th-, 5th- and 6th-order SOFI (scale bar 5 μm). **(b)** Resolution estimate by decorrelation analysis for three different cells for each order (average ± standard deviation) [17]. **(c)** Microtubule cross-section intensity profile for the standard deviation of the image sequence, 2nd-, 4th- and 6th-order SOFI and corresponding FWHM measurements. See Supplementary Table 3.2 for details about the imaging parameters.

high fluctuations are particularly well-suited for high-order SOFI reconstructions due to their exceptional blinking behavior.

3.3. Acquisition time reduction with DNA-PAINT and SOFI

Next, our objective was to enhance the fluctuations to a level that allows us to increase the sampling rate and reduce the number of frames required, all while maintaining high SOFI quality. To achieve this, we optimized our imaging buffer (Supplementary Note 2) by using even higher imager strand concentrations (with the periodic sequence motif docking strand) to decrease the off-time. At the same time, we add the small molecule ethylene carbonate (EC) to reduce the on-time by destabilizing the DNA duplex, leading to more pronounced intensity fluctuations. This approach still provided the blinking statistics required for achieving 6th-order SOFI (Supplementary Fig. 3.5 and Supplementary Fig. 3.6). But more importantly, these optimizations enabled us to measure at a higher frame rate of 100 Hz due to the greater frequency of binding and unbinding events.

As a result, we reduced the acquisition time for 2nd-order SOFI to only 5 seconds

(or 500 frames) and for 4th-order to 50 seconds (or 5000 frames) (Fig. 3.3a,b), which falls within previously reported ranges for other fluorophores [20]. These achievements are validated through a qualitative assessment of structural continuity and absence of artifacts for different acquisition times while the resolution is preserved (Supplementary Fig. 3.10). Additionally, a pixel-wise SNR estimation based on a statistical approach known as jackknife resampling was performed [23] to quantify the SNR of the SOFI images for different acquisition times (Fig. 3.3d).

SMLM DNA-PAINT requires data acquisition at 10 Hz to ensure a sufficient signal-to-background ratio that enables accurate localization. Localization of single emitters was executed and we observed continuity in microtubule filaments after a time series of 30 minutes with a localization precision of 7 nm and a FWHM of 63 nm (Fig. 3.3c, e). In comparison, our DNA-PAINT approach combined with SOFI analysis facilitated a 30-fold reduction in acquisition time for 4th-order SOFI (50 seconds) and a 300-fold reduction for 2nd-order SOFI (5 seconds). The spatial resolution is estimated to be 208 nm for 2nd-order SOFI and 151 nm for 4th-order SOFI, as determined using image decorrelation analysis [17], and 184 nm for 2nd-order SOFI and 140 nm for 4th-order SOFI when evaluating the FWHM (Fig. 3.3e). This highlights that, while SMLM achieves higher spatial super-resolution, it does so at the cost of increasing the acquisition time. Conversely, SOFI improves the acquisition speed (i.e. temporal resolution for dynamic samples) while still surpassing the diffraction limit, albeit with reduced spatial resolution compared to SMLM. So the SOFI optimized buffer allows for rapidly achieved super-resolution marking a significant advancement in imaging speed and highlighting its potential for high-content super-resolution imaging applications.

3.4. High-throughput imaging with adaptive resolution

The drastic improvement in image acquisition time enables high-throughput super-resolution imaging by SOFI directly, making it feasible to capture large areas efficiently (Fig. 3.4a, top panel). To demonstrate, we acquire a 0.65 mm × 0.52 mm area by subsequently scanning partially overlapping FOVs in a 4 × 9 grid (Fig. 3.4b). At each grid position we cover a FOV of 84 μm by 150 μm and image for 500 frames at 10 ms exposure time. The total imaging time is thus 3 minutes plus additional 1 minute of stage movement and data saving time using an automated multi-position imaging protocol. Second-order SOFI reconstructs the microtubule network for the whole stitched FOV at a two-fold resolution enhancement (Fig. 3.4b).

To address the inherent trade-off between spatial and temporal resolution in traditional SMLM DNA-PAINT, we developed a workflow that integrates SOFI followed by SMLM. This approach leverages the fast data acquisition of SOFI to rapidly acquire super-resolution images, which are then used to guide subsequent imaging for SMLM. The sample remains unchanged, with only the buffer conditions modified to achieve the sparse blinking necessary for single-molecule localization (Fig. 3.4a).

We imaged the same field of view with two different buffers (Fig. 3.4c). We start with a SOFI optimized imaging buffer (i.e. high concentration of imager strands and ethylene carbonate) generating frames with a high density of emitters. To reconstruct a 2nd-order SOFI image with 2-fold resolution enhancement (Fig. 3.4d), we need 30 seconds of

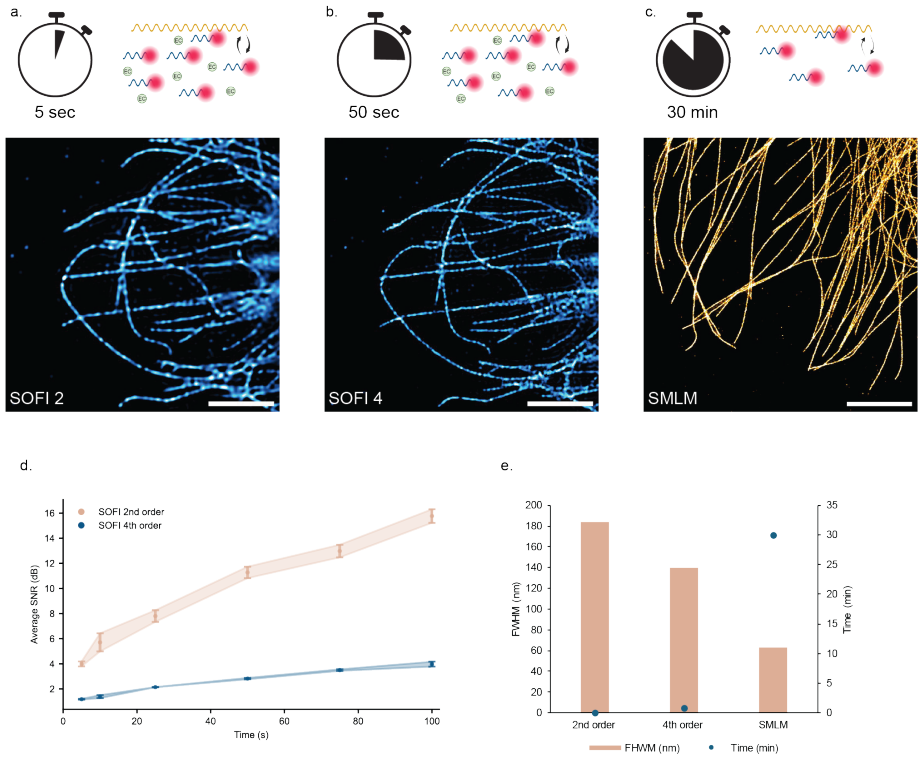


Figure 3.3: **Minimum acquisition time for SMLM and SOFI DNA-PAINT (a, b)** SOFI DNA-PAINT reconstructions of fixed microtubules in COS7 cells labeled with repeating docking sequence obtained with a minimal number of frames and with a frame rate of 100 Hz (scale bar 5 μm, Supplementary Fig. 3.10a,b for qualitative assessment of minimal frame acquisition). **(c)** SMLM DNA-PAINT reconstructions obtained with a minimal number of frames and with a frame rate of 10 Hz (scale bar 5 μm, Supplementary Fig. 3.10c for qualitative assessment of minimal frame acquisition). **(d)** Jackknife SNR metric for 2nd- and 4th-order SOFI as a function of acquisition time. **(e)** Average of 5 FWHM measurements of microtubule crosssections for each reconstruction correlated with the minimum acquisition time. See Supplementary Table 3.2 for details about the imaging parameters.

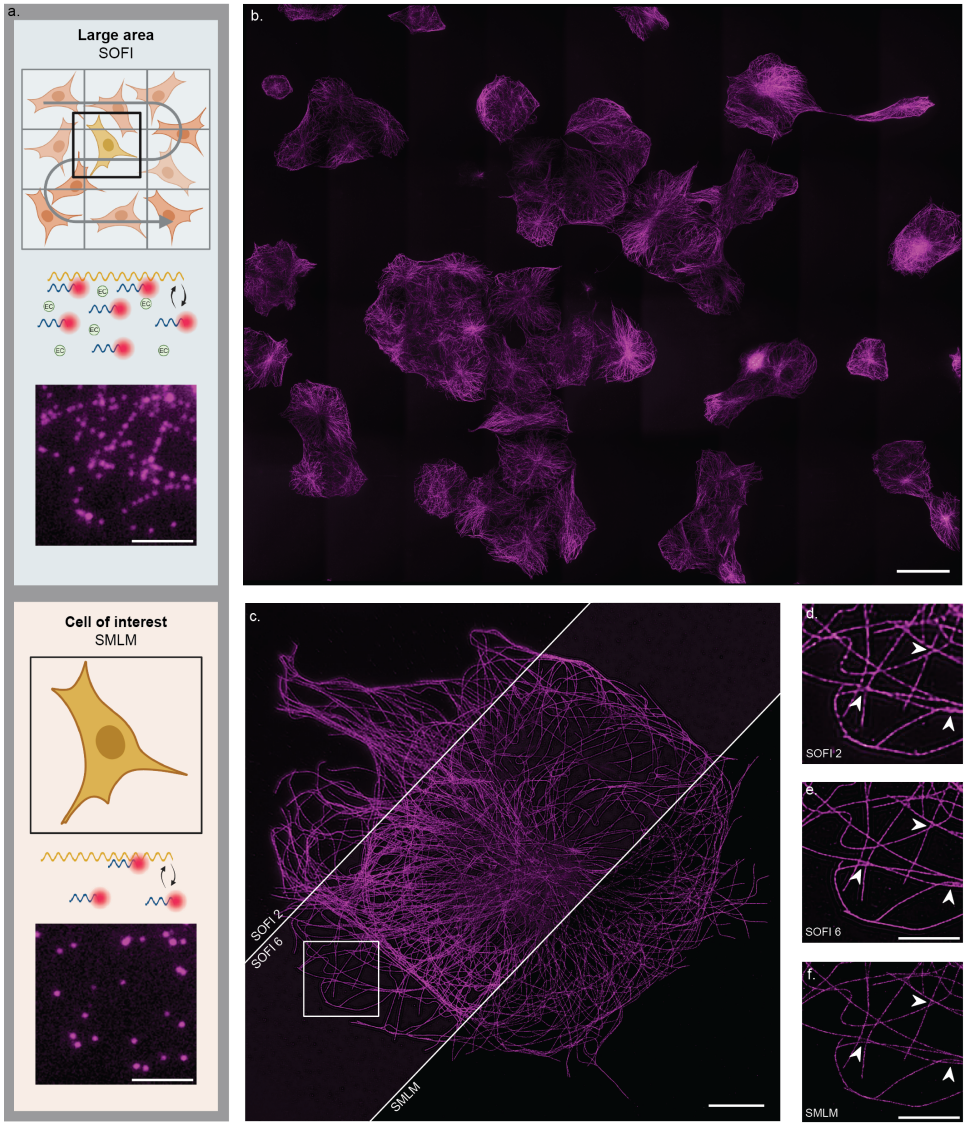


Figure 3.4: **Proof of principle: High-throughput SOFI followed by SMLM. (a)** Schematic of the proposed workflow. *Top:* A large area is imaged using a buffer optimized for fast SOFI. Example of raw data of COS7 cells stained for microtubules for fast SOFI imaging (scale bar: 5 μm). *Bottom:* After washing away buffer components, a low concentration of imager strands is introduced, and a region of interest is imaged using SMLM. Example of raw data of COS7 cells stained for microtubules for SMLM imaging (scale bar: 5 μm). **(b)** High-throughput 2nd-order SOFI imaging of a 0.65 mm × 0.52 mm FOV containing about 40 cells (scale bar 50 μm). **(c)** SOFI and SMLM reconstructions of the same FOV (scale bar 10 μm). **(d, e, f)** Close-ups of corresponding SOFI and SMLM reconstructions as indicated. Arrows indicate areas where improvement of resolution is visible (scale bar 5 μm). See Supplementary Table 3.2 for details about the imaging parameters.

acquisition time per field of view, suitable for rapid screening applications as shown in Figure 3.4a. (Note: The longer acquisition time compared to the results shown in Figure 3.4a was due to our use of a reduced imager strand concentration. This adjustment was necessary to ensure thorough washing away of all imager strands within a reasonable timeframe.) Based on the fast 2nd-order SOFI image, we could then decide whether to continue imaging with the same buffer to achieve higher-order SOFI. By extending the acquisition to a total of 4 minutes, we obtained the blinking statistics necessary for 6th-order SOFI, which provides an expected 6-fold improvement in resolution (Fig. 3.4e).

After these screening steps, if an area of interest or specific event is identified that requires higher spatial resolution, we can transition to SMLM imaging. This involves washing away the initial imager strands and replacing the buffer with one that has a lower concentration of imager strands, which facilitates the sparse blinking allowing localization of single emitters. We acquired SMLM data for a minimum of 25 minutes to reconstruct continuous microtubules with a localization precision of 8 nm (Fig. 3.4f).

We used SQUIRREL to perform a comprehensive analysis of potential artifacts induced by SOFI processing in comparison to traditional SMLM DNA-PAINT processing (see Fig. 3.11) [24]. The resolution-scaled Pearson (RSP) correlation coefficient and the root-mean-square error (RSE) between the reference and resolution-scaled image as a metric for structural discrepancies between the reference and super-resolution images indicate no major differences between SMLM and SOFI. However, we observed that the central part of the cell appears less resolved in SMLM compared to SOFI, suggesting a potential advantage of SOFI in thick cellular regions.

This integrated workflow provides flexible, high-content imaging by combining the speed of SOFI for rapid screening with the high spatial precision of SMLM for more detailed analysis, making it highly adaptable to the specific demands of various experimental contexts. By optimizing the imaging process, this approach is developed for applications requiring both fast screening and high-resolution imaging. For instance, it will be particularly advantageous for screening large numbers of samples or cells to identifying those suitable for downstream analysis or to recognize biologically rare events. Overall, the integration of SOFI and SMLM in our single molecule-based super-resolution workflow significantly improves imaging efficiency without compromising resolution quality.

3.5. Discussion

In summary, our results showed the compatibility of exchangeable labels with two super-resolution techniques, DNA-PAINT and SOFI, and the advantage of significant imaging speed increase when combining them. We also demonstrated spatial resolution tuning in high throughput imaging with our method.

While both rely on the stochastic blinking of single fluorophores, DNA-PAINT and SOFI differ in the mechanism for extracting information below the diffraction limit. SOFI gains resolution enhancement from statistical analysis of detectable fluorescence fluctuations. The quality of SOFI images depends on the effective contrast between on- and off- states, the SNR of acquired images, and the sampling of the blinking kinetics. Homogeneous blinking kinetics are beneficial for SOFI and low photobleaching ensures that the

spatial and temporal correlations analyzed in SOFI arise from stochastic fluorescence fluctuations [20].

In this work, we used the exchangeable oligonucleotide-based probes and first sped up the blinking kinetics for SOFI using repeating sequences on the docking strand, which has been shown to increase the binding events frequency [9]. The highly correlative fluorescence fluctuations resulting from frequent binding and unbinding events at high imager concentrations is crucial for high-order SOFI analysis. We achieved the first successful 6th-order SOFI reconstruction of cellular structures with DNA-PAINT probes. This required the use of post-processing algorithms including deconvolution and brightness linearization, resulting in the improvement of the 6th-order SOFI resolution up to 70 nm. Compared to previous work utilizing exchangeable nucleotide based probes for SOFI [13], this has increased the resolution enhancement by approximately three fold, and is in line with the best resolution reported in imaging continuous cellular structures for SOFI, which is 50–60 nm at 6th-order [20].

Similar to other SMLM techniques, conventional DNA-PAINT suffers from a long acquisition time. Advances in speeding up DNA-PAINT have been focusing on accelerating the blinking kinetics, i.e. shortening both the on- and off- time of blinking fluorophores. However, shorter on- and off- time translate to more fluorophores present in each frame, which poses challenges for SMLM due to the overlapping PSFs in a dense frame that lead to image artifacts. In addition, the localization precision suffers from shorter acquisition times due to a reduced signal-to-background ratio. SOFI eliminates the requirement of sparse distinguishable fluorophores, thereby opening up more blinking kinetics space for imaging speed up. We combined several strategies to increase the blinking frequency. Next to using repeating sequences on the docking strand, we simply increased the imager strand concentration to increase the binding events frequency and to decrease the off-time. We also added ethylene carbonate to the imaging buffer [25], which destabilizes DNA duplex in order to increase the dissociation rate and to decrease the on-time. This resulted in a 2nd-order SOFI image of the microtubule network in cells within only 5 seconds, or 500 frames at 100 Hz. Our data acquisition is 25-fold faster compared to Glogger et al. [13], where the total acquisition time amounts to 125s using the standard P1 and P4 sequences. Obtaining more frames for as long as 50 seconds facilitated the 4th-order SOFI reconstructions in our measurements, 30-fold faster than a typical SMLM acquisition.

Compared to other methods to accelerate DNA-PAINT, for example, argo-PAINT [8] and FLASH-PAINT [26], we avoided adding additional protein or nucleic acids or greatly extending the imager strand length. Our approach could also be combined with other factors in the buffer affecting the nucleic acid binding kinetics, such as salt concentration and temperature [16]. The limitation for our method for more acceleration is mainly the high background signals at higher imager strand concentration that eventually compromises the SNR, even though SOFI intrinsically suppresses the non-correlative background noise. We used TIRF or HILO illumination for our images to provide extra optical sectioning that facilitated the higher-order SOFI. The upper limit of acceleration supported by increased blinking kinetics depends on the structures of interest and the docking strand labeling efficiency. The recent fluorogenic and self-quenched imager strands [7, 27] can further help to reduce background and expand applications in thick

samples. 3D SOFI where different z-positions are imaged at the same time, for example through multiplane splitting [18], can further increase the throughput of the approach.

The optimization of spatial resolution and acquisition time of DNA-PAINT-SOFI not only increases the imaging speed at high resolution and high throughput, but can also function as a useful tool for fast high-content screening of samples at a moderate resolution enhancement. The drastic reduction in acquisition time allowed for a 4-minute imaging with 2-fold resolution enhancement, scanning through a total FOV of 0.65 mm × 0.52 mm . We demonstrated that we can conveniently switch from SOFI conditions to SMLM with localization precision of few nanometers, simply by modifying the buffer composition, i.e. by lowering the imager strand concentration. The resolution improvement between fluctuation-based (about 70 nm) and localization imaging (about 7 nm) in our workflow is akin to switching between confocal and STED imaging, which is routinely done to facilitate data acquisition.

Our 2nd-order SOFI acquisition time for a single position is of a similar scale to structured illumination imaging with DNA-PAINT labels [28, 29] that enables a maximum 2-fold resolution increase. Importantly, our SOFI to SMLM workflow can be carried out using a microscope with simple hardware, facilitating straightforward adoption of our proposed approach. We envision screening a large number of cells with fast SOFI, and to use e.g. machine learning algorithms to interrogate the optically sectioned and background-reduced images to identify rare phenotypes for subsequent interrogation by DNA-PAINT. Since DNA-PAINT relies on stochastically blinking single molecules, identification of full protein structures or networks, and thereby rare events, is generally hampered by time-intensive image acquisition. In fact, the continuous adjustment capability of blinking kinetics with exchangeable oligonucleotide-based probes facilitates tuning of temporal and spatial resolutions to visualize protein structures and networks from a few nanometers with SMLM to dozens with SOFI.

Finally, this approach, which involves controlling blinking dynamics, is not limited to fixed cells alone. Novel PAINT-alike probes compatible with live cells, such as self-labeling protein tags labelled with reversible fluorescent probes [30] offer a promising outlook for high-content live-cell super-resolution imaging. We envisioned our method contributing towards the goal of fast 3D multi-target super-resolution imaging.

3.6. Materials and Methods

Sample preparation

Nanobody production

Bacterial expression plasmids pTP1122 and pTP955 and pDG02583 were a gift from Dirk Görlich (Addgene plasmid #104159; http://n2t.net/addgene:104159; RRID:Addgene_104159, Addgene plasmid #104164; http://n2t.net/addgene:104164; RRID:Addgene_104164, Addgene plasmid #104129; http://n2t.net/addgene:104129; RRID:Addgene_104129, respectively) [31].

The anti-mouse and anti-rabbit nanobodies with protease-cleavable affinity tags and engineered cysteines, and *bd*NEDP1 protease fused to His14-MBP-*bd*SUMO were expressed in *E.coli* BL21(DE3) [31]. 2 liters of Luria Bertani broth (LB broth) was inoculated with 20 mL overnight culture. E.coli were grown to an OD600

between 0.4 and 0.7 before protein expression was induced by 0.5 mM isopropyl B-D-1-thiogalactopyranoside (IPTG). 4 hours after induction, cells were pelleted by centrifugation and resuspended into lysis buffer (50 mM Tris/HCL; pH 8.0, 1 M NaCl, 5mM beta-mercaptoethanol, 50 mM imidazole) and 1mM PMSF was added. Cells were lysed by sonication, and the lysate was cleared by ultracentrifugation for 30 minutes at 4°C (Ti45 rotor, 37,000rpm, Beckman Coulter). The proteins were purified by affinity chromatography using an ÄKTA Start (GE Healthcare ÄKTA Start). The lysate was passed through a 5 mL pre-equilibrated HisTrap HP column (Cytiva) and was washed with lysis buffer. Gradient elution was performed over 10 column volumes (CVs) with filter sterilized elution buffer (50 mM Tris/HCl; pH = 8.0, 150 mM NaCl, 5 mM beta-mercaptoethanol, 500 mM imidazole). The fractions containing nanobody were pooled and a buffer exchange to maleimide labelling buffer (MLB; 100 mM potassium phosphate buffer; pH = 7.5, 150 mM NaCl, 250 mM sucrose) using SnakeSkin dialysis tubing was performed. For the *bd*NEDP1 protease, the eluate was rebuffered to protease buffer (50 mM Tris/HCl; pH = 7.5, 300 mM NaCl, 250 mM sucrose). The protein concentration after buffer exchange was determined using a Nanodrop1000 spectrophotometer (Thermo Fisher Scientific). The nanobodies and protease were aliquoted, frozen in liquid nitrogen, and stored at -80°C until further use.

1 mM His-tag containing nanobodies were cleaved by 0.6 μM bdNEDP1 protease in the thermoshaker at 20°C and 300 RPM for 24 - 96 hours. Cleaved His-tags, His-tag containing proteases and uncleaved nanobodies were purified out of the solution by reverse affinity chromatograpy using an ÄKTA Start (GE Healthcare ÄKTA Start). The cleaved mixture was subjected to purification using a pre-equilibrated 1 mL HisTrap HP column (Cytiva). After loading the sample, the column was washed with MLB to separate and collect the unbound protein (i.e. cleaved nanobodies). Subsequently, gradient elution was conducted over 5 CVs using MLB supplemented with 500 mM imidazole. During elution, the cleaved tags and protease were collected. The purity of the nanobodies was assessed using SDS-PAGE, and the protein concentrations were measured using a Nanodrop1000 spectrophotometer (Thermo Fisher Scientific). Subsequently, the cleaved and purified nanobodies were aliquoted, frozen in liquid nitrogen and stored at -80°C until further use.

Site-specific labeling of nanobodies

A site-specific labeling protocol of the nanobodies with an azide functionalized DNA oligonucleotide was developed based on previous literature and contains a two-step reaction [25, 32]. First, a DBCO-maleimide linker is conjugated to the nanobodies with engineered cysteines. Second, 5'-azide functional oligonucleotide docking strands are conjugated.

Purified and cleaved nanobodies with engineered cysteines were freshly reduced with a 30-fold molar excess of 15 mM TCEP (Carl Roth) for 30 minutes on ice. For a standard reaction, 40 μM reduced nanobody was mixed with 2mM DBCO-maleimide (Jena Bioscience) and incubated for 4 hours at 4°C. Unbound reaction partners were removed in two buffer exchange steps with Phosphate Buffer Saline (PBS; Gibco, ThermoFisher) using a Zeba spin desalting column (10,000 MWCO). The protein concentration and the degree of labeling (DOL) were determined by absorbance at 280 nm for the nanobodies and 309 nm for the DBCO using a Nanodrop1000 spectrophotometer (Thermo Fisher

Scientific).

Docking strand-oligonucleotides (see table 3.1), modified with either a 3' or a 5' azide moiety were synthesized by Biomers.net (Germany) and dissolved in PBS to a concentration of 5mM. For a standard reaction, 10 μM nanobody was incubated with 300 μM azide-docking strand for 30 minutes at 20°C at 300 rpm. Unconjugated docking strands were removed similar to the DBCO conjugation using a Zeba spin desalting column (10,000 MWCO) and protein concentration was determined by measuring the absorbance at 280 nm. The conjugated nanobodies were either stored at 4°C in PBS or -20°C in 50% glycerol.

Table 3.1: Docking site sequences and modifications for nanobody conjugation and corresponding imager strand sequences.

Docking strand (5' - 3')		**Imager strand (3' - 5')**	
P3	azide - TTTCTTCATTA	P3	Atto655 - AGAAGTAATG
5xR1	TCCTCCTCCTCCTCCTCCT - PEG4 - azide	R1	AGGAGGA - Atto655

Cell culture

COS-7 cells (DSMZ GmbH) were cultured in Dulbecco's modified Eagle medium (DMEM) with high glucose (ThermoFisher) supplemented by 10% Fetal Bovine Serum (FBS; Gibco, ThermoFisher), 1% sodium pyruvate (Gibco, ThermoFisher), 1% L-glutamine (Gibco, ThermoFisher), and 1% Penicillin-Streptomycin (Gibco, ThermoFisher). Cells were cultured in a 10-cm culture dish and incubated at 37°C and 5% CO_2. Cells were passed twice a week at 90% confluence, by washing with PBS, incubating with Trypsin/EDTA (Gibco, ThermoFisher) for 3-5 minutes at 37°C, and diluting the cells in fresh medium (1:10) on a new plate.

COS-7 cells were seeded either on 24 mm high-precision cover glasses (Carl Roth) in a 6-well plate or μ-Slide 8 Well high Glass Bottom (Ibidi). The cover glasses were first plasma cleaned by exposure to O_2-plasma for 2 minutes, making the surface hydrophilic allowing better adhesion of cells for microscopy experiments. Cells at 90% confluence were appropriately diluted at a 1:10 ratio and seeded onto the substrates. Following seeding, the cells were incubated at 37°C and 5% CO_2 overnight followed by fixation procedures.

Immunostaining

COS-7 cells were fixed when moderate confluence containing single cells was reached. Generally, this means that the samples were fixed about 24 hours after seeding. Cells were extracted for 90 seconds at room temperature in prewarmed (37°C) extraction buffer containing 0.3% (vol/vol) Triton X-100 and 0.25% (wt/vol) Glutaraldehyde in Microtubule-stabilizing buffer Kapitein (MTSBK; 80 mM PIPES, 7 mM $MgCl_2$, 1 mM egtazic acid, 150 mM NaCl, 5 mM D-glucose). The extraction buffer was replaced by

prewarmed (37°C) fixation buffer (4% (wt/vol) paraformaldehyde in PBS) and incubated for 10 minutes at room temperature. The fixation buffer was removed by washing three times with PBS for five minutes under a small traveling wave in each chamber. After fixation, the cell samples were either stored in PBS with 50% (vol/vol) glycerol at 4°C for up to three days, or the samples were directly quenched.

Fluorescent quenching was performed by incubating 10 mM freshly prepared sodium borohydride in PBS for 7 minutes at room temperature. This was followed by a quick wash with PBS and two washes of 10 minutes on the orbital shaker. The fixed cells were permeabilized with 0.25% (vol/vol) Triton X-100 in PBS, incubated for 7 minutes at room temperature at the orbital shaker and followed by three washes of 5 minutes on the orbital shaker with PBS. Fixed cells were blocked with blocking buffer (BKK; 2% (wt/vol) bovine serum albumin, 10 mM glycine, 50mM NH_4Cl) either for 60 minutes at room temperature or overnight at 4°C.

Primary and secondary antibodies or nanobodies were diluted in BKK according to the desired degree of labeling. Incubation was done for each of the stainings for 1 hour at room temperature in an incubation chamber and followed by three washes with BKK for 5 minutes on the orbital shaker. After the secondary staining and corresponding washes, the samples were post-fixated by incubating for 10-15 minutes with 2% (wt/vol) paraformaldehyde in PBS. Finally, the fixated cells were washed thrice with PBS for 5 minutes on the orbital shaker. Samples were stored in 50% glycerol in PBS at 4°C until used.

Image acquisition

Microscopic images were captured using the setup and software described in Chapter 2. Fixed cells were imaged in an imaging buffer containing 500 mM NaCl in PBS with varying imager strand concentrations at room temperature. In experiments exploring the impact of ethylene carbonate (EC), 5% (v/v) EC (Fisher Scientific) was introduced into the imaging buffer.

Microtubule imaging was conducted utilizing TIRF illumination, while HILO illumination was employed for imaging mitochondria. For each experiment, the selection of exposure time was based on a qualitative assessment of blinking kinetics and the SNR per frame in combination with the resulting SOFI results. The specific imaging parameters for each image can be found in supplementary table 3.2.

For the large FOV imaging, we used the multi-position acquisition in μManager where we generated 4 by 9 grids, with an overlap of 10% between tiles. 500 frames were recorded for one single tile before moving to the next grid. The grids were stitched together later reconstructing a large field-of-view image using the Stitching plugin on Fiji [33].

Data analysis

SOFI cross-cumulant analysis

The SOFI calculations were performed using a cross-cumulant-based algorithm available from `https://www.github.com/kgrussmayer/sofipackage` and implemented in MATLAB R2021b. Constant parameters were chosen allowing for comparison between the imaging buffer conditions. The input image sequence was subdivided into subsequences

of 1000 frames each. This subsequent length was chosen to minimize the influence of photobleaching. If the input was fewer than 1000 frames, the subsequence length was set to match the total length of the imaging series. As a pre-processing step, drift correction based on cross-correlation between the different SOFI subsequences was applied. For post-processing, deconvolution parameters were configured with a PSF approximation of a Gaussian with an FWHM of 4.2 pixels and a total of 10 iterations.

SMLM

The single-molecule localization microscopy (SMLM) reconstruction was conducted using the ThunderSTORM plugin within FIJI. Default settings were applied for image filtering and the approximate localization of molecule parameters. Sub-pixel localization of molecules was achieved utilizing a PFS Integrated Gaussian approach, with a fitting radius set to 4 pixels and an initial sigma of 1.6 pixels, employing a Weighted Least Squares fitting method.

Visualization of the reconstructed data was facilitated through the use of averaged shifted histograms, magnified at 5.0x with an update frequency of 50 frames. Post-localization, drift correction in the xy plane was performed using cross-correlation methods to ensure accurate spatial alignment. Additionally, single-molecule localizations with uncertainty values exceeding 15 were filtered out to enhance data reliability and precision.

Decorrelation analysis

The resolution of the SOFI results was evaluated based on image decorrelation analysis described by Descloux et al. [17]. This algorithm computes spatial resolution within a single image by employing partial phase autocorrelation, which involves the application of a mask filter and the computation of cross-correlation coefficients in Fourier space. To elaborate further, the analysis involves two primary steps. First, a normalized Fourier transform is calculated and subsequently cross-correlated with the original input image in Fourier space using Pearson correlation. Second, this cross-correlation procedure is iteratively executed while the Fourier transform is filtered through a binary circular mask featuring a diminishing radius ranging between 0 and 1.

In this work, the resolution of SOFI results was calculated using the MATLAB software from `https://github.com/Ades91/ImDecorr`. To ensure uniformity throughout the calculations, fixed settings were chosen, taking into account factors such as computational efficiency and precision. The normalized frequencies where the decorrelation curve has to be computed ranges from 0 to 1 with 100 equidistant points within this interval. The number of high-pass filters used to calculate the resolution was set to 20.

Microtubule cross-sections

An alternative approach to assess the resolution is by evaluating the intensity profile of a cross-section of converging microtubules. A perpendicular line profile was defined across a microtubule, and intensity values were recorded and normalized for each experimental condition (including average intensity profile and higher-order SOFI images). This

process necessitated appropriate scaling and considered pixel reduction resulting from SOFI post-processing.

Jackknife SNR

SOFI-specific SNR characterization was performed to ensure sufficient image quality using Jackknife resampling [34]. The algorithm was implemented as part of the SOFI cross-cumulant algorithm and is computationally expensive. Consequently, SNR estimation was conducted solely for specific, carefully chosen acquisitions.

Jackknife resampling involves creating N new datasets, where N corresponds to the number of raw images in the original dataset. Each new dataset is generated by excluding one image from the sequence and is subsequently employed to generate a new SOFI image, resulting in N new SOFI images. For every pixel value $I(x,y)$ in the original SOFI image, N new values $I_n(x,y)$ are produced. These values provide a distribution of possible pixel intensities for that specific pixel location. The variation in these values across the new SOFI images provides insight into the uncertainty associated with the original pixel value. This uncertainty can then be used to calculate the SNR per pixel. The SNR per pixel is defined as:

$$\mathrm{SNR}(x,y) = \frac{I(x,y)}{\sqrt{\mathrm{var}(I(x,y))}} \tag{3.1}$$

Here, the uncertainty associated with the original pixel value is:

$$\mathrm{var}(I(x,y)) = (N-1)\left\langle \left(I_n(x,y) - \left\langle I_n(x,y)\right\rangle\right)^2 \right\rangle \tag{3.2}$$

Intensity time traces

The methodology employed for intensity analysis involved the computation of normalized average pixel intensities over a temporal sequence. This analysis was conducted within a defined region of interest spanning 3x3 pixels across the entire time series. The selection of the specific pixel area involved the identification of a representative microtubule structure within the average widefield projection image. This strategy aimed to ensure that the chosen region was relevant and reflective of the underlying sample characteristics.

Quantitative analysis of imaging artifacts

SQUIRREL was used for quantitative analysis of imaging artifacts for SOFI and SMLM reconstructions. Specifically calculating the resolution-scaled error (RSE) and the resolution-scaled Pearson correlation (RSP) was done using the NanoJ (no GPU) Fiji plugin [24]. The algorithm requires three inputs: a reference image (generally diffraction-limited), a super-resolution image, and a representative resolution scaling function (RSF) image. For the reference images three separate widefield images were generated for SOFI2, SOFI6, and SMLM, using the standard deviation of the frames included in each super-resolution reconstruction. To ensure pixel alignment, both the widefield and SOFI images were cropped as required by the plugin.

Following the method described by Culley et al., the plugin aligned the super-resolution images to the reference widefield image and applied a RSF to match their resolutions [24]. Finally, it calculated the RSP and the RSE between the two images for each input.

3.7. Data Availability

Raw data underlying SOFI and SMLM images are openly available at `https://doi.org/10.4121/bcf01712-4f8d-4f12-bfc6-84fed4ddc086`.

3.8. Appendix

Supplementary table: experiment parameter overview

Figure	**Docking strand Imager strand**	**Buffer composition: [Imager strand], [EC]**	**Frames**	**Exposure time (ms)**	**Illumination intensity (kW cm^{-2})**	**Resolution (nm)**
Figure 3.2, 3.7, 3.8	5xR1 R1-Atto655	100 pM	10,000	30	2.5	74
Figure 3.3a, 3.10a SOFI 2	5xR1 R1-Atto655	20 nM, 5% EC	500	10	2.5	226
Figure 3.3b, 3.10b SOFI 4	5xR1 R1-Atto655	20 nM, 5% EC	5,000	10	2.5	169
Figure 3.3c, 3.10c SMLM	5xR1 R1-Atto655	50 pM	30,000	100	3.1	LP: 7 FWHM: 63
Figure 3.4b SOFI 2	5xR1 R1-Atto655	20 nM, 5% EC	500	10	1.2	230
Figure 3.4, 3.11 SOFI 2	5xR1 R1-Atto655	5 nM, 5% EC	1,000	30	3.1	221
Figure 3.4, 3.11 SOFI 6	5xR1 R1-Atto655	5 nM, 5% EC	8,000	30	3.1	74
Figure 3.4, 3.11 SMLM	5xR1 R1-Atto655	25 pM	15,000	100	3.1	LP: 8 FWHM: 65
Figure 3.1a, 3.9a	5xR1 R1-Atto655	100 pM	10,000	50	2.5	NA
Figure 3.1b, 3.9b	5xR1 R1-Atto655	5 nM	10,000	10	2.5	NA
Figure 3.1c, 3.9c	5xR1 R1-Atto655	5 nM, 5% EC	10,000	30	3.1	NA
Figure 3.5	5xR1 R1-Atto655	5 nM, 5% EC	10,000	50	3.1	73
Figure 3.6	P3 P3-Atto655	10 nM, 5% EC	10,000	30	3.1	115

Table 3.2: Overview of sample types, buffer conditions, imaging parameters, and achieved resolutions. For SOFI images, resolution is assessed through decorrelation analysis, with the resolution of 6th-order SOFI presented unless stated otherwise in the associated figure. For SMLM reconstructions, localization precision (LP) and full width half maximum (FWHM) are provided.

Supplementary figures

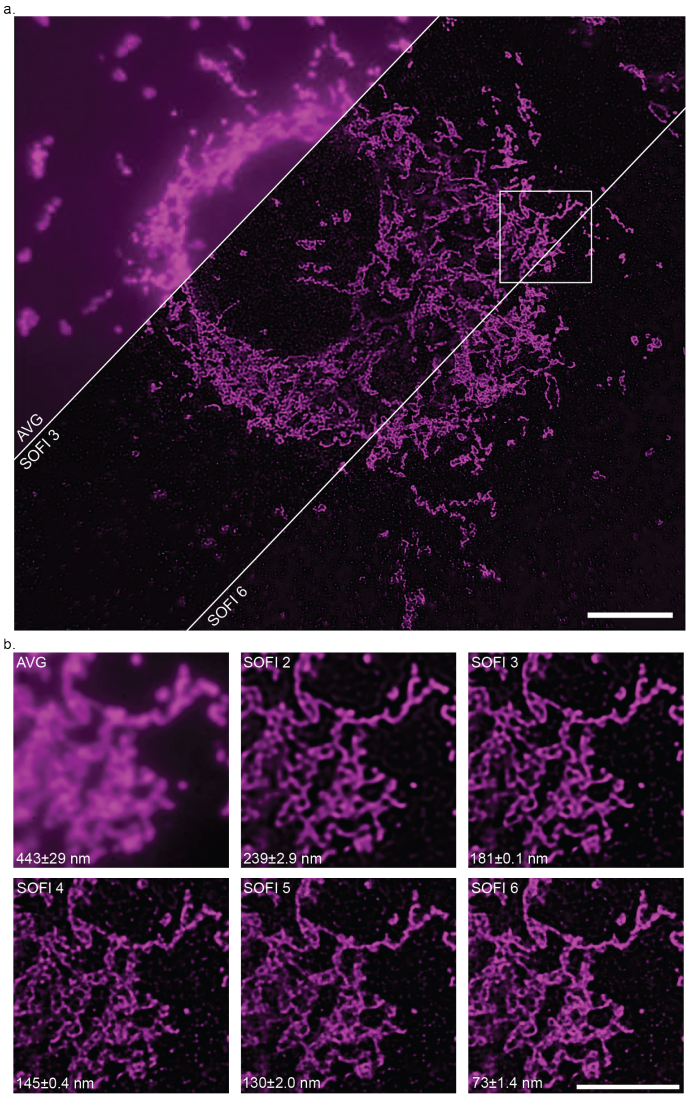


Figure 3.5: **Up till 6th-order SOFI imaging of mitochondria** COS7 cells stained for mitochondria with repeating docking sequence and addition of ethylene carbonate. **(a)** Widefield (average of the image sequence), 3rd- and 6th-order SOFI as indicated (scale bar 10 μm) **(b)** Close-ups of diffraction limited average projection of the image sequence, 2nd-, 3rd-, 4th-, 5th- and 6th-order SOFI as indicated (scale bar 5 μm). See Supplementary Table 3.2 for details about the imaging parameters.

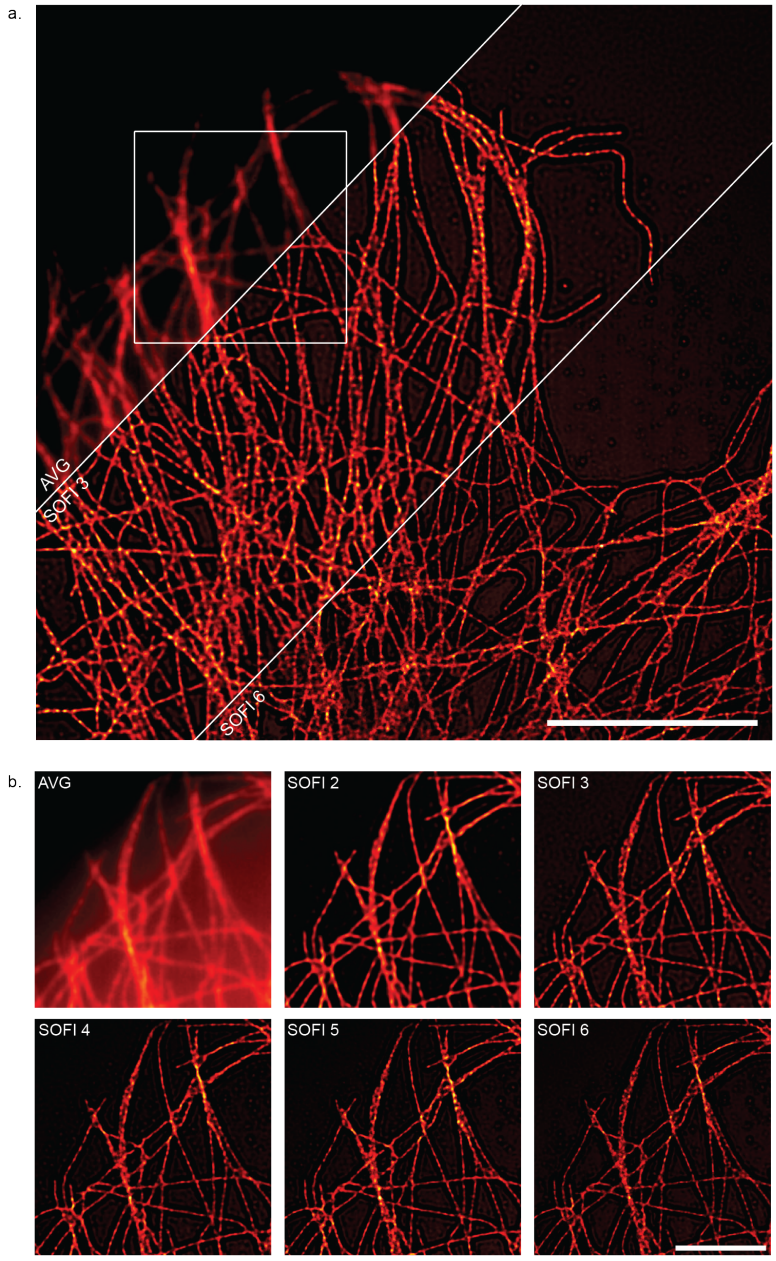


Figure 3.6: **Up till 6th-order SOFI imaging using non-speed optimized docking sequence** COS7 cells stained for mitochondria with non-speed optimized docking sequence (P3) and addition of ethylene carbonate. **(a)** Widefield (average of the image sequence), 3rd- and 6th-order SOFI as indicated (scale bar 10 μm) **(b)** Close-ups of diffraction limited average projection of the image sequence, 2nd-, 3rd-, 4th-, 5th- and 6th-order SOFI as indicated (scale bar 5 μm). See Supplementary Table 3.2 for details about the imaging parameters.

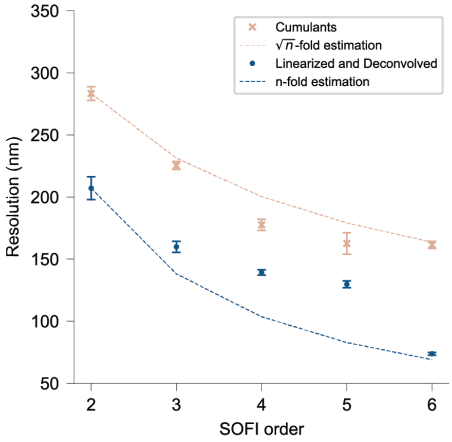


Figure 3.7: **Resolution estimates for three different cells** Resolution estimate using decorrelation analysis of SOFI cumulants (pink, average ± standard deviation) and subsequently linearized and deconvolved SOFI images (blue, average ± standard deviation). The dashed lines connect the theoretical resolution enhancements starting from the 2nd-order SOFI image (pink $\sqrt{n}$- and blue n-fold improvement). See Supplementary Table 3.2 for details about the imaging parameters.

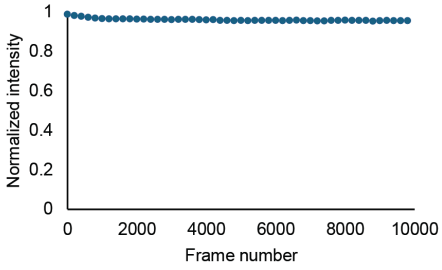


Figure 3.8: **Bleaching resistance of DNA-PAINT for SOFI** Mean fluorescence signal of full time series of three different cells stained for microtubules with DNA-PAINT. See Supplementary Table 3.2 for details about the imaging parameters.

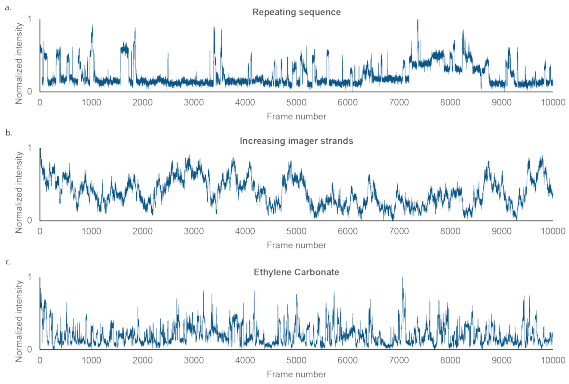


Figure 3.9: **Intensity time traces for varying buffer conditions** Intensity time traces of the signal at a microtubule for varying buffer compositions. **(a)** 100 pM imager strand **(b)** 5 nM imager strand **(c)** 5nM imager strand + 5% ethylene carbonate. Conditions correspond to the examples shown in Fig. 3.1. See Supplementary Table 3.2 for details about the imaging parameters.

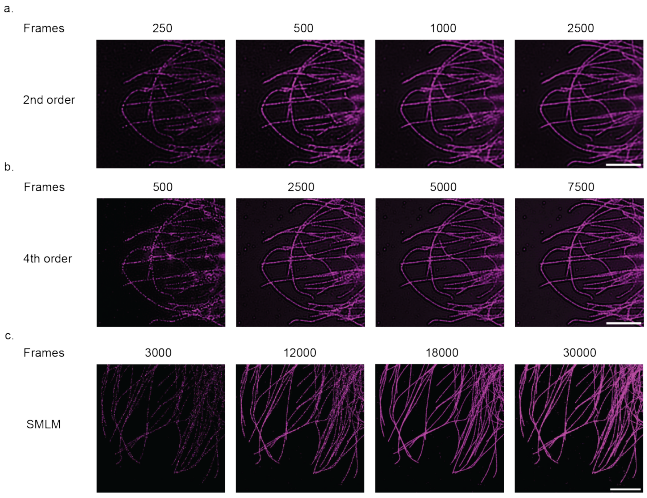


Figure 3.10: **Performance comparison of 2nd- and 4th-order SOFI and SMLM with increasing acquisition time** **(a)** 2nd-order, **(b)** 4th-order SOFI reconstructions and **(c)** SMLM reconstructions using the specified number of frames as input. See Supplementary Table 3.2 for details about the imaging parameters.

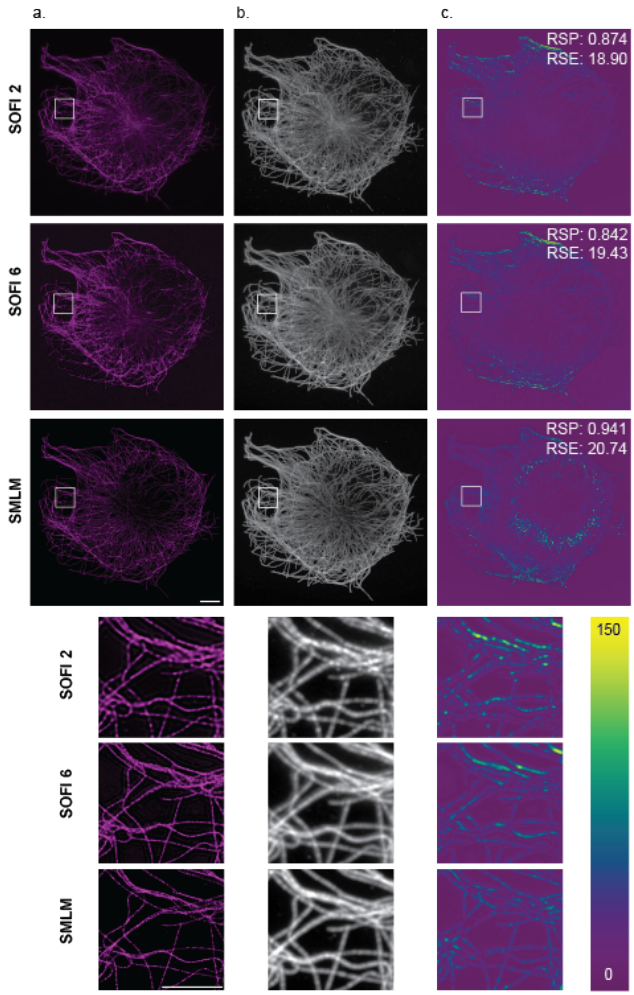


Figure 3.11: **Quantitative analysis of imaging artifacts (a)** Super resolution reconstruction for 2nd-, 6th-order SOFI and SMLM reconstruction as in Figure 3.4 (scale bar 10μm). Close up of indicated region for each reconstruction (scale bar 5μm). **(b)** Corresponding standard deviation widefield image of the frames included in each super-resolution reconstruction **(c)** Quantitative map of errors between the standard deviation widefield image and convolved super-resolution images using the SQUIRREL algorithm [24]. Resolution Scaled Error (RSE) and Resolution Scaled Pearson coefficient (RSP) are denoted. The image processing of SMLM and SOFI among others provides some degree of optical sectioning. This violates the assumption in SQUIRREL that both reference and super-resolution images represent the same focal plane and thus accounts for part of the detected errors. This has been studied in detail for SMLM and SRRF [24, 35]. See Supplementary Table 3.2 for details about the imaging parameters.

References

[1] Y. M. Sigal, R. Zhou, X. Zhuang, Visualizing and discovering cellular structures with super-resolution microscopy, Science 361, 880–887 (2018). DOI: 10.1126/science.aau1044.

[2] K. Xu, G. Zhong, X. Zhuang, Actin, spectrin, and associated proteins form a periodic cytoskeletal structure in axons, Science 339, 452–456 (2013). DOI: 10.1126/SCIENCE.1232251/SUPPL_FILE/1232251.XU.SM.NEW.PDF.

[3] P. Kanchanawong, G. Shtengel, A. M. Pasapera, E. B. Ramko, M. W. Davidson, H. F. Hess, C. M. Waterman, Nanoscale architecture of integrin-based cell adhesions, Nature 2010 468:7323 468, 580–584 (2010). DOI: 10.1038/nature09621.

[4] R. Jungmann, C. Steinhauer, M. Scheible, A. Kuzyk, P. Tinnefeld, F. C. Simmel, Single-molecule kinetics and super-resolution microscopy by fluorescence imaging of transient binding on DNA origami, Nano Letters 10, 4756–4761 (2010). DOI: 10.1021/NL103427W/SUPPL_FILE/NL103427W_SI_001.PDF.

[5] F. Schueder, J. Stein, F. Stehr, A. Auer, B. Sperl, M. T. Strauss, P. Schwille, R. Jungmann, An order of magnitude faster DNA-PAINT imaging by optimized sequence design and buffer conditions, Nature Methods 2019 16:11 16, 1101–1104 (2019). DOI: 10.1038/s41592-019-0584-7.

[6] F. Civitci, J. Shangguan, T. Zheng, K. Tao, M. Rames, J. Kenison, Y. Zhang, L. Wu, C. Phelps, S. Esener, X. Nan, Fast and multiplexed superresolution imaging with DNA-PAINT-ERS, Nature Communications 2020 11:1 11, 1–8 (2020). DOI: 10.1038/s41467-020-18181-6.

[7] K. K. H. Chung, Z. Zhang, P. Kidd, Y. Zhang, N. D. Williams, B. Rollins, Y. Yang, C. Lin, D. Baddeley, J. Bewersdorf, Fluorogenic DNA-PAINT for faster, low-background super-resolution imaging, Nature Methods 19, 554–559 (2022). DOI: 10.1038/s41592-022-01464-9.

[8] M. Filius, T. J. Cui, A. N. Ananth, M. W. Docter, J. W. Hegge, J. van der Oost, C. Joo, High-Speed Super-Resolution Imaging Using Protein-Assisted DNA-PAINT, Nano Lett. 20, 2264–2270 (2020). DOI: 10.1021/acs.nanolett.9b04277.

[9] S. Strauss, R. Jungmann, Up to 100-fold speed-up and multiplexing in optimized DNA-PAINT, Nature Methods 2020 17:8 17, 789–791 (2020). DOI: 10.1038/s41592-020-0869-x.

[10] A. H. Clowsley, W. T. Kaufhold, T. Lutz, A. Meletiou, L. D. Michele, C. Soeller, Repeat DNA-PAINT suppresses background and non-specific signals in optical nanoscopy, Nature Communications 2021 12:1 12, 1–10 (2021). DOI: 10.1038/s41467-020-20686-z.

[11] M. Lelek, M. T. Gyparaki, G. Beliu, F. Schueder, J. Griffié, S. Manley, R. Jungmann, M. Sauer, M. Lakadamyali, C. Zimmer, Single-molecule localization microscopy, Nature Reviews Methods Primers 2021 1:1 1, 1–27 (2021). DOI: 10.1038/s43586-021-00038-x.

[12] R. Jungmann, M. S. Avendaño, J. B. Woehrstein, M. Dai, W. M. Shih, P. Yin, Multiplexed 3D cellular super-resolution imaging with DNA-PAINT and Exchange-PAINT, Nature Methods 2014 11:3 11, 313–318 (2014). DOI: 10.1038/nmeth.2835.

[13] M. Glogger, C. Spahn, J. Enderlein, M. Heilemann, Multi-Color, Bleaching-Resistant Super-Resolution Optical Fluctuation Imaging with Oligonucleotide-Based Exchangeable Fluorophores, Angewandte Chemie - International Edition 60, 6310–6313 (2021). DOI: 10.1002/anie.202013166.

[14] T. Dertinger, R. Colyera, G. Iyer, S. Weiss, J. Enderlein, Fast, background-free, 3D super-resolution optical fluctuation imaging (SOFI), Proceedings of the National Academy of Sciences of the United States of America 106, 22287–22292 (2009). DOI: 10.1073/PNAS.0907866106.

[15] D. Cevoli, R. Vitale, W. Vandenberg, S. Hugelier, R. V. den Eynde, P. Dedecker, C. Ruckebusch, Design of experiments for the optimization of SOFI super-resolution microscopy imaging, Biomed. Opt. Express 12, 2617–2630 (2021). DOI: 10.1364/BOE.421168.

[16] R. Andrews, DNA hybridisation kinetics using single-molecule fluorescence imaging, Essays in Biochemistry 65, 27 (2021). DOI: 10.1042/EBC20200040.

[17] A. Descloux, K. S. Grussmayer, A. Radenovic, Parameter-free image resolution estimation based on decorrelation analysis, Nature Methods 2019 16:9 16, 918–924 (2019). DOI: 10.1038/s41592-019-0515-7.

[18] S. Geissbuehler, A. Sharipov, A. Godinat, N. L. Bocchio, P. A. Sandoz, A. Huss, N. A. Jensen, S. Jakobs, J. Enderlein, F. G. V. D. Goot, E. A. Dubikovskaya, T. Lasser, M. Leutenegger, Live-cell multiplane three-dimensional super-resolution optical fluctuation imaging, Nature Communications 2014 5:1 5, 1–7 (2014). DOI: 10.1038/ncomms6830.

[19] S. Hugelier, W. Vandenberg, T. Lukeš, K. S. Grussmayer, P. H. Eilers, P. Dedecker, C. Ruckebusch, Smoothness correction for better SOFI imaging, Scientific Reports 2021 11:1 11, 1–9 (2021). DOI: 10.1038/s41598-021-87164-4.

[20] K. Grussmayer, T. Lukes, T. Lasser, A. Radenovic, Self-Blinking Dyes Unlock High-Order and Multiplane Super-Resolution Optical Fluctuation Imaging, ACS Nano 14, 9156–9165 (2020). DOI: 10.1021/acsnano.0c04602.

[21] X. Yi, X. Yi, X. Yi, X. Yi, S. Weiss, S. Weiss, S. Weiss, S. Weiss, S. Weiss, Cusp-artifacts in high order superresolution optical fluctuation imaging, Biomedical Optics Express, Vol. 11, Issue 2, pp. 554-570 11, 554–570 (2020). DOI: 10.1364/BOE.382296.

[22] S. Basak, A. Chizhik, J. I. Gallea, I. Gligonov, I. Gregor, O. Nevskyi, N. Radmacher, R. Tsukanov, J. Enderlein, Super-resolution optical fluctuation imaging, Nature Photonics 2025, 1–9 (2025). DOI: 10.1038/s41566-024-01571-3.

[23] P. Dedecker, T. Lasser, S. Duwé, W. Vandenberg, M. Leutenegger, B. Moeyaert, B. Krajnik, Model-free uncertainty estimation in stochastical optical fluctuation imaging (SOFI) leads to a doubled temporal resolution, Biomedical Optics Express, Vol. 7, Issue 2, pp. 467-480 7, 467–480 (2016). DOI: 10.1364/BOE.7.000467.

[24] S. Culley, D. Albrecht, C. Jacobs, P. M. Pereira, C. Leterrier, J. Mercer, R. Henriques, Quantitative mapping and minimization of super-resolution optical imaging artifacts, Nature Methods 2018 15:4 15, 263–266 (2018). DOI: 10.1038/nmeth.4605.

[25] J. Schnitzbauer, M. T. Strauss, T. Schlichthaerle, F. Schueder, R. Jungmann, Super-resolution microscopy with DNA-PAINT, Nature Protocols 12, 1198–1228 (2017). DOI: 10.1038/nprot.2017.024.

[26] F. Schueder, F. Rivera-Molina, M. Su, Z. Marin, P. Kidd, J. E. Rothman, D. Toomre, J. Bewersdorf, Unraveling cellular complexity with transient adapters in highly multiplexed super-resolution imaging, Cell 187, 1769–1784.e18 (2024). DOI: 10.1016/j.cell.2024.02.033.

[27] L. F. Kessler, A. Balakrishnan, N. S. Deußner-Helfmann, Y. Li, M. Mantel, M. Glogger, H.-D. Barth, M. S. Dietz, M. Heilemann, Self-quenched Fluorophore Dimers for DNA-PAINT and STED Microscopy, Angewandte Chemie International Edition 62, e202307538 (2023). DOI: 10.1002/anie.202307538.

[28] F. Schueder, M. T. Strauss, D. Hoerl, J. Schnitzbauer, T. Schlichthaerle, S. Strauss, P. Yin, H. Harz, H. Leonhardt, R. Jungmann, Universal Super-Resolution Multiplexing by DNA Exchange, Angewandte Chemie International Edition 56, 4052–4055 (2017). DOI: https://doi.org/10.1002/anie.201611729.

[29] Y. Wang, J. B. Woehrstein, N. Donoghue, M. Dai, M. S. Avendaño, R. C. J. Schackmann, J. J. Zoeller, S. S. H. Wang, P. W. Tillberg, D. Park, S. W. Lapan, E. S. Boyden, J. S. Brugge, P. S. Kaeser, G. M. Church, S. S. Agasti, R. Jungmann, P. Yin, Rapid Sequential in Situ Multiplexing with DNA Exchange Imaging in Neuronal Cells and Tissues, Nano Letters 17, 6131–6139 (2017). DOI: 10.1021/acs.nanolett.7b02716.

[30] J. Kompa, J. Bruins, M. Glogger, J. Wilhelm, M. S. Frei, M. Tarnawski, E. D'Este, M. Heilemann, J. Hiblot, K. Johnsson, Exchangeable HaloTag Ligands for Super-Resolution Fluorescence Microscopy, J. Am. Chem. Soc. 145, 3075–3083 (2023). DOI: 10.1021/jacs.2c11969.

[31] T. Pleiner, M. Bates, S. Trakhanov, C. T. Lee, J. E. Schliep, H. Chug, M. Böhning, H. Stark, H. Urlaub, D. Görlich, Nanobodies: Site-specific labeling for super-resolution imaging, rapid epitope- mapping and native protein complex isolation, eLife 4 (2015). DOI: 10.7554/ELIFE.11349.

[32] S. Sograte-Idrissi, N. Oleksiievets, S. Isbaner, M. Eggert-Martinez, J. Enderlein, R. Tsukanov, F. Opazo, Nanobody detection of standard fluorescent proteins enables multi-target DNA-PAINT with high resolution and minimal displacement errors, Cells 8 (2019). DOI: 10.3390/cells8010048.

[33] S. Preibisch, S. Saalfeld, P. Tomancak, Globally optimal stitching of tiled 3D microscopic image acquisitions, Bioinformatics 25, 1463–1465 (2009). DOI: 10.1093/bioinformatics/btp184.

[34] H. Deschout, T. Lukes, A. Sharipov, D. Szlag, L. Feletti, W. Vandenberg, P. Dedecker, J. Hofkens, M. Leutenegger, T. Lasser, A. Radenovic, Complementarity of PALM and SOFI for super-resolution live-cell imaging of focal adhesions, Nature Communications 2016 7:1 7, 1–11 (2016). DOI: 10.1038/ncomms13693.

[35] R. F. Laine, H. S. Heil, S. Coelho, J. Nixon-Abell, A. Jimenez, T. Wiesner, D. Martínez, T. Galgani, L. Régnier, A. Stubb, G. Follain, S. Webster, J. Goyette, A. Dauphin, A. Salles, S. Culley, G. Jacquemet, B. Hajj, C. Leterrier, R. Henriques, High-fidelity 3D live-cell nanoscopy through data-driven enhanced super-resolution radial fluctuation, Nature Methods 2023 20:12 20, 1949–1956 (2023). DOI: 10.1038/s41592-023-02057-w.

4

Rapid Sequence Selection by Parallel Kinetic Characterization of DNA Hybridization

Finding oligonucleotide labels with suitable kinetics for single molecule super-resolution imaging is non-trivial task. In this chapter, we propose a new sequence for fast and low-background DNA-PAINT imaging, selected by a novel DNA hybridization characterization technique named SPARXS. SPARXS opens a bright future for high-throughput, kinetics-multiplexed super-resolution imaging with unmatched sequence-selection efficiency.

A modified version of this chapter has been published: C. Bastiaanssen, R. Huo, P. Irmisch, A. Sivaraman, R. Seidel, K. S. Grußmayer, and C. Joo, bioRxiv 10.64898/2026.08.25.746935 (2026).

C. Bastiaanssen and C. Joo developed the SPARXS assay. R. Huo and K.S. Grußmayer conducted the super-resolution imaging. C. Bastiaanssen and R. Huo wrote this Chapter.

4.1. Introduction

Already for decades core biomolecular techniques such as polymerase chain reaction and southern blotting rely on the process of DNA hybridization. In more recent years, creative use of the programmability of DNA hybridization has led to major advances in nanoscale technologies [1]. For instance, DNA origami enables the assembly of custom-shaped nanoscale structures for among others nanophotonics and targeted drug delivery [2]. Beyond structural nanotechnology, DNA hybridization is also exploited in advanced imaging methods. An example is the super-resolution microscopy technique DNA-PAINT (DNA points accumulation for imaging in nanoscale topography) [3]. It makes use of fluorescently labeled short DNA oligonucleotides (imager strands) that transiently hybridize to complementary oligonucleotides which are attached to target molecules. The stochastic hybridization and release of the imager strands is observable as a blinking fluorescence signal which can be used to construct a super-resolution image. Recording multiple hybridization events with sufficient photons is crucial to achieve a high localization precision [4]. Therefore, DNA-PAINT super-resolution imaging requires long acquisition times which makes it slow compared to other super-resolution microscopy techniques. Because both the hybridization rate and the stability of the duplex depend largely on the DNA sequence, one way to accelerate DNA-PAINT imaging is by optimizing the imager sequence [5]. However, while the thermodynamics of DNA hybridization have been well characterized, the kinetics remain more difficult to predict.

Extensive thermodynamic studies have enabled accurate predictions of melting temperatures and free energies [6, 7]. In contrast, the kinetics of DNA hybridization cannot yet be predicted with similar accuracy. In 2017, Hata and colleagues developed a model with a focus on the effect of unstable secondary structures. They achieve a high correlation of 0.92 between the model and the experimental data [8]. However, this is based on a set of 47 oligonucleotide pairs with similar melting temperatures and without any stable secondary structures. It is thus the question how generalizable this model is. More sequences were included in a study by Zhang and colleagues, who measured the hybridization kinetics of 100 36-nucleotide long DNA sequences using a bulk fluorescence assay. They used this data to construct a weighted neighbour voting (WNV) model which achieved an accuracy of a factor 2 for 80% of the predicted hybridization rate constants [9]. Another model of DNA hybridization kinetics was developed by Hertel and colleagues in 2022 [10]. Using surface plasmon resonance, they measured the hybridization rates of 43 DNA sequences ranging in length from 10 to 14 nucleotides. Their model makes use of only two features: the number of nucleating interactions and their sequence-dependent stability. With a Pearson correlation coefficient of approximately 0.7, this minimal model achieves a good correlation with the experimental data, but it is limited to unstructured oligonucleotides. While these models bring us closer to understanding and predicting DNA hybridization kinetics, they cannot yet be used to accurately predict the hybridization kinetics of any DNA sequence.

The lack of models that can accurately predict DNA hybridization kinetics poses a challenge for many DNA-based nanotechnology applications since the kinetics are often essential for choosing the most optimal sequence. Currently, candidate sequences are selected based on features such as thermodynamic stability and secondary structures, after which they are tested in series. For example, one of the fastest sequences up to

date for DNA-PAINT super-resolution imaging has been identified in such a way [5]. However, testing individual sequences in series is costly and time-consuming. To ease the identification of optimal sequences for nanotechnology applications such as DNA-PAINT, we designed a single-molecule parallel DNA hybridization assay. With this assay, we identified a DNA sequence which enables DNA-PAINT super-resolution imaging with an order of magnitude higher sampling rate than the current standard in the DNA-PAINT field (PS3) [5]. Our assay can thus help make more informed sequence selection decisions, instead of potentially missing top performing sequences due to screening only a very limited set of sequences.

4.2. Design of a single-molecule parallel DNA hybridization assay

To measure the kinetics of a library of DNA sequences in parallel, we build on SPARXS (Single-molecule Parallel Analysis for Rapid eXploration of Sequence space), a method that we developed recently [11, 12] (Fig. 4.1). In a SPARXS experiment, a library of DNA sequences is immobilized on the surface of a next-generation sequencing flow cell. To measure DNA hybridization, we added a complementary library in solution. Since the presence of secondary structures and interactions between DNA strands in solution are expected to complicate the analysis and negatively affect the association rate [13], we decided to use a library containing all possible 7-nucleotide combinations of adenine and guanine on the surface (docking library) and of cytosine and tyrosine in solution (imager library). Oligos for the docking library were visualized with a common visualization strand containing a fluorophore (Cy3). As each member of the imager library had to be present at a concentration of 10 nM to generate sufficient hybridization events, the total concentration of the imager library exceeded 1 μM. This library could therefore not be labeled with a regular fluorophore because this would give rise to unsurmountable background signal even when using indirect excitation and total internal reflection fluorescence (TIRF) microscopy. Instead, the imager library was labeled with a dark quencher (BHQ2). The fluorescence signal is thus high when a docking strand is single-stranded, and hybridization of an imager from solution causes a sharp decrease in the signal (Fig. 4.1). After acquiring movies over the entire flow cell surface, the immobilized library is sequenced. Finally, the fluorescence and sequencing datasets are coupled enabling us to analyze the sequence dependence of the hybridization kinetics of the library.

4.3. Parallel kinetic profiling of 128 DNA sequences

A single SPARXS DNA hybridization experiment yielded approximately a million sequence-coupled fluorescence time traces with a coverage of over a thousand traces per library sequence (Supplementary Fig. 4.4). The observed association rates (k_{on}) span a wide range (Fig. 4.2a). For some sequences, only very few events were observed. Therefore, these sequences (with an event frequency below 0.05 Hz) were excluded from further analysis (Supplementary Fig. 4.5). They did however give us information about the minimum free energy change required for us to observe binding. Using NUPACK

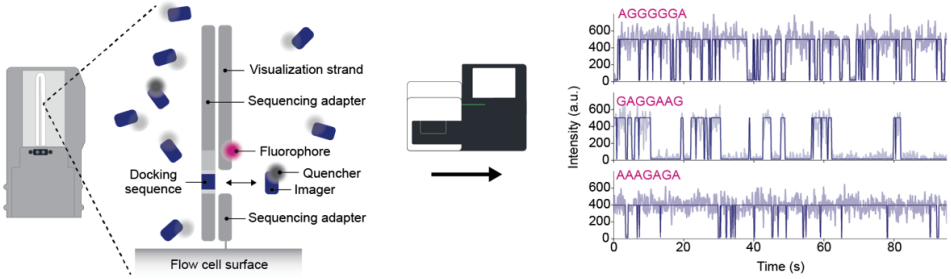


Figure 4.1: **Overview of the SPARXS DNA hybridization assay.** A DNA library of docking sequences is immobilized on the surface of a sequencing flow cell. The library also contains adapters required for sequencing and is prehybridized to a fluorescently labeled visualization strand. A library of dark quencher-labeled imagers is present in solution. After sequencing, sequence-coupled fluorescence time traces (light) are obtained. Representative traces are shown for three different sequences with the hidden Markov model classification in dark. Hybridization events are observed as a sharp decrease in intensity.

[14], we calculated this threshold to be 14.5 K_BT. For each of the other sequences in the docking library, we then calculated how many mismatched imagers had a free energy change above this threshold and would therefore be potential binders. Weak sequences have only a few mismatched binders but strong sequences with many guanines have up to 30 different imagers that can bind (Supplementary Fig. 4.6). Assuming that each of the potential binders for a certain docking sequence has a similar association rate, and that the observed rate is the sum over all these binders, we renormalized the association rate for each docking sequence by dividing the observed rate by the total number of potential binders (Fig. 4.2b). The renormalized association rates scatter around a common value of approximately $5\times\ 10^6$ Ms^{-1} which agrees well with values found in literature [9, 10]. Interestingly, there are differences in association rates between sequences within the same free energy regime. Our SPARXS DNA hybridization experiment thus enables the selection of fast binders beyond predictable sequence dependencies. We further validated our approach by comparing the association rates of all mirror sequences (i.e. pairs of sequences where the 5'-3' direction of one sequence equals the 3'-5' direction of the other) in the library. There is a strong correlation for the observed association rates (Pearson correlation of 0.85, Supplementary Fig. 4.7).

4.4. Super-resolution imaging with an order of magnitude higher sampling rate

From our SPARXS DNA hybridization dataset, we identified a sequence (AG4) that has the potential to outperform the current standard in the DNA-PAINT field (PS3)

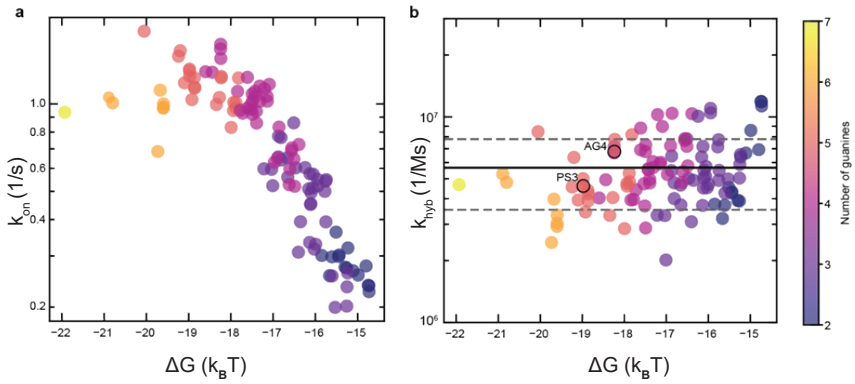


Figure 4.2: **Kinetic characterization of a DNA library using SPARXS. (a)** Scatter plot of the observed association rates. The color of the data points indicates the number of guanosines in the docking sequence. Sequences with an event frequency smaller than 0.05 Hz were excluded. **(b)** Scatter plot of the renormalized association rates with the mean and one standard deviation indicated by the solid and dashed lines respectively.

[5]. The SPARXS data suggest that AG4 has a higher association rate than PS3 (Fig. 4.2b). This enhanced association rate may facilitate a higher sampling rate, thereby enabling higher-resolution DNA-PAINT imaging. To first verify the applicability of AG4 for super-resolution imaging using DNA-PAINT, we used it to image microtubules in cells (Fig. 4.3a). We imaged a complete cell with AG4 using only 200 pM of imager and a camera exposure time of 50 ms. Under these optimized conditions, we achieved a localization precision estimate of 7.82 nm. This is a 17% improvement over the precision we obtained using the classical P1 DNA-PAINT sequence at 1 nM with double the camera exposure time (Supplementary Fig. 4.8).

Next, we compared the performance of AG4 with that of the speed-optimized sequence PS3 and found that AG4 exhibits an approximately 10-fold higher sampling rate than PS3 when reconstructing microtubule filaments (Fig. 4.3b). At a low imager concentration of 100 pM, AG4 exhibits blinking kinetics comparable to those of PS3 at 1 nM. When increasing the AG4 imager concentration to 250 pM, the density of emitters in each frame drastically increased, as is also demonstrated by the increased number of localizations identifiable per frame per unit area in areas of similar filament density (Fig. 4.3c). The lower imager concentration required for AG4 to achieve the sparse blinking conditions necessary for SMLM indicates its potential for DNA-PAINT imaging with reduced background noise and thus improved localization precision.

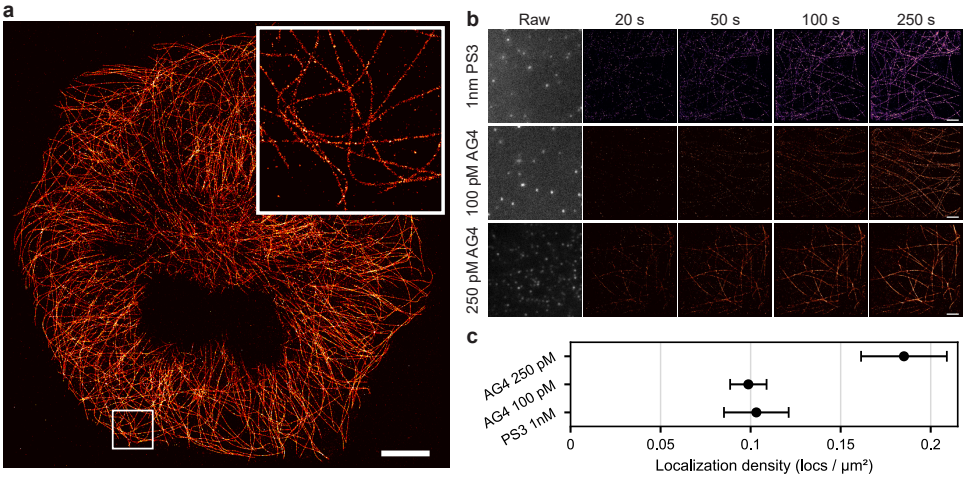


Figure 4.3: **Cellular DNA-PAINT super-resolution imaging with a novel fast-sampling sequence identified by SPARXS. (a)** Whole-cell SMLM reconstruction of microtubules imaged with 200 pM AG4. A localization precision estimation of 7.82 nm was achieved. The insert shows a zoom-in of the highlighted area and the scale bar equals 10 μm.**(b)** DNA-PAINT imaging of microtubules with the sequence as indicated on the left. From left to right: one raw image frame showing emitters in the fluorescence on-state, SMLM reconstruction after 20, 50, 10, and 250 seconds of image acquisition. Scale bars equal 2 μm. **(c)** Comparison of average localization density per frame between 1 nM PS3, 100 pM AG4 and 250 pM AG4. The error bars indicate standard deviation.

4.5. Discussion

The SPARXS DNA hybridization assay presented here provides a powerful and quantitative approach to systematically measure the hybridization kinetics of a library of DNA sequences in parallel. In a single experiment, we screen 128 DNA sequences and identify AG4, a sequence that outperforms PS3, the current DNA-PAINT standard. With AG4, super-resolution images can be obtained at a tenfold higher sampling rate compared to PS3, enabling the use of lower imager concentrations without sacrificing acquisition speed. This improvement directly translates to higher localization precision and lower background noise in the reconstructed super-resolution images. The systematic kinetic screening enabled by our SPARXS DNA hybridization assay thus provides the means to uncover sequence variants with improved performance.

Beyond its advantages for DNA-PAINT, the rapid blinking kinetics and improved signal-to-noise ratio observed with AG4 open new possibilities for other techniques that rely on transient hybridization events. In particular, super-resolution optical fluctuation imaging (SOFI) could benefit from a sequence with these characteristics. SOFI uses higher-order statistical analysis of temporal intensity fluctuations to extract sub-diffraction spatial information [15, 16] and therefore depends critically on measuring sufficient blinking statistics. Due to its enhanced blinking kinetics, AG4 could thus boost super-resolution reconstruction by SOFI. More generally, our SPARXS DNA hybridization assay could be used to select sequences with distinct hybridization kinetics for kinetic multiplexing [17].

Besides for super-resolution imaging techniques, we also expect our SPARXS DNA hybridization assay to accelerate sequence selection for other applications such as dynamic DNA origami structures and DNA walkers [18]. Additionally, the assay can be used to study the effect of mismatches on DNA hybridization kinetics to aid the improvement of the models that describe this essential molecular process. However, a limitation of the assay in its current state is that the mix of imager sequences in solution gives rise to a too complex distribution of bound dwell times to reliably estimate the dissociation rate for each sequence. Further analysis of the current dataset might yield an approach to extract the dissociation rates from the mixture, but another way to more cleanly obtain these rates is to use a library of orthogonal imager sequences [19].

By enabling, high-throughput, quantitative characterization of short DNA hybridization kinetics, our SPARXS DNA hybridization assay provides a powerful tool for the rapid selection of suitable sequences for dynamic DNA-based technologies.

4.6. Methods and Materials

SPARXS library preparation

Synthetic DNA was purchased from Ella Biotech (Germany) (Table S1). The visualization strand was labeled with Cy3 Mono NHS ester (Sigma-Aldrich). For the labeling reaction, 5 μl of 200 μM DNA, 1 μl of freshly prepared 0.5 M sodium bicarbonate and 1 μl of 20 mM dye in DMSO were mixed and incubated for 6 hours at room temperature in the dark. Ethanol precipitation was performed and the labeling efficiency was determined using a spectrophotometer (DeNovix DS-11+). The labeling efficiency was approximately 100%. The final samples were obtained by hybridizing the docking and visualization strand,

with an additional immobilization strand for the control experiments. Hybridization occurred in a 1:1:1 ratio in annealing buffer (10 mM Tris pH 8, 1 mM EDTA, 50 mM NaCl) by heating to 90 °C for 3 min and then slowly cooling with 1 °C every min to 4 °C.

Flow cell preparation

The sequencing flow cell was prepared as described previously [11, 12]. In short, an Illumina MiSeq flow cell is washed, closed with tape, and bleached for 5 h with a blue LED. For the first replicate a v3 Nano MiSeq flow cell was used and for the second replicate a v2 Nano MiSeq flow cell was used.

For control experiments on custom made flow cells, quartz slides with a polyethylene glycol-passivated surface were prepared as described previously [20]. Each channel was incubated with 20 μl 0.1 mg/ml streptavidin (Sigma-Aldrich) for 30 s and unbound streptavidin was flushed out with 100 μl T50 (10 mM Tris-HCl pH 8.0, 50 mM NaCl). Next, 50 μl 50 pM nucleic acid sample was introduced into the chamber and incubated for 1 min, after which unbound sample was flushed out with 100 μl T50. Next, 100 μl imaging buffer (50 mM Tris-HCl pH 8.0, 500 mM NaCl, 1 mM Trolox (6-Hydroxy-2,5,7,8-tetramethylchroman-2-carboxylic acid, Sigma-Aldrich), 2.5 mM PCA (Sigma-Aldrich) and 0.155 U/μl PCD (OYC) was added.

Experimental set-up and data acquisition for SPARXS Single-molecule imaging of the SPARXS experiments was performed on an objective-type total internal reflection fluorescence (TIRF) microscope (Nikon Eclipse Ti2). The microscope was equipped with a 100x oil immersion objective (Nikon CFI Apochromat TIRF 577 100XC Oil) through which the sample was excited and imaged. Excitation occurred in a 360-degree fashion with a 561 nm laser (Gataca iLaunch system, Gattaca iLas2). The collected signal was filtered with two filters (FF01-609/54 and FF01-600/52, Semrock), both being held in a splitting module which was used in bypass mode (OptoSplit 2). Finally, the signal was projected on a CCD camera (Andor iXon Ultra 897). The microscope was equipped with an automated stage and automated focusing system, enabling automated image acquisition using the MetaMorph software.

Experimental set-up and data acquisition for serial DNA hybridization measurements

Control experiments on quartz were performed on a custom-built prism-type TIRF microscope (Nikon Eclipse Ti2). For excitation, a 550 mW 532 nm laser was used (L4Cc-CSB-1311, Oxxius). A 60x water immersion objective (CFI Plan Apochromat VC 60x WI, Nikon) was used to collect the emission signal, which was subsequently filtered using a quad-notch filter in the turret (NF03-405/488/532/635E-25, Semrock). In an external emission box, the signal was split into two channels using a dichroic mirror (T635lpxr, Chroma) and further filtered with emission filters (ET585/65m for the Cy3 and ET655LP for the Cy5 emission signal, Chroma) before being projected onto a CMOS camera (Prime BSI sCMOS, Photometrics) using a dichroic mirror (T635lpxr, Chroma). Movies were acquired using NIS-Elements software (AR 5.20.01) and the microscope was equipped with an automated stage and automated focusing system for automated image acquisition.

Sequencing

Sequencing was performed as described previously, with a manual first strand synthesis step and then sequencing with an altered sequencing recipe using a MiSeq sequencer (Illumina) [11, 12]. The runs were single read with 40 cycles.

Extraction of observed dwell times

Observed dwell times were extracted using the python package Papylio (https://github.com/Chirlmin-Joo-lab/papylio). First, a spatial background correction was applied using a 20-pixel median filter on the 20-frame averaged image. From the corrected averaged image, molecules were localized by finding the local maxima, discarding molecules close to the edge of the image and molecules which could not be fit with a 2D-Gaussian. Next, traces were extracted for each molecule using a Gaussian mask.

For the SPARXS experiments, sequence identification and coupling of the single-molecule and sequencing data were also performed with Papylio. Only molecules with a five-frame rolling average intensity below a set threshold, the expected maximum intensity of a single molecule, were kept. Traces were then fit with a two-state hidden Markov model, or when no binding events were detected with a one-state Gaussian distribution. The low intensity state was classified as bound and the high intensity state was classified as unbound. Unbound dwell times (τ_{unbound}) were determined from the classified traces, discarding events interrupted by the start or end of the movie, and by fitting the distribution with a single-exponential decay.

Thermodynamic and kinetic analysis

All kinetic modeling was performed using custom-written Python (version 3.12) scripts. Thermodynamic parameters for DNA duplex formation were calculated using the NUPACK Python (v4.0.2.0) with reaction conditions set to 25 °C, 0.5 M Na^+, 0 M Mg^{2+} and a strand concentration of 10 nM. For each sequences, its Watson–Crick reverse complement $\bar{s}$ was generated, and the duplex formation reaction was evaluated via partition function calculations, yielding the free energy change upon hybridization $\Delta G(s_j, \bar{s}_i)$.

Off-target binding was quantified by evaluating each sequence's reverse complement against all library sequences. The number of binding-competent strands was determined as:

$$N(s_i) = \sum_j \Theta\big(\Delta G(s_j, \bar{s}_i) - \Delta G_{\text{thresh}}\big) \tag{4.1}$$

with $\Delta G_{\text{thresh}} = -14.5\ k_B T$, chosen to define sequences that are thermodynamically stable within the time resolution, and Θ being the Heaviside function.

The apparent association rate was computed from τ_{unbound} using:

$$k_{\text{on}} = \frac{1}{\tau_{\text{unbound}}} \tag{4.2}$$

Assuming independent parallel binding pathways, the intrinsic bimolecular hybridization rate constant was obtained according to:

$$k_{\text{hyb}} = \frac{k_{\text{on}}}{Nc} \tag{4.3}$$

with c=10 nM being the imager strand concentration.

Cell culture

COS-7 cells (DSMZ GmbH) were cultured in Dulbecco's modified Eagle medium (DMEM) in high glucose (Thermo Fisher) with addition of 10% fetal bovine serum (FBS; Gibco, Thermo Fisher), 1% L-glutamine (Gibco, Thermo Fisher), 1% sodium pyruvate (Gibco, Thermo Fisher), and 1% penicillin-streptomycin (Gibco, Thermo Fisher). On the day before immunostaining, cells were seeded on coverslips (#1.5 type 25 mm diameter, Carl Roth) in 6-well plates in the culture medium and incubated at 37 °C with 5% CO_2.

Microtubule immunostaining

24 hours after seeding cells, α-tubulin on microtubules were immunostained with DNA-PAINT probes. Firstly, extraction buffer based on the Kapitein microtubule buffer (80 mM PIPES, 7 mM $MgCl_2$, 1 mM EGTA, 150 mM NaCl, 5 mM D-glucose) supplemented with 0.3% (v/v) Triton X-100 and 0.25% (w/v) glutaraldehyde was pre-warmed at 37 °C and applied to the cells for 90 seconds at room temperature. Following removal of the extraction buffer, cells were fixed for 10 minutes at room temperature with a fixation buffer containing 4% (w/v) paraformaldehyde in PBS, then washed three times for 5 minutes each with PBS. To reduce autofluorescence, cells were treated for 7 minutes with freshly dissolved 10 mM sodium borohydride in PBS and immediately rinsed with PBS afterwards before two more 10-minute washes on an orbital shaker. The fixed cells were then permeabilized with 0.25% (v/v) Triton X-100 in PBS for 7 minutes and subsequently washed three times for 5 minutes each with PBS. Later, the cells were incubated for one hour at room temperature with blocking buffer containing 2% (w/v) bovine serum albumin, 10 mM glycine, and 50 mM ammonium chloride (NH_4Cl).

Primary antibody (mouse anti-α-tubulin, T5168-.2ML, Merck) was diluted 200 times in the blocking buffer and then added to the cells for one hour at room temperature followed by three washes with the same buffer. Secondary anti-mouse nanobodies were produced and conjugated with DNA docking strand PS3 (Biomers) in house. Nanobody production and site-specific nanobody-DNA conjugation via DBCO-azide click chemistry were described in detail in [21] and Chapter 3. Docking strand AG4 conjugated with secondary anti-mouse sdAbs were custom-made (Massive Photonics). Docking strand P1 conjugated with anti-mouse sdAbs were purchased (Massive Photonics). All secondary nanobodies or antibodies were diluted with the blocking buffer (AG4 at 0.08uM, PS3 at 0.04 μM, and P1 at 0.1 μM) and applied on cells on respective coverslips during one-hour incubation, followed by three 5-minute washes with the blocking buffer.

Cells were post-fixated with 2% PFA after immunostaining and stored in PBS at 4 degrees. During imaging, coverslips were mounted with imaging buffer containing corresponding imager strands diluted at various concentrations in 500 mM NaCl solution in PBS. An overview of the DNA sequences, concentrations and imaging parameters can be found in Table 4.2.

Microscopy setup for cell experiments

All cell images were taken using the microscope and software described in Chapter 2.

DNA-PAINT image analysis

Image stacks were acquired using μManager 2.0 software. DNA-PAINT images were reconstructed using Picasso software (v0.9.5) [22]. Drift correction was done using the redundant cross-correlation (RCC) algorithm [23] integrated in Picasso. The localization precision was estimated by Picasso's integrated nearest neighbor based analysis (NeNA) algorithm [24]. To analyze localization density, five circular regions of interest (ROIs) with a diameter of 5.4 μm covering similar filament density were selected per DNA-PAINT image. The average number of localizations per image frame was extracted from every ROI and plotted using Python.

4.7. Data Availability

Raw data underlying SPARXS and the super-resolution images is publicly available at `https://doi.org/10.4121/697938bb-b2c6-4762-a81f-0270ce9f865f.v1`.

4.8. Appendix

Supplementary figures

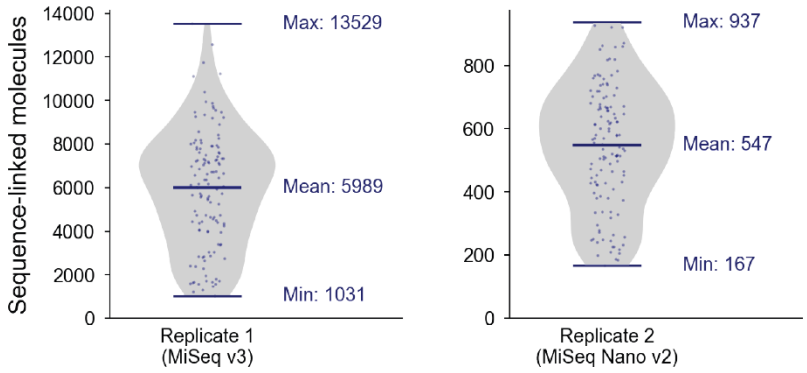


Figure 4.4: **Violin plots of sequence-linked molecules for each SPARXS replicate.** Replicate 1 and 2 were performed using a v3 and v2 Nano MiSeq sequencing flow cell, respectively.

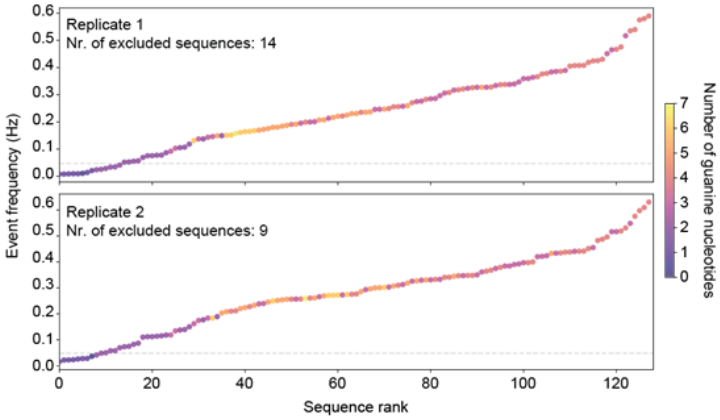


Figure 4.5: **Sequences ranked by event frequency.** Sequences with an event frequency below 0.05 Hz (the dashed line) were excluded from further analysis. The color of the data points indicates the number of guanine nucleotides in the docking sequence. Replicate 1 and 2 were performed using a v3 and v2 Nano MiSeq sequencing flow cell, respectively.

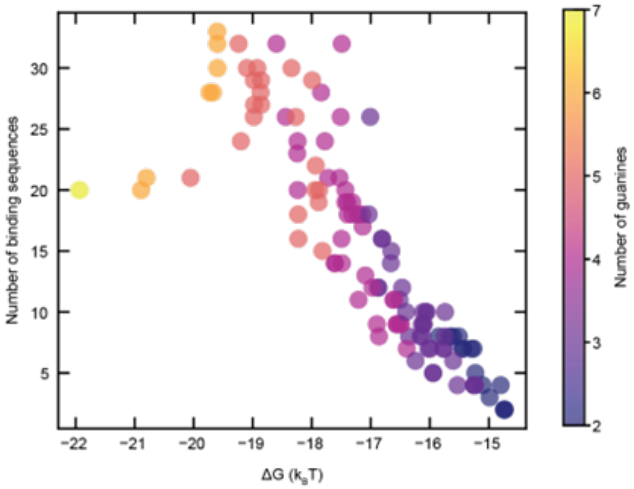


Figure 4.6: **Number of imager sequences that can bind each docking sequence.** The free energy change of all imager sequences was calculated for each docking sequence. Imager sequences were counted as potential binding sequences when the free energy change was below 14.5 k_BT. The color of the data points indicates the number of guanine nucleotides in the docking sequence.

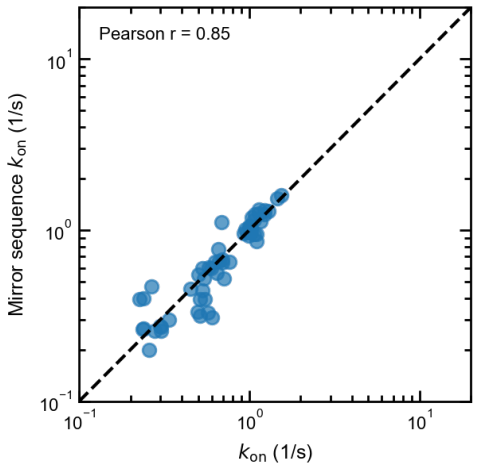


Figure 4.7: **Correlation of observed association rates for mirror sequences.** Mirror sequences are pairs of sequences where the 5'-3' direction of one sequence equals the 3'-5' direction of the other.

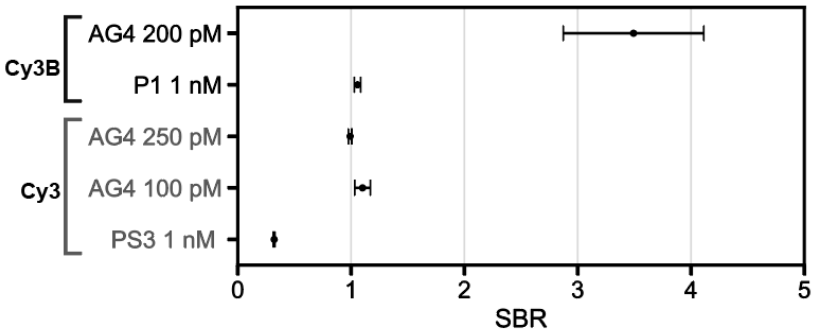


Figure 4.8: **Signal-to-background ratio (SBR) of cell images comparison between sequences** Average SBR of cell images compared between 1 nM of PS3, 100 pM of AG4, and 250 pM of AG4, which were imaged using Cy3 fluorophore; 1 nM of P1, and 200 pM of AG4, which were imaged using brighter Cy3B fluorophore. SBR is calculated for each localization by the ratio of the peak intensity and the background in number of photons, whereas the peak intensity is defined by the one-pixel area integral over the point spread function described by the Gaussian fit parameters, and the background is the off-set value per pixel [25]. Error bar denotes the standard deviation of SBR of localizations from five regions of interest in each DNA-PAINT image.

Supplementary tables

Table 4.1: Sequences of DNA oligonucleotides used for SPARXS and imaging

Name	Sequence (5′ to 3′)
Library docking strand	AATGATACGGCGACCACCGAGATCTACACTCTTTCCCTACA
	CGACGCTCTTCCGATCTATCGTTT
	RRRRRRRTTTATCTCGTATGCCGTCTTCTGCTTG
Visualization strand	CGA(T amino)AGATCGGAAGAGCGTCGTGTAGGGAAAGAG
	TGTAGATCTCGGTGGTCGCCGTATCATT
Imager library	YYYYYYY-BHQ2
Immobilization strand	Biotin-CAAGCAGAAGACGGCATACGAGAT
PS3 docking strand	TTGGGAGGA
PS3 imager strand	TCCTCCC-Cy3
AG4 docking strand	TTAGAGGGA
AG4 imager strand	TCCCTCT-Cy3(B)
P1 docking strand	ATACATCT
P1 imager strand	AGATGTAT-Cy3B

Table 4.2: Summary of sample and image parameters

Figure ID	Imager type, concentration	Laser intensity (kW/cm^2)	Camera exposure time (ms)	Number of frames	NeNA localization precision (nm)
Fig.4.3b, top	PS3-Cy3, 1 nM	0.46	50	10000	14.6
Fig.4.3b, mid	AG4-Cy3, 100 pM	0.30	50	10000	10.9
Fig.4.3b, bottom	AG4-Cy3, 250 pM	0.39	50	10000	11.7
Fig.4.3a	AG4-Cy3B, 200 pM	0.39	50	10000	7.82
Fig.4.8	P1-Cy3B, 1 nM	0.39	100	10000	9.43

References

[1] N. C. Seeman, H. F. Sleiman, DNA nanotechnology, Nature Reviews Materials 3, 17068 (2017). DOI: 10.1038/natrevmats.2017.68.

[2] P. Zhan *et al.*, Recent Advances in DNA Origami-Engineered Nanomaterials and Applications, Chemical Reviews 123, 3976–4050 (2023). DOI: 10.1021/acs.chemrev.3c00028.

[3] R. Jungmann, C. Steinhauer, M. Scheible, A. Kuzyk, P. Tinnefeld, F. C. Simmel, Single-molecule kinetics and super-resolution microscopy by fluorescence imaging of transient binding on DNA origami, Nano Letters 10, 4756–4761 (2010). DOI: 10.1021/NL103427W/SUPPL_FILE/NL103427W_SI_001.PDF.

[4] L. Piantanida, I. T. S. Li, W. L. Hughes, Advancements in DNA-PAINT: applications and challenges in biological imaging and nanoscale metrology, Nanoscale 17, 14016–14034 (2025). DOI: 10.1039/D4NR04544K.

[5] F. Schueder, J. Stein, F. Stehr, A. Auer, B. Sperl, M. T. Strauss, P. Schwille, R. Jungmann, An order of magnitude faster DNA-PAINT imaging by optimized sequence design and buffer conditions, Nature Methods 2019 16:11 16, 1101–1104 (2019). DOI: 10.1038/s41592-019-0584-7.

[6] J. SantaLucia, D. Hicks, The Thermodynamics of DNA Structural Motifs, Annual Review of Biophysics and Biomolecular Structure 33, 415–440 (2004). DOI: 10.1146/annurev.biophys.32.110601.141800.

[7] J. N. Zadeh *et al.*, NUPACK: Analysis and design of nucleic acid systems, Journal of Computational Chemistry 32, 170–173 (2011). DOI: 10.1002/jcc.21596.

[8] H. Hata, T. Kitajima, A. Suyama, Influence of thermodynamically unfavorable secondary structures on DNA hybridization kinetics, Nucleic Acids Research 46, 782–791 (2018). DOI: 10.1093/nar/gkx1258.

[9] J. X. Zhang *et al.*, Predicting DNA hybridization kinetics from sequence, Nature Chemistry 10, 91–98 (2018). DOI: 10.1038/s41557-017-0006-2.

[10] S. Hertel *et al.*, The stability and number of nucleating interactions determine DNA hybridization rates in the absence of secondary structure, Nucleic Acids Research 50, 7829–7841 (2022). DOI: 10.1093/nar/gkac624.

[11] I. Severins *et al.*, Single-molecule structural and kinetic studies across sequence space, Science 385, 898–904 (2024). DOI: 10.1126/science.adf8317.

[12] C. Bastiaanssen, I. Severins, J. Van Noort, C. Joo, Single-molecule parallel analysis for rapid exploration of sequence space, Nature Protocols 21, 689–717 (2025). DOI: 10.1038/s41596-025-01196-y.

[13] Y. Gao, Secondary structure effects on DNA hybridization kinetics: a solution versus surface comparison, Nucleic Acids Research 34, 3370–3377 (2006). DOI: 10.1093/nar/gkl376.

[14] M. E. Fornace *et al.*, NUPACK: Analysis and Design of Nucleic Acid Structures, Devices, and Systems (2022). DOI: 10.26434/chemrxiv-2022-xv98l.

[15] T. Dertinger, R. Colyer, G. Iyer, S. Weiss, J. Enderlein, Fast, background-free, 3D super-resolution optical fluctuation imaging (SOFI), Proceedings of the National Academy of Sciences 106, 22287–22292 (2009). DOI: 10.1073/pnas.0907866106.

[16] M. Glogger, C. Spahn, J. Enderlein, M. Heilemann, Multi-Color, Bleaching-Resistant Super-Resolution Optical Fluctuation Imaging with Oligonucleotide-Based Exchangeable Fluorophores, Angewandte Chemie - International Edition 60, 6310–6313 (2021). DOI: 10.1002/anie.202013166.

[17] O. K. Wade, J. B. Woehrstein, P. C. Nickels, S. Strauss, F. Stehr, J. Stein, F. Schueder, M. T. Strauss, M. Ganji, J. Schnitzbauer, H. Grabmayr, P. Yin, P. Schwille, R. Jungmann, 124-Color Super-resolution Imaging by Engineering DNA-PAINT Blinking Kinetics, Nano Letters 19, 2641–2646 (2019). DOI: https://doi.org/10.1021/acs.nanolett.9b00508.

[18] J. Li *et al.*, Exploring the speed limit of toehold exchange with a cartwheeling DNA acrobat, Nature Nanotechnology 13, 723–729 (2018). DOI: 10.1038/s41565-018-0181-y.

[19] G. Gowri, K. Sheng, P. Yin, Scalable design of orthogonal DNA barcode libraries, Nature Computational Science 4, 423–428 (2024). DOI: 10.1038/s43588-024-00591-3.

[20] S. D. Chandradoss *et al.*, Surface passivation for single-molecule protein studies, Journal of Visualized Experiments (2014). DOI: 10.3791/50549.

[21] K. de Zwaan, **R. Huo**, M. N. Hensgens, H. L. Wienecke, M. Tekpınar, H. Geertsema, K. Grußmayer, High-Throughput Single-Molecule Microscopy with Adaptable Spatial Resolution Using Exchangeable Oligonucleotide Labels, ACS Nano (2025). DOI: 10.1021/acsnano.4c18502.

[22] J. Schnitzbauer, M. T. Strauss, T. Schlichthaerle, F. Schueder, R. Jungmann, Super-resolution microscopy with DNA-PAINT, Nature Protocols 12, 1198–1228 (2017). DOI: 10.1038/nprot.2017.024.

[23] Y. Wang *et al.*, Localization events-based sample drift correction for localization microscopy with redundant cross-correlation algorithm, Optics Express 22, 15982–15982 (2014). DOI: 10.1364/OE.22.015982.

[24] U. Endesfelder, S. Malkusch, F. Fricke, M. Heilemann, A simple method to estimate the average localization precision of a single-molecule localization microscopy experiment, Histochemistry and Cell Biology 141, 629–638 (2014). DOI: 10.1007/s00418-014-1192-3.

[25] P. R. Steen, E. M. Unterauer, L. A. Masullo, J. Kwon, A. Perovic, K. Jevdokimenko, F. Opazo, E. F. Fornasiero, R. Jungmann, The DNA-PAINT palette: a comprehensive performance analysis of fluorescent dyes, Nature Methods 21, 1755–1762 (2024). DOI: 10.1038/s41592-024-02374-8.

5

Towards Multiplexed Live-cell Super-resolution Imaging with Enzymatic Labels

Multiplexed super-resolution imaging in live cells elucidates the dynamics and interactions of life at the nanoscale. A new generation of advanced fluorescent labels can be the key towards the goal of ideal microscopy. In this chapter, we benchmark two types of emerging live cell compatible labels for SOFI, the fast and gentle super-resolution imaging approach. We explore SOFI's quantitative features for multiplexed imaging along this path.

Mara Buga, master's student supervised by the author, collected and analyzed the data in Section 5.2 and contributed to this Chapter.

5.1. Introduction

With the continuous development of super-resolution imaging techniques, their application to live cells has attracted much interest. The dynamic information in biological processes revealed by live-cell imaging, especially at the nanoscale resolution enabled by single-molecule microscopy, is hard to replace with other investigations. In addition, multiplexing in live-cell imaging to visualize molecular interactions is a powerful tool that could further our understanding of numerous research topics, such as cell interactions and signaling pathways. Among super-resolution microscopy techniques, structural illumination microscopy (SIM) offers the highest temporal resolution to capture fast dynamics, with a low laser dose that benefits sample health. However, the spatial resolution of SIM is constrained, and its excitation optics and reconstruction algorithms are complex. Stimulated emission depletion (STED) microscopy offers superior spatial resolution and uses high-power lasers to deplete fluorescence. Although recent studies have shown evidence of STED-compatible live-cell imaging, its complex and costly hardware still limits large-scale applications [1, 2]. Besides, the field of view in STED is limited by the need to maintain laser intensity and image scanning speed, restricting its use in live-cell imaging that demands high throughput and statistics for screening applications. Wide-field based single-molecule microscopy at enhanced resolution, including single molecule localization microscopy (SMLM) and super-resolution fluctuation imaging (SOFI), remains a strong candidate for high-throughput live-cell imaging.

Live-cell imaging poses special demands on the fluorescent labels. First of all, the compatibility of the labeling system with the living system, i.e., whether the label could be introduced to the target proteins without interference, is crucial and determines the viability of the methods. Second, live-cell imaging requires higher brightness and specificity than fixed-cell imaging because of complex, noisy cellular environments. Finally, photostability is desired for long-term observation of dynamic processes. For single-molecule microscopy relying on the stochastic switching of the fluorophores, the photoswitching properties that influence spatial and temporal resolution require special attention.

Evaluating main experimental implementations of SMLM, DNA-PAINT is restricted to live-cell membrane labeling because of the non-permeability of DNA molecules; dSTORM, engaging UV-shifted and high-power excitation lasers in addition to chemicals for photoswitching, harms the cells, thus challenging for long-term live-cell imaging. Photoactivated localization microscopy (PALM) utilizes fluorescent proteins co-expressed with proteins of interest, which is at a disadvantage as fluorescent proteins are less photostable and bright compared to organic dyes. Similar to all SMLM methods, PALM requires strict control of the on- and off- blinking kinetics to achieve the spatial separation of emitters in every frame of a long time-series of imaging, leading to low temporal resolution and throughput. Therefore, we resolved to SOFI, which does not localize isolated fluorophores for super-resolution reconstruction. The less stringent requirement on the on- and off-blinking means SOFI can work with a broader range of labeling systems suitable for live cells and is a gentler approach than SMLM.

Blinking fluorescence arising from transient binding of the label to the target has several advantages, including programmable density and less photobleaching. In Chapter

3, we have exploited the synergy between SOFI and exchangeable oligonucleotide probes as used in DNA-PAINT. Live-cell PAINT can be facilitated with recently developed exchangeable HaloTag ligands (xHTL). xHTL is a modification of conventional ligands for HaloTags, a self-labeling protein tag derived from bacterial enzymes and co-expressed with proteins of interest, and is advantageous for live-cell imaging [3]. In HaloTag-PAINT, the HaloTag-labeled proteins can bind transiently to the xHTLs. The xHTLs are essentially rhodamine dyes with modified functional groups that non-covalently bind to the HaloTags at different affinity rates. It has been shown in applications for conventional SMLM and bleaching-resistant STED imaging [4]. HaloTag-PAINT also features controllable emitter density with varied ligand concentration and the possibility of multiplexing with sequential imaging. The potential of xHTLs for SOFI, following the optimization with DNA-PAINT-SOFI in Chapter 3, is thus interesting to explore for live-cell imaging. Their role as orthogonal labels to DNA-PAINT probes is also interesting.

Spontaneously blinking fluorophores (SBFs) have been used for high-resolution live-cell SOFI [5]. There have been rapid developments optimizing their spectrum, blinking kinetics, and photostability since the first demonstration in SOFI [6–8]. Rational design of the SBF molecules can affect the intramolecular spirocyclization equilibrium that determines the blinking kinetics, among other photophysical properties. Some newly reported SBFs have been shown to have fast blinking kinetics more suitable for SOFI than SMLM. Combining SBFs with HaloTag labeling is a simple, straightforward labeling strategy and paves the way for multiplexing and is worth evaluating in SOFI. Additionally, cellular compartments have contrasting pH values and polarity, affecting the blinking kinetics of SBFs. The sensitivity of SBFs to the microenvironment is a property exploitable for both multiplexing and biosensing.

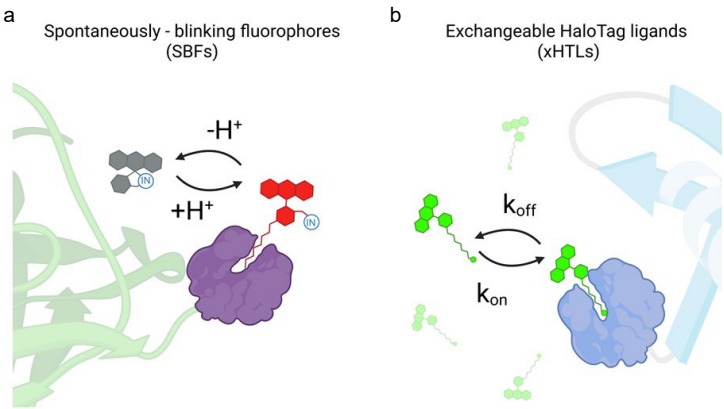


Figure 5.1: **Comparison between spontaneously blinking fluorophores (SBFs) and exchangeable HaloTag ligands (xHTLs) blinking with enzymatic labels**. **(a)** SBFs are covalently bound to HaloTags and cycle between an open, bright state and a closed, dark state at an intramolecular spirocyclization equilibrium. **(b)** xHTLs bind to HaloTags non-covalently and transiently. Image created by Mara Buga with BioRender.com.

SOFI's unique analytical quantification ability elucidates information about blinking fluorophores, including their brightness, blinking kinetics, and molecular number. This is a promising yet challenging approach for multiplexing because it requires 4th-order, high-quality SOFI [9]. Compared to other multiplexing methods in SMLM, such as spectral demixing and sequential PAINT imaging, using kinetics or other properties inherent to the dyes without additional optical modification and acquisition time is still attractive and especially desirable for live cells. Hence, screening for the labeling systems and fluorophores and optimizing for conditions leading to high-order SOFI is not only relevant for better resolution but also for a new pathway to multiplexing and quantification, which is not yet available in cellular imaging.

In this chapter, we conduct systematic characterizations of a few promising live cell compatible blinking labels introducible with HaloTags and evaluate their performance in SOFI. We optimize the labeling and imaging conditions and use metrics of resolution, photostability, and specificity to inform possible combinations for multiplexed SOFI imaging.

5.2. Characterization of self-labeling protein tags for SOFI

With novel labels intended for cell imaging, fixed-cell data is easier to obtain and valuable for optimizing the labeling protocol and imaging parameters. Therefore, we started our characterization in fixed cells for each label. Informed by the optimized fixed-cell parameters, we selected candidates for live-cell imaging. We are interested in conditions proven in fixed cells suitable for higher-order SOFI with fewer frames that could improve the temporal resolution in live-cell imaging. Following this, we initiated dual-target HaloTag labeling, combining orthogonal HaloTags co-expressed with different proteins of interest. Since HaloTags and the engineered ligands have various affinities to each other [10], careful combination of the plasmids and cell lines needs to be chosen to avoid crosstalk.

5.2.1. Exchangeable HaloTag ligands (xHTLs)

We evaluated four different xHTLs and their compatibility with SOFI, namely MaP555-Hy5, SiR-HSAM, Map555-T5, and SiR-FSAM (Fig. 5.2). These xHTLs differ in the type of fluorophores and the ligand they are fused to. For example, the SiR-FSAM is a modified SiR dye that is fused to the T5 ligand, while SiR-HSAM has another modification that enables fusion with the S5 ligand. The T5 and S5 derivatives of HaloTag ligands have different affinities for HaloTag7, consequently affecting the blinking kinetics using the HaloTag-xHTLs system. In addition, a variation of HaloTag, named dHaloTag, is orthogonal to HaloTag in terms of specificity to ligands. For dHaloTag, the ligand variant is called Hy5. An overview of the dye, ligands, and cell lines with HaloTag-labeled structures can be found in Table 5.1 in Section 5.5.

Similar to DNA-PAINT-SOFI discussed in Chapter 3, we started with titration experiments of varying xHTLs concentrations. As expected, for all the xHTLs, the density of emitters per frame increases with concentration, accompanied by an increase in the background. To reach the same density, the amount of each xHTL differs. At the same number of frames (10000) and exposure time (50 ms), we chose one concentration

for optimized SOFI reconstruction, evaluated by filament cross-section width and resolution estimation. For most xHTLs, we reached up to 4th-order SOFI reconstruction, with the best resolution performance using dHaloTag-binding MaP555-Hy5. SiR-HSAM is expected to have lower affinity for HaloTags than SiR-FSAM, based on higher dissociation coefficients from in vitro data in the literature; however, in cellular labeling, they did not show this difference. MaP555-T5 is expected to show similar blinking kinetics to SiR-FSAM because the dyes are fused to the same type of ligand; however, a higher concentration was needed to achieve similar density for MaP555-T5, leading to worse SNR. Supplementary figure 5.8 includes more SOFI results from the xHTLs labeling cellular structures with different morphologies, showing their versatility. Concentration-dependent kinetics are consistent across different targets, for example, MaP555-Hy5 is found to reach high-order SOFI at 10 – 50 nM concentration whether labeling filamentous vimentin or punctiform H2B. 20 – 100 nM is recommended for SiR-HSAM. An additional xHTL, JF636-HSAM, is shown in Supplementary Figure 5.9 from earlier experiments but was excluded from further two-color experiments due to material degradation. In general, the in vitro kinetics data from the literature, summarized in Table 5.4, did not inform us well about the blinking kinetics in cellular labeling. In addition, we observed labeling heterogeneity in cells, necessitating optimization in cellular environments.

We selected two xHTLs for evaluation in live cells: MaP555-Hy5 and SiR-HSAM. This choice is influenced by the SOFI quality from fixed cell data and by the fact that this combination within the available xHTLs is possible to introduce orthogonal labeling at different color channels. It is immediately noticed that much fewer xHTLs are needed for live-cell labeling to reach a similar density as in fixed cells, hypothetically due to a lack of damage to the HaloTag from fixatives and temperature-promoted diffusion (Fig.5.3). Live-cell experiments used far less laser power and a reduced exposure time of 20 ms. To explore the possibility of fast SOFI with fewer frames for better temporal resolution, we compared the lower-emitter and higher-emitter conditions. For both xHTLs, at the low emitter density condition, we could reconstruct 2nd-order SOFI from 5000 frames. Rolling this window starting every 2500 frames, we followed the dynamic mitochondrial network within 150 or 300 seconds. When increasing the emitter density, for MaP555-Hy5, 2nd-order SOFI was attainable with 3000 frames; for SiR-HSAM, 2nd-order SOFI was attainable within 1000 frames. This gives us temporal resolution of 60 seconds and 20 seconds, respectively, which allowed for observation of mitochondria fusion, however still not sufficient for many cellular dynamic processwa. We overlapped image frames with the rolling window analysis to avoid averaging the moving structure and help identify intermediate dynamics.

5.2.2. Spontaneously blinking HaloTag ligands

Two different SBFs were evaluated in fixed cells first, namely HM-SiR and NL-309. Unlike xHTLs, the blinking kinetics of SBFs are less controllable once the labeling is done with a certain concentration of SBFs fused to HaloTag ligands. Therefore, we explored their response to environmental pH under fixed-cell conditions, as this information would clarify their potential as cellular sensors when attached to organelles with different pH values. For both SBFs, emitter density increases at lower pH (Fig. 5.4 (a-b)). This is

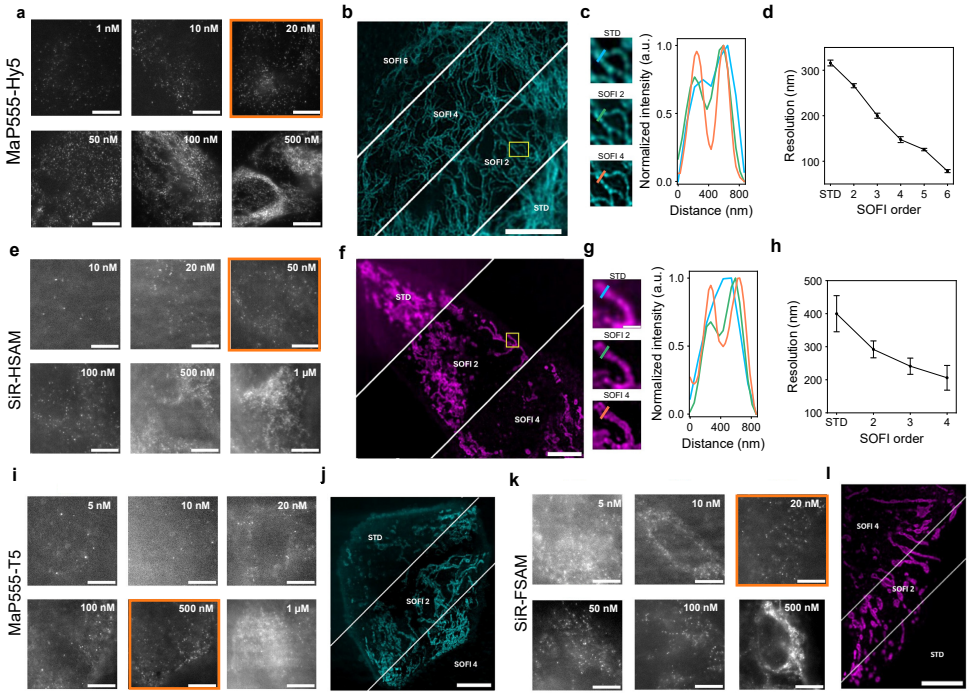


Figure 5.2: **Exchangeable HaloTag ligands (xHTL) in fixed-cell imaging. (a-d)** MaP555-Hy5 labeled VIM-dHT7: **(a)** xHTL concentration titration experiment showing emitter density per frame changes, scale bar 10 μm; **(b)** SOFI reconstruction of different orders at 20 nM concentration, scale bar 5 μm, STD is the standard deviation projection of image stack; **(c)** Zoom-in of (b), with line profile of the filament cross-section; **(d)** Resolution estimation of SOFI images. **(e-h)** SiR-HSAM labeled TOM20-HT7: **(e)** xHTL concentration titration, scale bar 10 μm; **(f)** SOFI reconstruction of different orders at 50 nM concentration, scale bar 5 μm; **(g)** Zoom-in of (f), with line profile of the microtubule cross-section; **(h)** Resolution estimation of SOFI images. **(i-j)** MaP555-T5 labeled TOM20-HT7: **(i)** xHTL concentration titration, scale bar 10 μm; **(j)** SOFI reconstruction of different orders at 500 nM concentration, scale bar 10 μm. **(k-l)** SiR-FSAM labeled TOM20-HT7: (k) xHTL concentration titration, scale bar 10 μm; (l) SOFI reconstruction of different orders at 20 nM concentration, scale bar 10 μm.

expected, as the spirocyclization protonation reaction shifts toward the open fluorescent molecular structure at higher H+ concentrations. However, at pH values of 4.5 or 5.5, no SOFI could be qualitatively reconstructed, possibly due to damage to the structures under those acidic conditions. Besides the emitter density in relation to the off-time, the on-time of SBFs also changes with pH. We conducted preliminary quantitative analysis

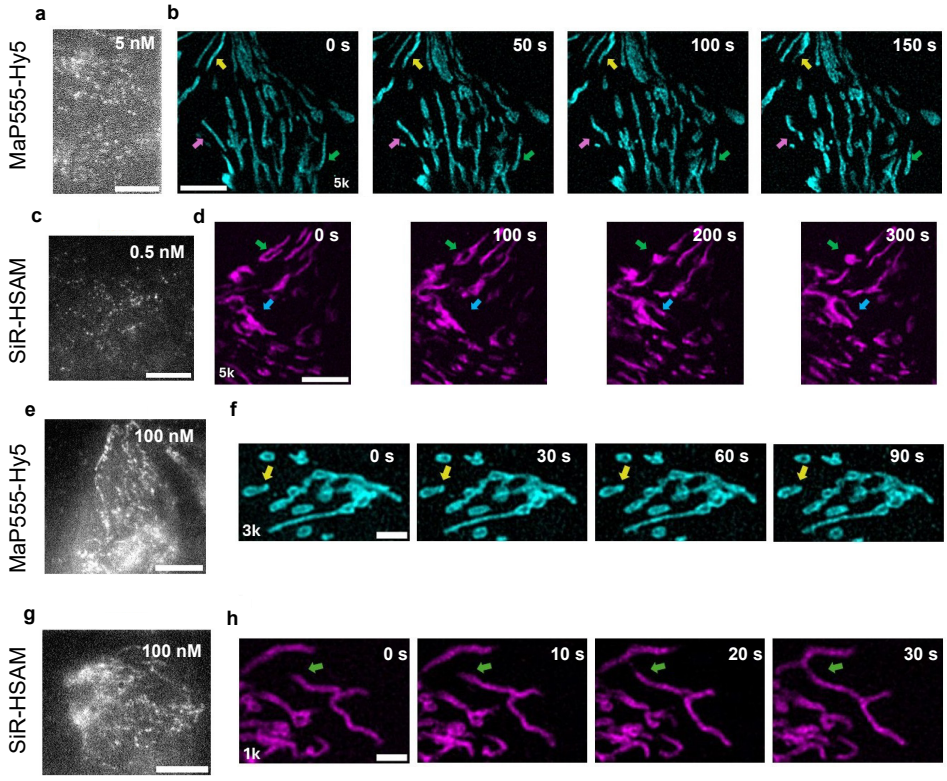


Figure 5.3: **Exchangeable HaloTag ligands (xHTL) in live-cell imaging. (a-d)**: TOM20-(d)HT7 labeled with low xHTL concentration. The gray-scale image is one raw frame showing emitter density. 5000 frames were used to reconstruct 2nd-order SOFI, with sliding window of 2500 frames apart, scale bar 5 μm, arrows indicate mitochondria morphology changes during imaging, time stamps indicate the starting time of the time window. **(e-h)** same samples using higher xHTL concentration: **(f)** 3000 frames were used to reconstruct one 2nd-order SOFI, with a sliding window of 1500 frames apart; **(h)** 1000 frames were used to reconstruct one 2nd-order SOFI, with a sliding window of 500 frames; scale bar 2 μm.

of blinking kinetics, including on- and off-times, which is challenging, especially in high-density images (Supplementary Figure 5.11). The results capture the decreasing on-time trend with higher pH.

Both dyes were designed and calibrated to have the best SMLM performance at physiological pH of 7.5. At this value, we could obtain 3rd-order SOFI at a mere 20 ms exposure time (Fig. 5.4 (c)). This is motivated by the idea of using this labeling system in

live-cell conditions with better temporal resolution. Notably, at high pH values, when the on-time is shortened, SOFI retains resolution at exposure times as low as 10 ms (resolution, SOFI 3: 255 nm; 20 ms, SOFI 3: 262 nm), while SMLM lost its contrast due to few photons detected in comparison (Fig. 5.4 (d)). This promotes SOFI as a more robust super-resolution algorithm for varying blinking conditions and imaging parameters. Proceeding to live-cell imaging using SBFs, we could follow mitochondrial dynamics within 70 s, with every 1000 frames starting at 500 frames apart. For the same number of frames, SMLM reconstruction is harder to track and the structure is less defined (Fig. 5.5).

5.2.3. Dual-color live-cell super-resolution combining xHTLs and SBFs

Dual-color live-cell imaging with HaloTag systems faces the challenges of transfection efficiency, crosstalk, autofluorescence, phototoxicity, and so on. We introduced a dHaloTag-containing plasmid (TOM20-dHT7) into HaloTag-containing stable cell lines (Lamp1-HT7). Lysosomes have been shown to show contacts with mitochondria during mitochondrial fission and mitophagy, which can facilitate the improvement or restoration of mitochondrial function in cells, thus constituting a good system for super-resolution observation [11].

After verification in fixed cells (Supplementary figure 5.10), two combinations of HaloTag ligands were used to label the HaloTags or dHaloTags. The first combines two types of xHTLs, MaP555-Hy5 and SiR-FSAM, and the second combines xHTL MaP555-Hy5 with SBF HM-SiR. Both labeling combinations showed 2nd-order SOFI reconstruction with 1000 frames, giving sub-diffraction insights into mitochondrial fission in proximity to lysosomes (Fig. 5.6).

5.3. Roadmap to multiplexed live-cell imaging with SOFI

As hinted in Chapter1, SOFI has a unique quantification ability to analytically map molecular parameters, provided a good 4th-order SOFI. Those parameters include blinking kinetics, brightness, and density, which could be exploited for multiplexing. Kinetics and brightness multiplexing have been explored in DNA-PAINT, respectively [12, 13], but neither is robust under cellular conditions, and neither applies to live cells.

With the abundance of candidate labels for high-order SOFI tested so far, we envision a promising pathway towards multiplexed and live-cell SOFI through parameter estimation. To start, by combining conventional slower-blinking DNA-PAINT labels with the fast ones we have used (Chapter 3) and discovered by SPARXS (Chapter 4), we could multiplex by blinking kinetics with SOFI in fixed cells. Because SOFI is compatible with much faster blinking conditions than SMLM, multiplexing order can be higher. Establishment of the DNA-PAINT-SOFI kinetics multiplexing workflow could be transferred to HaloTag-PAINT in live cells using enzymatic labels evaluated in the previous sections, or as orthogonal labels in addition to the DNA-PAINT labels. Results shown in Figure 5.2 give us a large variation in kinetics that we could experimentally modify, for example the SiR-HSAM and SiR-FSAM at low concentrations show very distinctive emitter density.

Similar ideas extend to brightness multiplexing using fluorophores that overlap in spectrum but differ in brightness. For this, the bright organic dyes are more promising.

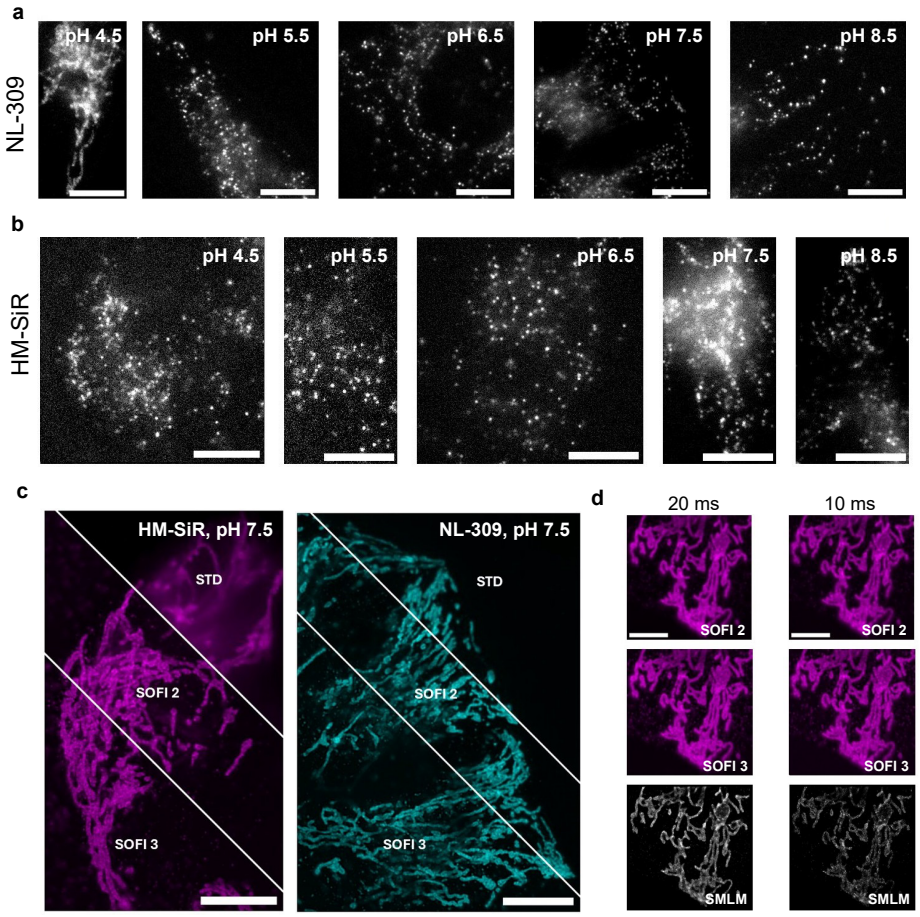


Figure 5.4: **Spontaneously blinking fluorophores (SBFs) in fixed cell imaging. (a)** pH titration experiments with NL-309 labeled TOM20-HT7, emitter density varies, scale bar 10 μm. **(b)** pH titration experiments with HM-SiR labeled TOM20-HT7, scale bar 10 μm. **(c)** SOFI reconstruction at pH = 7.5, scale bar 10 μm. **(d)** Comparison between SOFI and SMLM, with two different exposure times under fast-blinking conditions.

Those dyes are available in DNA-PAINT imagers (Cy3 vs Cy3B, Atto655 vs Atto647N), as well as SBFs (HMSiR and NL309, both red).

Figure 5.7 shows preliminary data on the possibility of kinetics multiplexing by SOFI. SOFI outputs kinetics as an on-time ratio map of the image. Masking the map with 4th-order SOFI isolates the structures, followed by statistical analysis of the pixel values underlying the on-time ratio of labels. We compared two datasets with fast and slow blinking kinetics, respectively, which yielded distinct peaks. Efforts remain in data

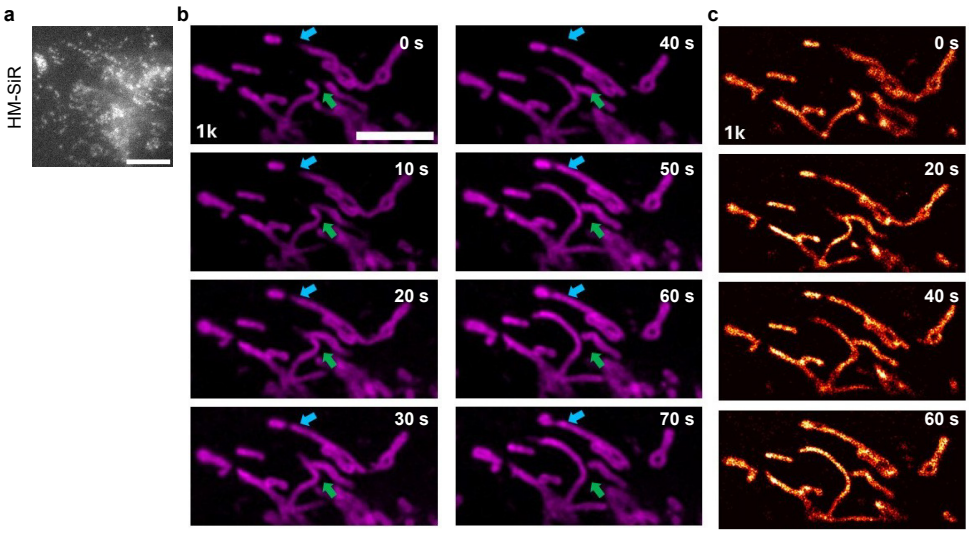


Figure 5.5: **Spontaneously blinking fluorophores (SBFs) in live-cell imaging.** HM-SiR labeled TOM20-HT7. **(a)** One raw frame showing emitter density, scale bar 10 μm. **(b)** 1000 frames were used to reconstruct SOFI image, with sliding window 500 frames apart. **(c)** SMLM reconstruction using every 1000 frames. Scale bar 5 μm.

processing for reliable classification in accordance with experimentally tuned kinetics.

5.4. Discussion

With the main focus of single-molecule microscopy today being SMLM, it is not straightforward to bring novel fluorescent labels optimized for SMLM to SOFI. Systematic testing of the labels, from xHTLs and SBFs to HaloTag labeling, is therefore essential. It is particularly valuable to determine suitable kinetics based on the sample and imaging settings. With optimized conditions, we found that xHTLs and SBFs are generally compatible with SOFI, achieving 4th-order SOFI in fixed cells and 3rd-order SOFI in live cells. We investigated blinking kinetics as a function of concentration and pH, which is advantageous for tuning spatiotemporal resolution by switching between SOFI and SMLM, since buffer exchange is relatively simple. We have set up a workflow for two-target live-cell labeling using orthogonal HaloTags and successfully combined two species of blinking ligands, xHTL and SBF-fused ligand, for two-target labeling simultaneously. This two-target labeling system by HaloTags is verified with simple spectral separation, i.e., imaging with dyes of different colors in separate optical channels. The orthogonal labeling system prepares us for multiplexing by differentiating parameters other than spectrum to avoid chromatic aberration, including kinetics, molecular density, and brightness reported by SOFI.

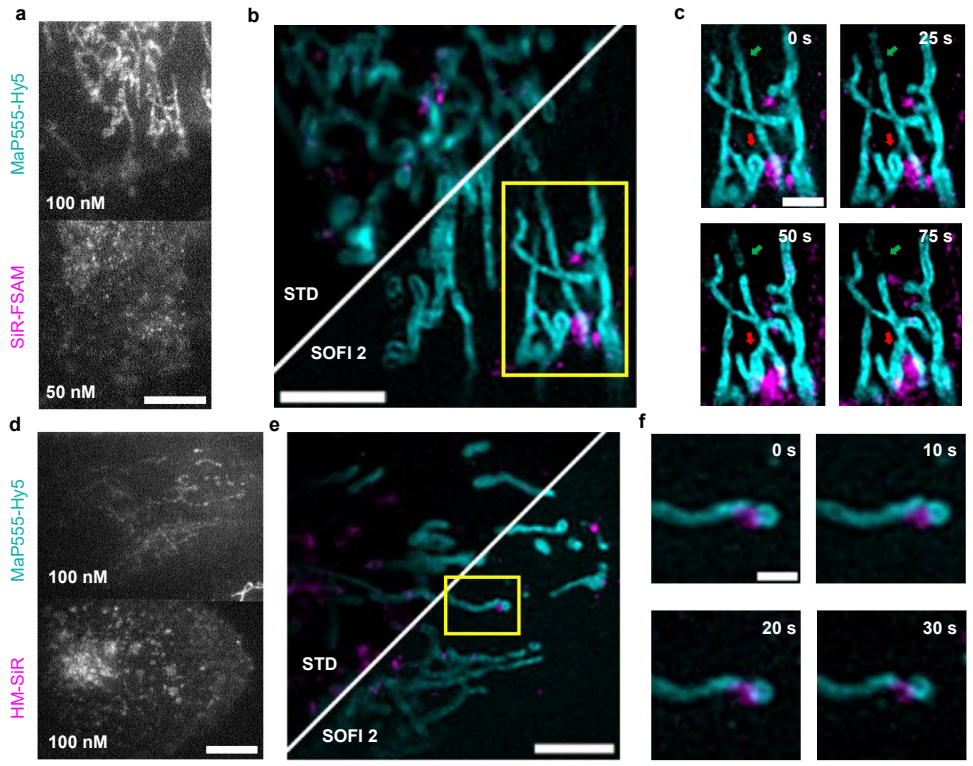


Figure 5.6: **Dual-color live-cell SOFI with HaloTag labeling system (a-c)** Dual-color imaging of MaP555-Hy5 labeled TOM20-dHT7, and SiR-FSAM labeled Lamp1-HT7. **(d-f)** Dual-color imaging of MaP555-Hy5 labeled TOM20-dHT7 and HM-SiR labeled Lamp1-HT7, showing mitochondrial fission at lysosomes involvement over time. Gray scale images show one raw frame of both color channels, scale bar 10 μm. Large FOV in (b) and (e): scale bar 5 μm. Zoom-in time series in (c) and (f): scale bar 1 μm. 2nd-order SOFI reconstructed from 1000 frames with sliding window 500 frames apart.

Compared to immunostaining used in previous chapters, HaloTag labeling is simpler in sample preparation and has less adverse effect on the target protein through co-expression. It is therefore an ideal system for multi-target live-cell imaging. The challenge of transfection in live cells remains, which motivates us to explore stably transfected cell lines or CRISPR cell lines in the future. We found it encouraging that both HaloTag labeling systems tested have tolerable photobleaching, in both fixed and live cells (Supplementary figure 5.12). We observed cross-talk between targets for Vimentin-dHT when labeled with non-cognate labels, which couldn't be explained by in vitro data and should be avoided in two-target experiments.

Our evaluation is limited to the materials available from collaborators. Other newly

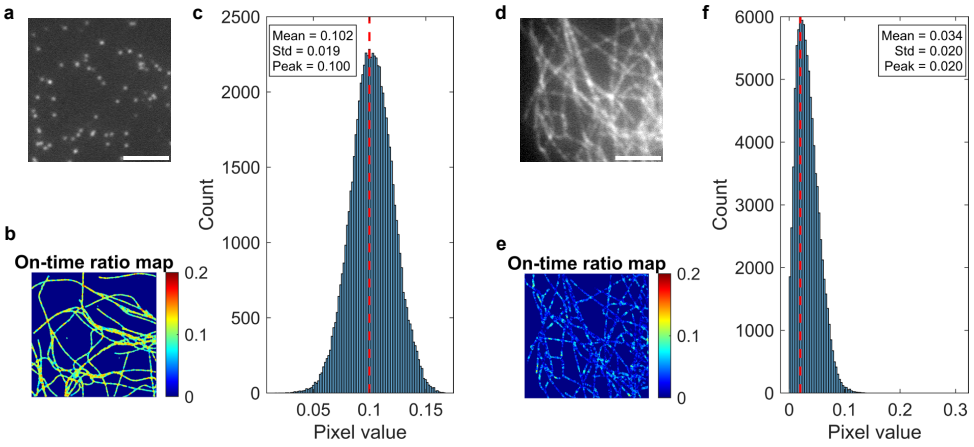


Figure 5.7: **Concepts validation of kinetics multiplexing by quantitative SOFI (a-c)** DNA-PAINT labeled by 25 pM 5R1–Atto 655; **(d-f)** DNA-PAINT labeled by 5 nM 5R1–Atto 655 with addition of 5% ethylene carbonate. (a) and (d): raw image showing the emitter density, scale bar 5 μm. (b) and (e): SOFI on-time ratio map. (c) and (f): histogram of pixel values of the on-time ratio map.

proposed SBFs and labeling systems are worth investigating to identify potential candidates. For example, recent literature reported a series of SBFs, one of which (JF635b) was tested for 2nd-order live-cell SOFI with 5000 frames at 10 ms exposure time [6]. Rho-tag and SiR-tag, recently developed for live-cell imaging, bind to rhodamine dyes with a weak affinity. Their high permeability and fluorogenicity, and low affinity to HaloTags, could be introduced to increase multiplexing with HaloTag and dHaloTag to higher than 2-plex.

Optimization in SOFI is a process not clearly defined. Visual inspection of image quality, focusing on structural integrity, contrast, and artifacts, is our primary assessment for high-order SOFI viability. Quantification methods, including resolution estimation and SNR analysis, can be helpful in optimizing acquisition and SOFI processing parameters, including the number of frames and deconvolution iteration number, within the same sample and imaging condition. Decorrelation as a parameter-free resolution estimation is generally reliable; however, it has a bias to overestimate point-like structures due to higher spatial frequencies from the sparsely distributed dots, which can be seen in the drastic resolution improvement in the lysosome channel compared to mitochondria in Fig. 5.10 [14]. Moeyaert et al. suggested high-order SOFI is only a matter of higher frame number if 2nd-order SOFI is attainable [15]. This underscores our next endeavor: optimizing the number of frames in higher-order SOFI for dynamic imaging.

Methodology development should serve the goal of solving biological questions. From designing and synthesizing new fluorescent probes to verifying them in imaging methods and applying them to real biological samples, each step involves calibration and optimization. This chapter, like most super-resolution methodology development

work, is to be supported by application in more complex biological models beyond resolution in well-defined structures. We attempted to track mitochondrial dynamics in the two-color live-cell imaging pilot experiment. Fusion and fission processes in mitochondrial membrane morphology are related to the regulation of metabolic homeostasis, and lysosomes can facilitate the improvement or restoration of their functions [16, 17]. For imaging mitochondrial dynamics, SIM and STED have been used with temporal resolution over seconds [18, 19], while SMLM is usually limited to tens of seconds [20, 21]. Our results present SOFI as offering moderate temporal resolution up to 20 s with minimal technical requirements. However, the strength of SOFI lies in its tunable flexibility, manifesting both in experimental conditions and post-processing outcomes. Future work will explore this aspect in a similar fashion presented in Chapter 3.

5.5. Methods and Materials

All cell and HaloTag materials were gifted from Prof. Kai Johnsson's group at Max Planck Institute for Medical Research, Heidelberg, except for the HTL-HMSiR (A201-01, 02 HaloTag SaraFluor™ 650B Ligand, Key Organics).

Cell lines and culture

The cell lines in Table 5.1 present stable plasmid expression generated with a Flp-In™ T-Rex™ system used to integrate the plasmid gene in the host genome for stable, isogenic expression inducible by doxycycline. Stable transfection prevents the need for continuous and highly variable transient transfections. The plasmid expression inducibility allows cells to grow without the influence of the transfected protein in the majority of the time, minimizing the potential detrimental effects of the protein on cell growth, which can occur in the case of a constitutively expressing gene. In case molecular targets were needed that were not available in stable cell lines, or a second target site needed to be created in a stable cell line, transient transfections were performed with the plasmids in Table 5.2.

For both stably and transiently transfected plasmids, the induction system is a Tet-off system, where the Tet repressor gene is constitutively expressed. The TetR protein produced by the gene dimerizes and binds to Tet operator 2 sites integrated after the promoter of the gene of interest, preventing gene-of-interest transcription. When doxycycline is added, it binds with high affinity to TetR homodimers, causing a conformational change that prevents them from binding to the Tet operator 2 sites and repressing transcription. Thus, TetR-doxycycline complexes dissociate from the DNA and the gene of interest can be transcribed.

The cell culture medium used for all experiments was Dulbecco's modified Eagle's medium (DMEM) with high glucose (ThermoFisher) without phenol red indicator, because phenol red could interfere with imaging by increasing background fluorescence. The medium was supplemented with 10% fetal calf serum (FCS, Gibco, ThermoFisher) and 1% penicillin/streptomycin (P/S, Gibco, ThermoFisher). This medium was used in all experiements (except for transfections), and will be further referred to as "medium". The medium was stored at 4°C and warmed in a 37°C water bath before use in cell culture

Table 5.1: Stable U2OS cell lines with (d)HaloTags

Cell line	Biological structure tagged	HaloTag
TOMM20-dHT7-T2A-GFP	Mitochondrial outer membrane	dHT7
TOMM20-HT7	Mitochondrial outer membrane	HT7
Vim-dHT7-T2A-eGFP	Vimentin	dHT7
H2B-dHT7-T2A-eGFP	Histone H2B	dHT7
H2B-HT9-T2A-eGFP	Histone H2B	HT9

Table 5.2: Plasmids for HaloTag labeling

Plasmid	Biological structure tagged	HaloTag
Lamp1-HT7	Lysosome	HT7
B4G-HT7	Golgi apparatus	HT7
LaminB1-HT7	Nuclear membrane	HT7
CalR-HT7-KDEL (JHp1147)	Endoplasmic reticulum	HT7
CalR-HT7-KDEL (JKp0025)	Endoplasmic reticulum	HT7
Vim-dHT7-T2A-GFP	Vimentin	dHT7
Vim-HT7-T2A-GFP	Vimentin	HT7

experiments. All U2OS cell lines were kept for long-term storage at −150°. To thaw cells, a cell tube was removed from the freezer and warmed up in the 37°C water bath. This process was done quickly, since cells are frozen in medium with dimethyl sulfoxide (DMSO), which is toxic to cells under normal growth conditions. Therefore, the aim was for the thawed cells to be in minimal contact with the high DMSO concentration. Once the cells were thawed, the tube was brought to a cell culture cabinet to ensure sterile conditions. The cells in the tube were washed with 5 mL of fresh medium and pipetted into a 15 mL tube. The tube was centrifuged at 1000 rpm for 5 minutes. Afterwards, the supernatant (containing diluted DMSO) was removed, and the cells were resuspended in 10 mL of fresh medium. Depending on the desired cell density, the cell suspension was pipetted into one or several 10-cm cell culture dishes, and fresh medium was added for a final volume of 10 mL of cell suspension per dish. The cell dishes were kept in a 37°C incubator in 5% CO_2 conditions.

The cells were passed twice a week (in approximately 1:8 dilution). The cell medium was not refreshed between the splitting time points. For passing, the cell plates were washed twice with PBS 1x. 1 mL of T/E was added to each plate, and the plate was incubated with the enzyme for approximately 1 minute at 37°C. We verified cell detachment with a wide-field microscope. The cells were then supplemented with 9 mL fresh medium to dilute the T/E, and the suspension was pipetted up and down to facilitate mixing and near-complete cell detachment. The cell suspension was split into

10-cm dishes. Fresh medium was supplemented to the new dishes for a total volume of 10 mL per dish.

For imaging experiments, the cells were typically seeded on precision cover glasses #1.5H (Marienfeld). Before seeding, the coverslips were plasma-cleaned in order to make the surface hydrophilic and facilitate cell adhesion. As such, the coverslips were exposed to oxygen for 30 seconds and to plasma treatment for 2 minutes. Afterwards, the coverslips were placed in 6-well plates inside the sterile flow cabinet. In each well containing a coverslip, 1.9 mL of fresh medium was added, then the plate was placed in the 37°C incubator under 5% CO2 conditions to facilitate protein adhesion to the coverslip, which would then lead to better cell attachment. 80-100 % confluent 10-cm dishes were washed two times with PBS 1x and 1mL T/E was added for cell detachment. The cell suspension was supplemented with 9 mL of fresh medium, and the suspension was pipetted up and down to facilitate mixing and near-complete cell detachment. Afterwards, the 6-well plate with the coverslips was removed from the incubator and 150-170 μL of cell suspension (depending on initial dish confluency) were added to each well. Lastly, 4 μL of 50 ng/mL doxycycline was added to each well (for a concentration of 100 ng/mL) in order to induce the plasmids. Following the results of previous optimization experiments performed in our group, the 6-well plates were kept in a 37°C incubator in 5% CO2 conditions for 48 h before imaging or fixation, to allow the doxycycline to induce plasmid expression.

Cell transfection

The stable cell lines in Table 5.1 only have one plasmid transfected with one target gene – HaloTag fusion. In order to create two target sites for dual-color imaging, a second target was added through the transfection of one of the available plasmids (Table 5.2). The plasmid was chosen such that the two labeled structures in the U2OS cells would be fused to different types of HaloTag (i.e., one structure fused to HT7 and the other fused to dHT7).

We performed two types of transfection: chemical (lipofection) and physical (electroporation). Since electroporation led to better cell survival and transfection efficiency (upon qualitative assessment of GFP expression under the EVOS microscope), as well as required less time to be performed, this became the preferred transfection method. In all the multicolor imaging results included in this thesis, transfection of a second structure plasmid was obtained through electroporation.

Lipofection

Before transfection, the cells were seeded in a 12-well plate in order to minimize the use of transfection reagents. To ensure the cells reach an appropriate confluency (70-90%) by the time of transfection, a range of cell suspension dilutions was seeded. The cells were cultured in medium without P/S ("transfection medium") to minimize cell stress during transfection. Chemical transfection with Lipofectamine 3000 (Invitrogen, ThermoFisher) was performed when the cells were 70-90% confluent.

In one tube, a mix of 50 μL Opti-MEM (Gibco, ThermoFisher) and 0.15 μL Lipofectamine 3000 was prepared, vortexing to ensure thorough mixing. In a second

tube, the DNA master mix was prepared by diluting 1 ng of the plasmid DNA in 50 μL Opti-MEM and 2 μL P3000 reagent (Invitrogen, ThermoFisher), ensuring thorough mixing by pipetting. The Lipofectamine mix was added to the DNA mix in a 1:1 ratio. This final mix was incubated for 30 minutes at room temperature, covered with aluminum foil. During this time, the cells in the 12-well plate were refreshed with 900 μL of transfection medium per well. After incubation, 100 μL of transfection mix were added to each well. The cells were incubated for 16- 24 h at 37°C, in 5% CO2 conditions.

After transfection, the cells were seeded on coverslips in a 6-well plate as in Section 2.1.5, but in transfection medium. The plasmids were induced with 100 ng/mL doxycycline, and the cells were fixed on the coverslip about 48 h after plasmid induction.

Electroporation

For electroporation, a Neon™ NxT Electroporation System (NEON1S, Invitrogen) was used. Before electroporation, a 6-well plate with oxygen-plasma-cleaned coverslips and 2 mL transfection medium in each well was prepared and placed at 37° in 5% CO_2 conditions to facilitate protein adhesion to the glass.

Cells at 70-80% confluency were detached with T/E, resuspended in 10 mL transfection medium, and counted using a Countess 3 FL Automated Cell Counter (AMQAF2000, Invitrogen). In brief, 10 μL of 0.4 % Trypan Blue Solution (Gibco, ThermoFisher) was added to 10 μL of cell suspension and gently mixed by pipetting. 10 μL of the mix was pipetted into each of the two chambers of a Countess Reusable Slide (Invitrogen, ThermoFisher). The slide was then inserted into the cell counter, which counted the live and dead cells in the sample. The two live cell counts from the two chambers were averaged to estimate the number of cells in 1 mL of suspension. Based on this, a suspension volume corresponding to the number of cells required for the experiment (approx 0.5×10^6 cells/well) was centrifuged at 300 g for 5 minutes. The supernatant was then discarded, and the cells were resuspended in 10 mL PBS 1x and centrifuged once more at 300 g for 5 minutes to ensure thorough washing. The supernatant was then discarded carefully, aiming to leave as little liquid as possible without disturbing the pellet. Afterwards, the pellet was resuspended in 10 μL Resuspension Buffer R (ThermoFisher) per well, making sure to prepare a sample for an extra well in case of electroporation issues. The plasmid DNA solution was mixed with this cell suspension in a tube, with 10 μL cell suspension and 0.5-1 μg plasmid per well. Generally, a plasmid concentration of 0.5 μg per well led to better transfection results.

The electroporation arm was placed inside the cell culture hood, and 3 mL of Electrolytic Buffer E (ThermoFisher) was pipetted inside the electroporation tube. The electroporation pipette with 10 μL electroporation tips was used to take up 10 μL of the cell-DNA mixture and then placed in the electroporation arm, such that the tip was immersed in the buffer. The electroporation could then be started, with 1150 V delivered in 4 pulses of 10 ms. After electroporation was completed, the sample was pipetted into its respective well in the 6-well plate. 100 ng/mL of doxycycline was added for 48 h to induce plasmid expression, after which the cells were imaged or fixed.

Cell labeling

For fixed cell imaging, seeded cells were incubated with 4% paraformaldehyde (PFA, ThermoFisher) in PBS 1x for 15 minutes. Afterwards, the plate was washed with PBS 1x and placed on a shaker for 5 minutes. The washing and shaking process was repeated three times. The coverslips were stored in 2mL PBS 1x at 4°C.

For live-cell imaging, the cells were seeded in 35 mm high 1.5 coverslip bottom μ-dishes (ibidi, 81158) or 35 mm dishes 1.5 coverslip 14 mm glass diameter (Mattek, P35G-1.5-14-C), using the same amount of cells and the same doxycycline concentration as for a well in a 6-well plate. The cells were incubated for 48 h at 37°C in 5% CO_2 conditions before imaging.

For cells labeled with xHTLs, the staining could be performed right before imaging, as it was based on the cells being in contact with the exchangeable fluorophores in the buffer. For imaging fixed coverslips, the imaging buffer consisted of xHTLs diluted to the desired concentration in PBS1x. The coverslip was mounted in contact with the imaging buffer shortly before imaging. For imaging live cells in microscopy dishes, the imaging buffer consisted of xHTLs diluted to the desired concentration in medium with 20 mM HEPES buffer. The HEPES buffer helped mitigate the possible changes in medium pH caused by the lack of CO_2 control at the microscope. We first used a 2 h incubation time with the xHTLs; however, a shorter incubation time also proved effective.

For cells labeled with SBFs, the labeling was done overnight before the day of fixation or imaging. The cell medium was exchanged for medium with SBF diluted to the desired concentration. Before imaging or fixation, the medium with SBF was exchanged for fresh medium, in order to wash away the unbound fluorophore. The cells were incubated in the fresh medium for 2 h, after which the coverslips were fixed or imaged. For imaging fixed coverslips, the imaging buffer was PBS 1x. For imaging live cells in microscopy dishes, the imaging buffer was 20 nM HEPES medium.

For the pH titrations, the buffer pH was adjusted by adding acids (HCl) and bases (NaOH) until the desired pH was reached. This was measured with a pH meter.

In two-target labeling experiments, the two xHTLs were diluted in the imaging buffer before adding the buffer to the sample and imaging, as described for single targets. When one SBF and one xHTL were used, the SBF labeling was done overnight. Then the medium was replaced with imaging buffer in which the xHTL was diluted to the desired concentration. The sample was incubated for 2 h, then imaged.

The following tables provide an overview of HaloTag ligands used for labeling.

Table 5.3: Spontaneously-blinking fluorophores

Fluorophore	**Ligand**	**HaloTag**	**Abs/Em Max (nm)**	**On time (ms)**	**Off time (s)**
HTL-NL325	HTL	HT7	512/535	3.6 ± 0.2	131 ± 14
HTL-NL309	HTL	HT7	559/582	13.1 ± 0.3	11 ± 2
HTL-NL125	HTL	HT7	513/531	N.D.	N.D.
HTL-HMSiR	HTL	HT7	654/669	N.D.	N.D.

Table 5.4: Exchangeable HaloTag ligands

Fluorophore	Ligand	HaloTag	Abs/Em Max (nm)	k_{on} (10^6 $M^{-1}s^{-1}$)
MaP555	T5	HT7	553/580	8.1 (7.8–8.5)
MaP555	Hy5	dHT7	553/580	15.6 (14.9–16.3)
JF635	S5	HT7	635/652	6.0 (5.5–6.6)
SiR	T5	HT7	652/674	5.5 (5.1–5.8)
SiR	S5	HT7	652/674	4.0 (4.4–4.9)

For mounting the coverslips on concave slides, with a concave dent in which buffer could be pipetted, the slides were first cleaned with 70% ethanol. 100 μL of imaging buffer was pipetted into the concave dent of the slide. Afterwards, a coverslip was placed on the slide, on top of the dent, making sure that the side with the cells is in contact with the imaging buffer. The excess buffer on the edges of the coverslip was removed gently with a tissue. The coverslip was then fixed to the slide by applying nail polish on the edges, making sure that no buffer could leak.

To enable buffer exchange for fluorophore concentration/ pH exchange purposes, coverslips were mounted as previously described on concave coverslips with two drilled holes in the concave well. A p200 pipette could be used for buffer exchange by inserting the tip in one of the holes to remove the previous buffer and add new one. The buffer was pipetted slowly but firmly, such that the dent could be filled and air bubbles could be avoided.

For easier buffer exchange, the coverslips with fixed or live cells were mounted on two-piece metal rings. The metal pieces were cleaned with 70% ethanol before sample mounting. With tweezers, a coverslip was placed on the lower part of the ring, then the upper part of the ring was screwed on. 1 mL of imaging buffer was slowly added to the ring, making sure that no leakage occurred due to loose screwing. A third piece of the ring could be used to seal the top part of the buffer chamber with a second coverslip.

Microscope description

Two setups were used for imaging. The first one is Open Blink microscope described as in Chapter 2. A heating element was added to Open Blink to facilitate live-cell imaging. Flexible heating foil (Omega KHLVA-0504/10-P) is wrapped around the objective, enabling heat transfer through the objective lens and immersion oil to the sample coverslip. For calibration, two temperature sensors (RS, PT100) were used to measure the temperature difference between the sample and the objective, such that the appropriate temperature is delivered to the objective for the sample to be at 37° during imaging. A PID temperature controller (Omron, E5CC-QX3A5M-003) monitors the temperature sensor glued onto the objective to keep the temperature stable during live-cell imaging.

Gataca iLAS TIRF microscope setup of the Kavli Nanolab Imaging Centre was also used, due to the better temperature control available in a commercial setup. The microscope included 4 CW lasers (405/488/561/638) and allowed for TIRF/HILO/widefield

illumination. The stage was motorized in XY and included hardware z-drift compensation (Nikon perfect focus). The setup also included an incubation box for temperature control. For SR imaging, a 100x Apo TIRF oil objective was used. The emission passed through bandpass filters (609/54, 708/75, Semrock) before being captured on an Andor iXon Ultra 897 EM-CCD camera. The image acquisition was performed through the INSCOPER 9.0.6 software. To measure the laser intensity at the sample plane, an optical power meter for laser (Thorlabs) with a microscope slide sensor head was used. The slide sensor was mounted on the microscope stage and brought close to the objective, at a similar height to the sample focus. Afterwards, the laser was turned on, using the same settings as for sample imaging (power, illumination modality (TIRF), incubation box temperature). The displayed value, within a standard deviation of ± 0.002 mW, was recorded. To estimate the laser power density at the sample plane, we used the field-of-view size as a proxy for the illuminated area.

Image analysis

SOFI reconstruction, decorrelation resolution estimation, and Jackknife SNR analysis were done in the same fashion as in Chapter 3.

5.6. Data Availability

All SOFI reconstructions in this Chapter are publicly available at https://doi.org/10.4121/bcf01712-4f8d-4f12-bfc6-84fed4ddc086.

5.7. Appendix

Supplementary figures

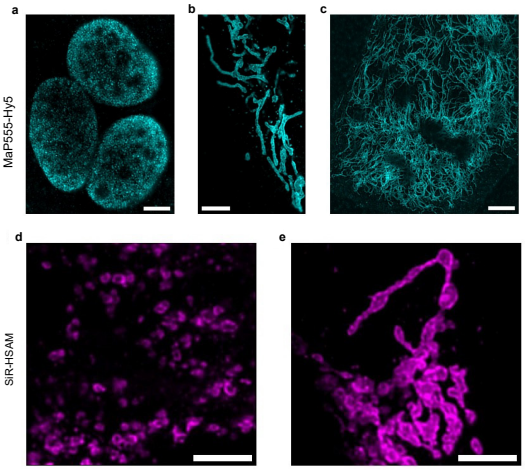


Figure 5.8: **3rd-order SOFI of other structures labeled with MaP555-Hy5.** **(a)** U2OS H2B-dHT7 labeled with 10 nM MaP555-Hy5. **(b)** U2OS TOM20-dHT7 labeled with 50 nM MaP555-Hy5. **(c)** U2OS VIM-dHT7 labeled with 20 nM MaP555-Hy5. **(d)** Lamp1-HT7 labeled with 20 nM SiR-HSAM. **(e)** TOM20-HT7 labeled with 100 nM SiR-HSAM. Scale bar 5 μm

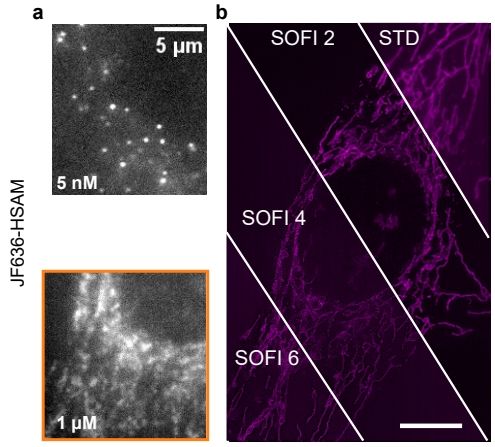


Figure 5.9: **xHTL JF-636 labeled U2OS TOM20-HT7** **(a)** Comparison of emitter density at two different xHTL concentrations. **(b)** Up to 6th-order SOFI reconstruction at 1 μM concentration. Decorrelation results: 274 nm for 2nd-order SOFI, 154 nm for 4th-order SOFI, and 83 nm for 6th-order SOFI. Scale bar 10 μm.

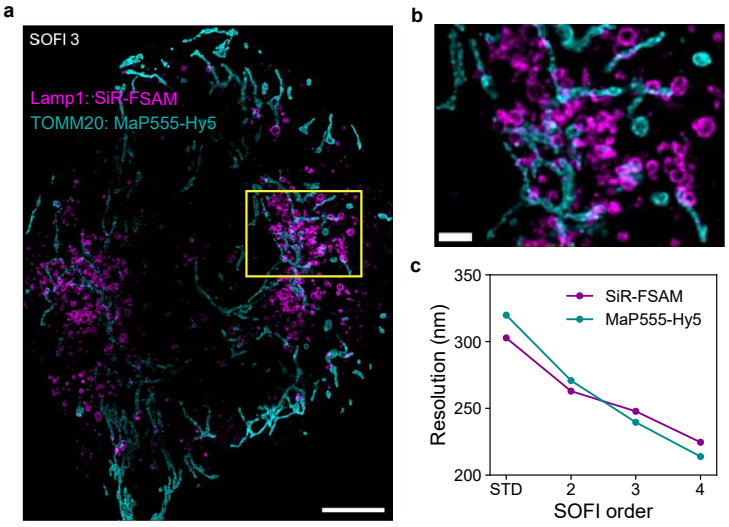


Figure 5.10: **Dual-color SOFI reconstruction of fixed U2OS sample with TOM20-dHT7 (labeled with 20 nM MaP555-Hy5) and Lamp1-HT7 (labeled with 10 nM SiR-FSAM)**, for the purpose of validating dual-target labeling for live cells. **(a)** 3rd-order SOFI reconstruction. Scale bar 10 μm. **(b)** Zoom-in of ROI highlighted in (a), scale bar 2 μm. **(c)** Resolution estimation by decorrelation analysis for each of the two acquired channels.

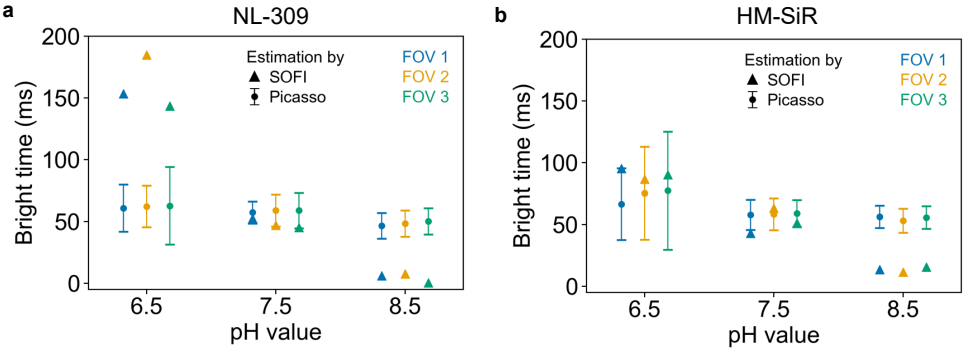


Figure 5.11: **On-time quantification for NL-309 fluorophores labeling TOM20-HT7 structures in fixed cells**, in imaging buffers with different pH values. **(a)** NL-309. **(b)** HM-SiR. Results from correlation-based on-time analysis of SOFI software and qPAINT analysis of Picasso software were compared. Averages and standard deviations (error bars) were calculated from 3 FOVs for each pH condition.

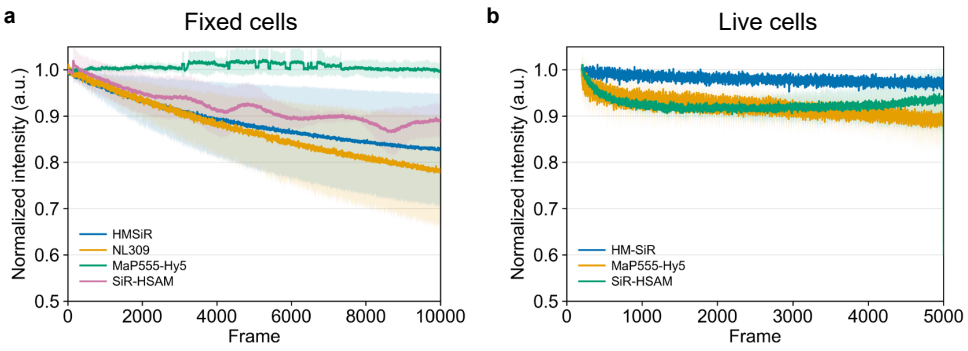


Figure 5.12: Comparison of bleaching curves of xHTLs and SBFs in **(a)** fixed-cell and **(b)** live-cell imaging experiments. Average normalized signal intensity per frame with standard deviation from different regions of interest.

References

[1] T. Stephan, A. Roesch, D. Riedel, S. Jakobs, Live-cell STED nanoscopy of mitochondrial cristae, Scientific Reports 9, 12419 (2019). DOI: 10.1038/s41598-019-48838-2.

[2] W. Jahr, P. Velicky, J. G. Danzl, Strategies to maximize performance in STimulated Emission Depletion (STED) nanoscopy of biological specimens, Methods 174, 27–41 (2020). DOI: 10.1016/j.ymeth.2019.07.019.

[3] J. Kompa, J. Bruins, M. Glogger, J. Wilhelm, M. S. Frei, M. Tarnawski, E. D'Este, M. Heilemann, J. Hiblot, K. Johnsson, Exchangeable HaloTag Ligands for Super-Resolution Fluorescence Microscopy, J. Am. Chem. Soc. 145, 3075–3083 (2023). DOI: 10.1021/jacs.2c11969.

[4] S. Jang, K. K. Narayanasamy, J. V. Rahm, A. Saguy, J. Kompa, M. S. Dietz, K. Johnsson, Y. Shechtman, M. Heilemann, Neural network-assisted single-molecule localization microscopy with a weak-affinity protein tag, Biophysical Reports 3, 100123 (2023). DOI: 10.1016/j.bpr.2023.100123.

[5] K. Grussmayer, T. Lukes, T. Lasser, A. Radenovic, Self-Blinking Dyes Unlock High-Order and Multiplane Super-Resolution Optical Fluctuation Imaging, ACS Nano 14, 9156–9165 (2020). DOI: 10.1021/acsnano.0c04602.

[6] K. L. Holland, S. E. Plutkis, T. A. Daugird, A. Sau, J. B. Grimm, B. P. English, Q. Zheng, S. Dave, F. Rahman, L. Xie, P. Dong, A. N. Tkachuk, T. A. Brown, R. H. Singer, Z. Liu, C. G. Galbraith, S. M. Musser, W. R. Legant, L. D. Lavis, A series of spontaneously blinking dyes for super-resolution microscopy, bioRxiv: The Preprint Server for Biology, 2024.02.23.581625 (2024). DOI: 10.1101/2024.02.23.581625.

[7] F. M. Jradi, B. P. English, T. A. Brown, J. Aaron, S. Khuon, J. A. Galbraith, C. G. Galbraith, L. D. Lavis, Coumarin as a general switching auxiliary to

prepare photochromic and spontaneously blinking fluorophores (2024). DOI: 10.1101/2024.05.12.593749.

[8] S. Wu, D. Hou, Q. Qiao, Z. Xu, Fluorescent dyes in the era of super-resolution imaging: new opportunities, challenges, and evolution, Chemical Society Reviews (2026). DOI: 10.1039/D5CS01304F.

[9] S. Geissbuehler, N. L. Bocchio, C. Dellagiacoma, C. Berclaz, M. Leutenegger, T. Lasser, Mapping molecular statistics with balanced super-resolution optical fluctuation imaging (bSOFI), Optical Nanoscopy 1, 1–7 (2012). DOI: 10.1186/2192-2853-1-4.

[10] M. S. Frei, M. Tarnawski, M. J. Roberti, B. Koch, J. Hiblot, K. Johnsson, Engineered HaloTag variants for fluorescence lifetime multiplexing, Nature Methods 19, 65–70 (2022). DOI: 10.1038/s41592-021-01341-x.

[11] Y. M. Sigal, R. Zhou, X. Zhuang, Visualizing and discovering cellular structures with super-resolution microscopy, Science 361, 880–887 (2018). DOI: 10.1126/science.aau1044.

[12] O. K. Wade, J. B. Woehrstein, P. C. Nickels, S. Strauss, F. Stehr, J. Stein, F. Schueder, M. T. Strauss, M. Ganji, J. Schnitzbauer, H. Grabmayr, P. Yin, P. Schwille, R. Jungmann, 124-Color Super-resolution Imaging by Engineering DNA-PAINT Blinking Kinetics, Nano Letters 19, 2641–2646 (2019). DOI: https://doi.org/10.1021/acs.nanolett.9b00508.

[13] L. Le, S. K. Sreenivas, E. Fort, S. Lévêque-Fort, Brightness demixing for simultaneous multi-target imaging in 3D single-molecule localization microscopy (2025). DOI: 10.1101/2025.03.02.639924.

[14] A. Descloux, K. S. Grussmayer, A. Radenovic, Parameter-free image resolution estimation based on decorrelation analysis, Nature Methods 2019 16:9 16, 918–924 (2019). DOI: 10.1038/s41592-019-0515-7.

[15] B. Moeyaert, W. Vandenberg, P. Dedecker, SOFIevaluator: a strategy for the quantitative quality assessment of SOFI data, Biomedical Optics Express 11, 636–648 (2020). DOI: 10.1364/BOE.382278.

[16] N. Jolivet, G. Bertolin, Revealing mitochondrial architecture and functions with single molecule localization microscopy, Biology of the Cell 117, e2400082 (2025). DOI: 10.1111/boc.202400082.

[17] W. Zou, L. Yang, H. Lu, M. Li, D. Ji, J. Slone, T. Huang, Application of super-resolution microscopy in mitochondria-dynamic diseases, Advanced Drug Delivery Reviews 200, 115043 (2023). DOI: 10.1016/j.addr.2023.115043.

[18] Q. Chen, C. Jin, X. Shao, R. Guan, Z. Tian, C. Wang, F. Liu, P. Ling, J.-L. Guan, L. Ji, F. Wang, H. Chao, J. Diao, Super-Resolution Tracking of Mitochondrial Dynamics with An Iridium(III) Luminophore, Small 14, e1802166 (2018). DOI: 10.1002/smll.201802166.

[19] Y. Han, M. Li, F. Qiu, M. Zhang, Y.-H. Zhang, Cell-permeable organic fluorescent probes for live-cell long-term super-resolution imaging reveal lysosome-mitochondrion interactions, Nature Communications 8, 1307 (2017). DOI: 10.1038/s41467-017-01503-6.

[20] S. Chen, J. Wang, D. Guan, B. Tan, T. Zhai, L. Yang, Y. Han, Y. Liu, Q. Liu, Y. Zhang, Near-Infrared Spontaneously Blinking Fluorophores for Live Cell Super-Resolution Imaging with Minimized Phototoxicity, Analytical Chemistry 96, 10860–10869 (2024). DOI: 10.1021/acs.analchem.4c02445.

[21] W. Chi, Q. Qiao, C. Wang, J. Zheng, W. Zhou, N. Xu, X. Wu, X. Jiang, D. Tan, Z. Xu, X. Liu, Descriptor ΔGC-O Enables the Quantitative Design of Spontaneously Blinking Rhodamines for Live-Cell Super-Resolution Imaging, Angewandte Chemie 59, 20215–20223 (2020). DOI: 10.1002/anie.202010169.

6

Discussion and Outlook

6.1. Balancing trade-offs in super-resolution microscopy: leverage biochemistry and technology

At the very beginning of Chapter 1, I described an ideal microscope. In reality, modern microscopy techniques excel in some features but fall short in others. We face the trade-offs between gains in spatial resolution, temporal resolution, contrast, and sample health, known as the pyramid of frustration, when presented with the many varieties of microscopy techniques offered today. Ultimately, the choice of method depends on the application and the biological and biomedical questions to be answered, and on what information should be obtained from samples through microscopic imaging. Scrutinizing the strengths and limitations of different methods and playing the strategy game wisely by balancing the trade-offs are hence crucial to maximize the amount and accuracy of information attainable.

The work in this dissertation is motivated by the long-standing insufficiency in throughput, temporal resolution and sample health of single molecule localization microscopy. The improvements were made by addressing two intertwined steps: sample labeling and data processing. Employment of novel fluorescent labels enabled inherently faster fluctuation analysis of SOFI (Chapter 3) or conventional SMLM (Chapter 4), and SOFI in turn enabled applications of blinking fluorophores suitable for live-cell imaging under gentle conditions (Chapter 5). In this section, I will reweigh the gains and losses and identify challenges and opportunities for the proposed methods.

Combining techniques can sometimes bring benefits from both worlds, as we saw in Chapter 3, which presents the synergy of DNA-PAINT and SOFI. Our approach of increasing single molecule microscopy throughput and temporal resolution comes at the compromise of spatial resolution; however, with a conscious and tunable balance depending on the application. At 6th-order, SOFI matches in spatial resolution to what is routinely achievable in SMLM. At lower orders, resolution is inferior; however, acquisition time is accelerated by up to 300 times compared to SMLM, with the exact factor adjustable by modulating buffer composition and the number of frames acquired. This serves as an example of the trade-off between spatial and temporal resolution for single molecule microscopy, as well as an example of how combining techniques offers extra room for maneuver. The adaptive resolution of our method is elegantly enabled by buffer

exchange, a simple approach that can be applied to any other blinking mechanisms responsive to buffer composition, including concentrations and pH. This can be further combined with sequential imaging workflows for multiplexing. It is worth noting that the method is not restricted to 2D. 3D imaging through multi-plane, where the fluorescence fluctuation in volume can be captured simultaneously, is applicable for DNA-PAINT-SOFI as well.

To further increase acquisition speed and SOFI order and extend the spatiotemporal resolution parameter space, we could first turn to fluorescent labels with favorable features. Looking back at the history of fluorescence super-resolution microscopy technique development, one can correlate how fluorophore and labeling techniques advance imaging techniques. For example, it was not until a decade after the theoretical principle of SMLM was proposed that multiple experimental implementations of SMLM emerged [1]. In the intervening years, photochromatic properties of fluorescent proteins were discovered, leading to the realization of PALM [2]. More switchable fluorescent labels and corresponding SMLM methods quickly followed, notably FRET-pair organic dyes for STORM [3], and transiently binding labels for PAINT [4]. The continuous development of fluorescent labels keeps fueling and enriching the fluorescent microscopy methodology advances, as shown in Chapter 3 where the speed-optimized DNA-PAINT sequence was proven to be the key to unlocking high-order SOFI, and in Chapter 5 where the exchangeable Halotag ligands enables analogue of DNA-PAINT-SOFI for live cells.

DNA-PAINT is an excellent experimental platform for single molecule microscopy, having shown spatial resolution rivaling that of electron microscopy and a simple multiplexing scheme by sequential imaging. The infinite possibilities in DNA sequences, and separation of the fluorescent chromophore and specific labeling of molecules of interest, contribute significantly to the currently increasing trends in novel labels for single molecule microscopy. Although the majority of those labels are proposed and optimized for SMLM conditions, SOFI could benefit as much. One type of label of interest is the fluorogenic and self-quenching imagers, which tackle the background noise problem in DNA-PAINT [5–7]. In the context of SOFI, the cross-pixel cumulant calculation does have an optical sectioning effect to an extent; however, the background noise from the diffusing imager could not be entirely averaged within an exposure time, thus adding the enhanced correlation signal falsely. Another undesirable time-variant component of fluorescence can arise from photobleaching. The resistance to photobleaching that DNA-PAINT has received recognition for is now under question, since the large reservoir of imager strands cannot compensate for the loss of light-induced reactive oxygen species (ROS) damaging to the docking strands [8]. This can be mitigated by carefully tuning the excitation light dose, as part of SOFI optimization. Recent studies proposed a buffer that effectively extends DNA-PAINT imaging time, which could also improve SOFI quality even with the shortest acquisition [9, 10]. Generally, photostable and high-contrast fluorescent labels, being pursued by biochemists for both oligonucleotide and spontaneously-blinking dyes nowadays, are worth trying for SOFI.

The physical size of fluorescent probes induces labeling errors and fundamentally restricts the spatial resolution. HaloTags and antibodies attached to proteins of interest, as used in this dissertation, typically have a size between 10 – 15 nm. According to the Nyquist sampling threshold, this means spatial resolution less than 20 to 30 nm is

impossible due to steric hindrance. Fluorescent molecules and labeling systems with smaller linkage errors, for example, generic code expansion followed by amino acid labeling, and shorter docking strand sequence in general for DNA-PAINT, are necessary to achieve resolution below the 10 nm barrier in SMLM. For SOFI, which operates at lower spatial resolution, this consideration is not immediately relevant. Instead, one needs to carefully assess any new labeling systems if the chromophores are isotropic dipoles at reduced size and confined structural geometry, as anisotropic radiation invalidates the assumption of a Gaussian-shaped PSF and deteriorates SOFI post-processing. In continuously labeled systems, i.e., non-transiently binding labels, it has also been reported that energy transfer between adjacent fluorophores blurs the PSF for SMLM. For SOFI, this invalidates the assumption of independent blinking and could be challenging to correct.

Reflecting on what constitutes high-order SOFI, sufficient sampling of the blinking statistics is at the core. Rapidly blinking fluorophores run through the storyline of this dissertation, essentially decreasing the number of frames needed for the same statistics. Rational design paired with exhaustive search is so far the common strategy for developing fast-blinking labels. For example, recent work expanded the number of rapidly repeating sequences by changing the chirality of DNA molecules [11]. Another example is engineering mismatches for different DNA strands to bind to the same handle with appropriate kinetics, in recent work on mRNA imaging using MINFLUX [12]. Technology like SPARXS could change entirely how we screen fluorescent labels in favor of certain features in a far more efficient way (Chapter 4). Beyond the search for accelerated kinetics, SPARXS can potentially specify any kinetics and spectroscopic property suitable for any imaging modality, such as the aforementioned fluorogenicity, longer on-time for tracking, and so on. However, we still need a more robust workflow to select sequences suitable for imaging in the cellular setting from the high-throughput results of SPARXS.

Another promising avenue for SOFI is spontaneously-blinking dyes. We have begun benchmarking a few of them for SOFI in Chapter 5, and the literature has identified more with kinetics too rapid for SMLM but promising for SOFI [13]. Yet another emerging blinking mechanism is reversible rhodamine-binding proteins, which is attractive for live-cell imaging [14]. In combination with advanced deconvolution and machine learning algorithms, which have been shown to further decrease the frame number to below 100, it is foreseeable that the throughput of super-resolution imaging will be pushed to new highs [15, 16].

One limiting factor that arises as imaging speed increases is camera exposure time and associated readout time. Large chip-based highly-sensitive sCMOS cameras are now standard in single molecule imaging. In order to obtain the high SNR crucial for the resolution enhancement for both SMLM and SOFI, camera exposure time needs to be long enough to capture as much as possible of the limited photon budget and is rarely below 10 to 20 ms. Event based sensors (EBS) could be revolutionary for detection in microscopy. Instead of registering fluorescence signal as an intensity, EBS detects only the change in the fluorescence and operates at a much faster rate compared to wide-field cameras. It has been demonstrated to increase throughput by detecting dense emitters for SMLM [17], and we are yet to see its application in SOFI. The unique data from EBS,

as point clouds registering blinking events in a 2D map instead of frames, requires extra pre-processing before inputting into SOFI. At the same time, it also provides new possibilities for classification in multiplexed imaging.

In short, SOFI's ability to speed up super-resolution imaging depends on the properties of fluorescent labels, which need identification, characterization, and optimization as they evolve. Together with new technologies and algorithms, we see more opportunities in the future towards the goal of fast, multiplexed live-cell resolution imaging.

6.2. Open microscopy as the platform for next-generation smart microscopy

Microscopy technology today comes with hardware and software hand in hand. After eyepieces were replaced by cameras, and manual positioning of samples was replaced by motorized precision stages, highly automated microscopes are on the rise for next-generation imaging. In smart microscopy, human intervention is minimized during imaging, and the parameters of hardware components are adjusted automatically according to feedback from images analyzed on the fly [18]. Highlighted target-driven or event-driven microscopy, where a predefined feature in the sample image triggers adaptive imaging parameters such as laser power or magnification, is particularly useful for biological imaging in high-throughput screening applications. In Chapter 3, we proposed a workflow for target-driven microscopy. An automated microfluidic system for DNA-PAINT buffer exchange could switch from low-resolution fast scanning to high-resolution detailed imaging upon the occurrence of a rare phenotype. The decision to change the buffer can also be facilitated by artificial intelligence. This task, on the one hand, requires advanced imaging analysis algorithms such as rapid segmentation and classification; on the other hand, it demands full access to the control of microscope hardware and auxiliary devices. This enhances the value of open microscopy beyond cheaper alternatives to commercial counterparts.

Development of smart microscopy involves effort in microscope hardware, control software, interface layer, experimental logic and user interfaces, demanding interdisciplinary expertise [19]. The diversity in bio-imaging tasks means each smart microscopy implementation needs customization and is difficult to transfer to other microscopes. I built Open Blink (Chapter 2) for single molecule super-resolution imaging used in this dissertation, taking into consideration hardware and software that could be reusable and extendable in the future. This is why Open Blink was integrated μManager which supports a wide range of devices and is programmable to integrate modular image analysis tools through Python. Additionally, the large amount of data generated by high-throughput imaging from Open Blink is essential for training adaptive microscopy using deep learning.

Open Blink stands on the shoulders of several other open projects. We have gladly received positive feedback from the open microscopy community, which is beginning to influence the broad population of microscopy users by advocating accessible hardware, standardized microscopy control application programming interfaces (APIs), image data formats and metadata. Challenges present ahead for this community as technological complexity and demands in life sciences grow, identified by Hohlbein

et al. in [20]. Among those challenges, Open Blink and its potential proliferation might encounter a lack of long-term support and an underestimation of the time and effort required for development in the future, considering its setting in a research lab focusing on methodology and/or biology. The first challenge could be tackled by thorough documentation and instructions as we attempted. The second one calls for alignment of goals from the developers and users, in which scenario having a stable working microscope alongside a duplicate dedicated for fast prototyping, for example implementing new devices and adaptive imaging pipelines, can be beneficial.

6.3. Concluding remarks

Super-resolution imaging enriches our understanding of life sciences and has numerous potential applications in biomedical and therapeutic research, and is therefore worth investing in improvements in every aspect. This dissertation presented methodologies for the increase of throughput in single molecule super-resolution microscopy, and a democratized tool for single molecule microscopy in general. It is a smaller step forward towards the goal of high-resolution, high-throughput live cell imaging, accessible to the broad bioimaging community. By adventuring with novel fluorescent labels, I have demonstrated the vast potential of SOFI in high-throughput multiplexed live-cell super-resolution imaging, which has been the central challenge for light microscopy. To raise awareness and usage of SOFI, it is crucial to develop and optimize fluorescent labels with suitable photophysical properties either by design or by discovery. This calls for an accessible framework to both implement and evaluate the SOFI reconstruction algorithm. As a computationally intensive method, SOFI involves pre- and post-processing steps currently fragmented and duplicated in various software platforms in need of clear instructions. Democratizing software is the next step after opening the hardware to fully exploit SOFI's potential.

Looking further ahead, imaging with high temporal-spatial resolution at greater scale is key to discoveries in biology and medicine. This dissertation did not address tissue imaging or imaging extended over days to weeks, which remain directions for future work in the longer term. Such endeavors might involve fluorescent labels very different from what has been discussed here, or not involving them at all; the large amount of data would call for AI-assisted microscopy automation. The high-throughput super-resolution imaging methods presented in this work, including instrumentation and concepts, lay a foundation and hopefully encourage more collaborative efforts across disciplines to develop imaging techniques.

References

[1] E. Betzig, Proposed method for molecular optical imaging, Optics Letters 20, 237–239 (1995). DOI: 10.1364/OL.20.000237.

[2] S. T. Hess, T. P. Girirajan, M. D. Mason, Ultra-High Resolution Imaging by Fluorescence Photoactivation Localization Microscopy, Biophysical Journal 91, 4258 (2006). DOI: 10.1529/BIOPHYSJ.106.091116.

[3] M. J. Rust, M. Bates, X. Zhuang, Sub-diffraction-limit imaging by stochastic optical reconstruction microscopy (STORM), Nature Methods 2006 3:10 3, 793–796 (2006). DOI: 10.1038/nmeth929.

[4] A. Sharonov, R. M. Hochstrasser, Wide-field subdiffraction imaging by accumulated binding of diffusing probes, Proceedings of the National Academy of Sciences of the United States of America 103, 18911–18916 (2006). DOI: 10.1073/PNAS.0609643104.

[5] S. Stoller, A. Jha, J. Bewersdorf, F. Schueder, Fluorogenic speed-optimized DNA-PAINT probes enable super-resolution imaging of whole cells, bioRxiv (2026). DOI: 10.64898/2026.03.23.710523.

[6] L. F. Kessler, A. Balakrishnan, N. S. Deußner-Helfmann, Y. Li, M. Mantel, M. Glogger, H.-D. Barth, M. S. Dietz, M. Heilemann, Self-quenched Fluorophore Dimers for DNA-PAINT and STED Microscopy, Angewandte Chemie International Edition 62, e202307538 (2023). DOI: 10.1002/anie.202307538.

[7] A. Ghosh, M. Meub, D. A. Helmerich, S. Doose, M. Sauer, Fast, whole-cell DNA-PAINT imaging with dual-labeled self-quenched imager probes, bioRxiv (2023). DOI: 10.1101/2023.10.09.561472.

[8] P. Blumhardt, J. Stein, J. Mücksch, F. Stehr, J. Bauer, R. Jungmann, P. Schwille, Photo-Induced Depletion of Binding Sites in DNA-PAINT Microscopy, Molecules 2018, Vol. 23, Page 3165 23, 3165 (2018). DOI: 10.3390/MOLECULES23123165.

[9] C. Liang, Q. Li, B. Chen, T. Zhai, X. Luo, Y. Yang, J. Qian, D. Zhao, S. Luo, F. Wang, Q. Li, J. Shen, C. Fan, Reactive oxygen species–resistant ultrastable super-resolution DNA framework dots, Proceedings of the National Academy of Sciences 123, e2514438123 (2026). DOI: 10.1073/pnas.2514438123.

[10] R. T. Perelman, G. M. Church, J. Stein, A simple, ultrastable, and cost-effective oxygen-scavenging system for long-term DNA-PAINT imaging, bioRxiv (2025). DOI: 10.1101/2025.07.14.664726.

[11] E. M. Unterauer, E.-M. Schentarra, I. Pachmayr, T. Tashrin, J. Kwon, S. Strauss, K. Jevdokimenko, R. Kowalewski, F. Opazo, E. F. Fornasiero, L. A. Masullo, R. Jungmann, Left-handed DNA for efficient highly multiplexed imaging at single-protein resolution, Nature Communications 16, 8773 (2025). DOI: 10.1038/s41467-025-64228-x.

[12] A. Passera, P. Welzl, A. Gomez-Segalas, C. Plaschka, F. Balzarotti, Super-resolved imaging of mRNA ultrastructure in cells, bioRxiv (2026). DOI: 10.64898/2026.01.23.701081.

[13] K. L. Holland, S. E. Plutkis, T. A. Daugird, A. Sau, J. B. Grimm, B. P. English, Q. Zheng, S. Dave, F. Rahman, L. Xie, P. Dong, A. N. Tkachuk, T. A. Brown, R. H. Singer, Z. Liu, C. G. Galbraith, S. M. Musser, W. R. Legant, L. D. Lavis, A series of spontaneously blinking dyes for super-resolution microscopy, bioRxiv: The Preprint Server for Biology, 2024.02.23.581625 (2024). DOI: 10.1101/2024.02.23.581625.

[14] J. Kompa, L. J. Dornfeld, N. Porzberg, S. Jang, S. Zedlitz, S. H. Lilje, C. Catapano, D. Jocher, L. Merk, C. Hoege, R. Mao, J. Wilhelm, M. S. Dietz, M. Tarnawski, J. Hiblot, A. A. Hyman, M. Heilemann, K. Johnsson, Fast, Bright, and Reversible Fluorescent Labeling of Rhodamine-Binding Proteins, Journal of the American Chemical Society 148, 1419–1429 (2026). DOI: 10.1021/jacs.5c18083.

[15] M. Tekpınar, J. Komen, H. Valenta, **R. Huo**, K. d. Zwaan, P. Dedecker, N. Tomen, K. Grußmayer, Enabling Real-Time Fluctuation-Based Super Resolution Imaging, bioRxiv (2026). DOI: 10.1101/2025.06.05.658028.

[16] W. Zhao, S. Zhao, Z. Han, X. Ding, G. Hu, L. Qu, Y. Huang, X. Wang, H. Mao, Y. Jiu, Y. Hu, J. Tan, X. Ding, L. Chen, C. Guo, H. Li, Enhanced detection of fluorescence fluctuations for high-throughput super-resolution imaging, Nat. Photon. 17, 806–813 (2023). DOI: 10.1038/s41566-023-01234-9.

[17] C. Cabriel, T. Monfort, C. G. Specht, I. Izeddin, Event-based vision sensor for fast and dense single-molecule localization microscopy, Nature Photonics 17, 1105–1113 (2023). DOI: 10.1038/s41566-023-01308-8.

[18] A. Rates, J. B. Passmore, N. Norlin, L. C. Kapitein, Smart microscopy: adaptive microscope control to improve the way we see life, npj Imaging 4, 14 (2026). DOI: 10.1038/s44303-026-00145-y.

[19] L. Hinderling, H. S. Heil, A. Rates, P. Seidel, P. S. Kesavan, M. Gunkel, B. Diederich, T. Guilbert, R. Torro, O. Bouchareb, C. Demeautis, C. Martin, S. Brooks, E. Sisamakis, E. Grandgirard, J. Mutterer, H. Oatman, J. Toettcher, A. Rogov, N. Antonovaite, K. Johansson, J. K. Ahnlinde, O. André, P. Nordenfelt, P. Nordenfelt, C. Pfander, J. Reymann, T. Lambert, M. R. Cosenza, J. O. Korbel, R. Pepperkok, L. C. Kapitein, O. Pertz, N. Norlin, A. Halavatyi, R. Camacho, Smart microscopy: current implementations and a roadmap for interoperability, Methods in Microscopy (2026). DOI: 10.1515/mim-2025-0029.

[20] J. Hohlbein, B. Diederich, B. Marsikova, E. G. Reynaud, S. Holden, W. Jahr, R. Haase, K. Prakash, Open microscopy in the life sciences: quo vadis?, Nature Methods 19, 1020–1025 (2022). DOI: 10.1038/s41592-022-01602-3.

Summary

Super-resolution microscopy (SRM) techniques based on single molecule bypass the diffraction limit in light imaging and facilitate visualization of cellular organization at the nanometer scale, which have driven many breakthroughs in life science. Despite the high spatial resolution, their application in biological research is hampered by the low throughput and temporal resolution, particularly burdening imaging *in vivo*. In addition, the high cost and technical complexity of single molecule super-resolution microscopy instrumentation hinder their wider adoption. Therefore, it is important to improve both the methodology and accessibility for super-resolution microscopy.

In **Chapter 1**, I briefly review the history and principles of single-molecule based microscopy, namely single molecule localization microscopy (SMLM) and super-resolution fluctuation imaging (SOFI). Both methods are enabled by the stochastic blinking of fluorescent labels, whose mechanisms are discussed. SOFI gains enhancement of spatial resolution via correlation analysis of fluorescence fluctuations instead of rigorous localization of single molecules as in SMLM, thus an inherently faster and gentler imaging method tolerant of a wide range of blinking behaviors and kinetics. Recent advancements in various types of fluorescent probes, with properties of faster blinking or live-cell compatibility, can be combined with SOFI to address the challenges in super-resolution microscopy.

A comprehensive open-source imaging platform named Open Blink for 2D single-molecule imaging is presented in **Chapter 2**. Open Blink provides the essential hardware setup for high-quality, high-throughput single-molecule imaging, with its high-power quad-line homogeneous illumination, total internal reflection fluorescence (TIRF) compatibility, a large field of view, and the ability to maintain axial focus over hours. The microscope body is constructed based on an open frame and efforts were made to fully integrate the control and image acquisition into open software μManager. Open Blink not only serves all the imaging tasks for this dissertation, but also brings unprecedented accessibility for SRM with ultra-low cost, easy implementation, use, and maintenance.

To increase the single molecule imaging throughput, we combine oligonucleotide labels, as used in DNA points accumulation for imaging in nanoscale topography (DNA-PAINT) with SOFI in **Chapter 3**. The synergy between the two methods is first validated by the successful rendering of high-resolution SOFI using speed-optimized DNA-PAINT labels. We exploit the versatility of DNA hybridization kinetics with DNA-PAINT labels and achieved 30-300-fold faster imaging with SOFI compared to conventional SMLM, albeit with lower resolution. Notably, by tuning the image medium composition and data processing, this method allows a flexible switch between high-throughput SOFI and super-resolution SMLM, thereby demonstrating adaptive spatial-temporal resolution tailored to different imaging needs.

In search of DNA-PAINT labels with hybridization rates suited for single molecule SRM,

current technologies are incapable of accurately predicting the kinetics from the sequence. In **Chapter 4**, we utilize a powerful technique named SPARXS (Single molecule Parallel Analysis for Rapid eXplora-on of Sequence space) linking kinetics to sequence in high throughput. With SPARXS, we characterize the hybridization rates of 128 sequences in parallel, leading to the discovery of a new sequence for fast DNA-PAINT that outperforms current standards.

To extend the high-throughput SRM method to imaging *in vivo*, we begin to explore the live-cell compatibility provided by enzymatic labeling of HaloTags and spontaneously-blinking fluorophores (SBFs), in **Chapter 5**. Two-color live-cell SOFI is enabled by the new class of fluorescent labels with a novel blinking mechanism which we systematically optimize by adjusting imaging medium and acquisition parameters. We also suggest expanding the throughput by kinetics and brightness multiplexing using the quantitative capability of SOFI.

Lastly, in **Chapter 6**, I discuss the strengths and limitations of the high-throughput super-resolution microscopy methods presented in this dissertation, and evaluate factors driving their further advancement.

Samenvatting

Superresolutiemicroscopietechnieken (SRM) die gebaseerd zijn op de detectie van individuele moleculen omzeilen de diffractielimiet van optische beeldvorming en maken het mogelijk om de cellulaire organisatie op nanometerschaal te visualiseren. Deze technieken hebben daarmee aan de basis gestaan van talrijke doorbraken binnen de levenswetenschappen. Ondanks hun hoge ruimtelijke resolutie wordt de toepassing ervan in biologisch onderzoek beperkt door de lage doorvoersnelheid en temporele resolutie, hetgeen met name beeldvorming *in vivo* bemoeilijkt. Daarnaast vormen de hoge kosten en technische complexiteit van instrumentatie voor superresolutiemicroscopie op basis van individuele moleculen een belemmering voor grootschalige toepassing. Het is daarom van belang om zowel de methodologie als de toegankelijkheid van superresolutiemicroscopie verder te verbeteren.

In **Hoofdstuk 1** geef ik een beknopt overzicht van de historische ontwikkeling en de principes van microscopietechnieken gebaseerd op individuele moleculen, in het bijzonder single-molecule localization microscopy (SMLM) en super-resolution optical fluctuation imaging (SOFI). Beide methoden maken gebruik van het stochastische knippergedrag van fluorescente labels; de onderliggende mechanismen hiervan worden eveneens besproken. In tegenstelling tot SMLM, waarbij afzonderlijke moleculen nauwkeurig worden gelokaliseerd, verkrijgt SOFI een verbeterde ruimtelijke resolutie door middel van correlatieanalyse van fluctuaties in fluorescentie-intensiteit. Hierdoor is SOFI intrinsiek een snellere en minder belastende beeldvormingsmethode, die bovendien tolerant is voor een breed scala aan knippergedragingen en -kinetieken. Recente ontwikkelingen op het gebied van verschillende typen fluorescente probes, waaronder probes met snellere knipperkinetiek of compatibiliteit met levende cellen, kunnen met SOFI worden gecombineerd om belangrijke uitdagingen binnen de superresolutiemicroscopie aan te pakken.

In **Hoofdstuk 2** presenteer ik Open Blink, een uitgebreid open-source beeldvormingsplatform voor tweedimensionale beeldvorming van individuele moleculen. Open Blink biedt de essentiële hardware voor hoogwaardige beeldvorming van individuele moleculen met een hoge doorvoersnelheid. Het systeem beschikt onder meer over krachtige, homogene belichting met vier golflengten, compatibiliteit met total internal reflection fluorescence (TIRF)-microscopie, een groot beeldveld en de mogelijkheid om de axiale focus gedurende meerdere uren stabiel te houden. De microscoop is opgebouwd rond een open frame, waarbij bijzondere aandacht is besteed aan de volledige integratie van de besturing en beeldacquisitie in de open-source software μManager. Open Blink wordt niet alleen gebruikt voor alle beeldvormingsexperimenten binnen dit proefschrift, maar vergroot tevens de toegankelijkheid van SRM aanzienlijk dankzij de zeer lage kosten en het gemak waarmee het systeem kan worden opgebouwd, gebruikt en onderhouden.

Om de doorvoersnelheid van beeldvorming op het niveau van individuele molecu-

len te verhogen, combineren we in **Hoofdstuk 3** oligonucleotidelabels, zoals toegepast in DNA points accumulation for imaging in nanoscale topography (DNA-PAINT), met SOFI. De synergie tussen beide methoden wordt in eerste instantie aangetoond door de succesvolle reconstructie van SOFI-beelden met hoge resolutie met behulp van voor snelheid geoptimaliseerde DNA-PAINT-labels. Vervolgens benutten we de veelzijdigheid van DNA-hybridisatiekinetiek om met DNA-PAINT-labels in combinatie met SOFI een 30- tot 300-voudig hogere beeldvormingssnelheid te realiseren dan met conventionele SMLM, zij het ten koste van de ruimtelijke resolutie. Door de samenstelling van het beeldvormingsmedium en de gegevensverwerking aan te passen, maakt deze methode bovendien een flexibele omschakeling mogelijk tussen SOFI met hoge doorvoersnelheid en SMLM met hoge ruimtelijke resolutie. Daarmee biedt de methode een adaptieve afweging tussen ruimtelijke en temporele resolutie, afgestemd op uiteenlopende beeldvormingsbehoeften.

Bij de zoektocht naar DNA-PAINT-labels met hybridisatiesnelheden die geschikt zijn voor SRM op het niveau van individuele moleculen, vormt het ontbreken van methoden waarmee deze kinetiek nauwkeurig uit de DNA-sequentie kan worden voorspeld een belangrijke beperking. In **Hoofdstuk 4** maken we gebruik van SPARXS (Single molecule Parallel Analysis for Rapid eXploration of Sequence space), een krachtige techniek waarmee op grote schaal relaties tussen sequentie en kinetiek kunnen worden onderzocht. Met behulp van SPARXS karakteriseren we parallel de hybridisatiesnelheden van 128 sequenties. Dit leidt tot de identificatie van een nieuwe sequentie voor snelle DNA-PAINT die betere prestaties levert dan de huidige standaardsequenties.

Om de ontwikkelde SRM-methode met hoge doorvoersnelheid uit te breiden naar beeldvorming *in vivo*, onderzoeken we in **Hoofdstuk 5** de mogelijkheden voor beeldvorming in levende cellen door middel van enzymatische labeling van HaloTags en spontaan knipperende fluorescente kleurstoffen (spontaneously blinking fluorophores; SBFs). Deze nieuwe klasse fluorescente labels, die wordt gekenmerkt door een nieuw knippermechanisme, maakt tweekleuren-SOFI in levende cellen mogelijk. We optimaliseren deze beeldvorming systematisch door zowel de samenstelling van het beeldvormingsmedium als de acquisitieparameters aan te passen. Daarnaast stellen we voor om de doorvoersnelheid verder te vergroten door multiplexing op basis van kinetiek en fluorescentie-intensiteit, waarbij gebruik wordt gemaakt van de kwantitatieve mogelijkheden van SOFI.

Tot slot bespreek ik in **Hoofdstuk 6** de sterke punten en beperkingen van de in dit proefschrift gepresenteerde methoden voor superresolutiemicroscopie met hoge doorvoersnelheid. Tevens evalueer ik de factoren die bepalend zijn voor de verdere ontwikkeling en toepassing van deze methoden.

Epilogue

In studying life, you keep diving from higher levels to lower ones,
until somewhere along the way, life fades out, leaving you empty-handed.

Albert Szent-Györgyi

I could not ignore the inconsistency in my use of terms such as *fluorophores, fluorescent labels, probes, emitters, markers, tags*, and so on throughout this thesis, which reflects my uncertainty about their roles in microscopy and about microscopy as a methodology. As with any experimental technique, we need to interpret carefully what we detect and measure with microscopes. For fluorescent microscopy, the question of fidelity arises as we introduce foreign molecules to the molecules of interest in the hope of converting the molecular behavior into photons. Every step in the process could fail. The labeling could have errors. The labels could alter the structures or interactions. The light could perturb. The optics could be aberrated. The detection could be noise-prone. The image reconstruction could be assumptive. Fortunately, every step can be controlled, calibrated, and uncertainty estimated and reduced to some extent. The more we understand about the chain from targets to labels and then to images, the more exploitable the labels are, as demonstrated by numerous methods using their lifetime, polarization, and so on. Although many studies examine the effect of labels on biological characterization in general, I found fewer that discuss it for super-resolution imaging beyond linkage error, and even fewer that validate it beyond using the super-resolution imaging methods they focus on. Nevertheless, since this thesis is restricted to morphologic visualization, where linkage error is the most concerning factor, I would like to point interested readers to the literature for this topic (Cuevas-Galindo & Jiménez-Sánchez, *Front. Photonics*, 2026; Erdmann et al., *Cell Chem. Biol.*, 2019; Ries et al., *Nat. Methods*, 2012; Thevathasan et al., *Nat. Methods*, 2019).

Meanwhile, I also notice the excessive use of words like *see, show, and observe*, which seems only natural when describing what we measure under a microscope. However, Ed

Young points out in his wonderful book on animal senses *An Immense World*, that the language we use to describe the world is shaped by our senses and in turn shapes how we sense:

> *Our species and our culture are so driven by sight that even people who are blind from birth will describe the world using visual words and metaphors... Even when scientists describe senses that humans lack altogether, like the ability to detect electric fields, they talk about images and shadows.*

Are we biased in believing what we see from a microscope is part of the reality of the specimen because visual information dominates our perception? Even accounting for label-induced errors, we seem to assume microscopic images are like camera photographs, producing something similar to what we would have seen with our bare eyes if we could. Advances in microscopy instrumentation and analysis now encourage the development of probes that translate other physical signals such as neuronal electricity into visual signals. We seem to have a bright future where labels and microscopy help each other's growth, but do we trust this approach to studying the complexity of life?

I was able to find an answer in the writings of Ian Hacking, an experimental realist, who already pointed to the direction of correlative microscopy before the blooming age of GFPs (Hacking, *Do We See Through a Microscope? Pac. Philos. Q.*, 1981; *Representing and Intervening, Cambridge Univ. Press*, 1983). Confidence in the images we produce should be earned by independent cross-validations, and more importantly, according to Hacking, from intervention. Perhaps this is not surprising for microscopists who are already on their way to optogenetics and optical tweezers. For super-resolution microscopy in general, the more detail we see, the more precisely we need to understand how the details are produced. This brings my questioning to a close while opening the imagination to the *in vivo* biological application this thesis still calls for.

Acknowledgments

This dissertation would not have been possible without the generous help I have received over the past years. To those whose names I have not been able to mention here, please know that your help and generosity are no less appreciated!

First, I would like to thank the committee members for their valuable feedback and assessment. **Kristina, Jörg, Johannes** and **Sjoerd**, it is my pleasure to have you on my committee after being influenced by your research directly or indirectly over the years. **Chirlmin**, thank you for being my promotor and offering your insights and encouragement throughout my PhD, which has been a source of inspiration.

Kristin, it is a privilege to become the first PhD student you graduate, and to have the opportunity to witness some milestones in both your career and family. From the first few times we talked during my interview, I knew I could trust you to offer a helping hand when needed, and you did. You always bring warmth and kindness to the people around you, and I really appreciate your effort to keep the group a supportive place to do research. Thank you!

The work presented here has benefited greatly from my collaborations with remarkable scientists. **Carolien**, thank you for your effort to make the project possible so quickly. I have enjoyed your efficiency and clarity in the process. **Myron** and **Hylkje**, I am a little less illiterate in biology because of your guidance. **Julian Kompa** and **Christian Niederauer**, thank you for generously sharing your experiences and materials which saved me a lot of time and trouble.

The Grußmiauers, the old and the new generations, my time during the PhD was enjoyable because of you. **Moritz**, thank you for coming up with the best name for the microscope and letting me steal it, and more importantly, for being a considerate and understanding office and lab mate from the start. I'm grateful for the many times I could walk out of the darkness of the optics lab knowing you were next door willing to help. **Miyase**, my go-to expert for computational questions, you make things happen no matter how difficult. I'm glad to have you around and work alongside you. **Arty**, I admire your determination to make a change, and I miss the artistic creativity you brought to the office. **Nicole**, I wish I had your impressive wetlab skills and I'm just as happy knowing my cells were the happiest in your hands. **Sjoukje, Karin, Stein** and **Tommasso**, you are the ones who remind me daily to remain curious and optimistic; the energy and joy you have brought to the group make it even harder now to say goodbye. **Sinan, Hannah Lena, Tim, Gijs, Phil, Filip, Marianne** and **Sabrina**, I'm happy to have shared with each of you a part of the memories at KG lab.

Klarinda, Mara, Jelle and **Anaïs**, I am lucky to have you as students and interns. I hope you have learned as much as I have learned from you. Thank you for your contributions

and for the delightful time we spent working together.

Catia, Dimitri de Roos, Wiel Evers, Roland Kieffer, and **Esther Plomp**, I have benefited enormously from your expertise, from cell biology and data management to electronics and mechanics. Each of you is exceptional at what you do, and your knowledge helped me solve many of the puzzles I encountered.

I feel lucky to have the nicest colleagues around at the Bionanoscience department. The group of Stan Brouns (**Rita, Alicia, Daan, Aswin, Desi, Sam, Halewijn, Anna, Dani, Stan, Nadiia, Jelger**), I will miss our countless lunches, cakes, coffees, and walks in our office corner. Some of you share my frustration with the lack of tables to have lunch at, but all the funny or interesting lunch conversations with you made up for eating from our laps. **Phuong**, the smiles and snacks you spare me brightened my days. **Fan**, I have taken home every quick meal hack I learned from you during our encounters at the microwave. **Angelica**, every time I had a lab supply emergency, you saved me. **Agathe**, **Christos** and **Dimphna**, thank you for making BN welcoming by sharing lab meetings and lab spaces when I started post-Covid rather clueless.

My fellow microscopists in Delft, from the group of Bernd Rieger and Sjoerd Stallinga at ImPhys, and the group of Carlas Smith at ME, you certainly make Delft arguably the best city to do research on microscopes besides the one obvious reason. **Shih-Te**, thank you for showing me your alignment tricks; your dedication truly motivated me. **Wenxiu**, you filled the microscopy conferences and our trips with so much joy with your unbeatable humor and your warmest heart. **Yutong** and **Huangcheng**, how many times have we ran into each other at de Doelen or Concertgebouw! It made riding the packed train home together much merrier. **Isabel**, one of my first memories of Delft is sitting on the back of your bike on a snowy night, after you kindly adopted me into your company at the first faculty event I went to. **Dimitri**, thanks for including me in the optics lab meetings and all the discussions which are missed in my faraway building on campus. **Yabin** and **Qingru**, always a delight to catch up with you at the seminars or socials. You have all made the journey less lonely.

Despite often being negative about where I'm living because of the lack of nature, I'm deeply grateful that this place has connected me with wonderful people. **Jaime, Asif, Stephani** and **Surabhi**, how nice that our paths crossed again; you bring back the close-knit connections in Europhotonics which I missed. **Deniz, Rinze, Jani** and **David**, thank you for making me feel at home at Mice Palace and for having the most immediate helping hand and listening ear, and for some of the best laughs. **Valentin**, I complain less about the Dutch landscapes thanks to you introducing cycling to me and being a reliable human GPS. **Lemeng** and **Dongying**, you both created my little piece of Herland where I could speak my thoughts without worry while enjoying making Chinese food with you. **Gina**, not only do you inspire me musically, but you made me believe in myself in a way I couldn't see. **Erik**, special thanks for your company and support, you hear my silent notes. **Liu**, you showed me what it means to be true to oneself; words won't suffice to express how grateful I am for your friendship.

最后，感谢爸爸妈妈一直以来无条件的爱、理解与支持，让我放心走过漫长的求学岁月。你们始终是我最温暖的依靠。

Curriculum Vitæ

Ran HUO

26 January 1997	Born in Lu'an, China.
2014–2018	B.Sc. in Applied Physics Hefei University of Technology, Hefei, China
2019–2021	M.Sc. in Optics and Photonics (Erasmus Mundus Joint Master's Degree *Europhotonics*) – Aix-Marseille University, Marseille, France (2019) – Karlsruhe Institute of Technology, Karlsruhe, Germany (2020) – Polytechnic University of Catalonia, Barcelona, Spain (2021)
2022–2026	Ph.D. Delft University of Technology, Delft, The Netherlands Title: "High-throughput Super-resolution Microscopy Using Novel Fluorescent Labels" Promotor: Prof. dr. C. Joo Copromotor: Dr. K. S. Grußmayer

List of Publications

4. C. Bastiaanssen, **R. Huo**, P. Irmisch, A. Sivaraman, R. Seidel, K. S. Grußmayer, and C. Joo, Multiplexed sequence-resolved screening of transient DNA hybridization for programmable nanotechnology. (Submitted)

3. **R. Huo**, J. Komen, M. Engelhardt, A. Millot, J.Extermann, and K. Grußmayer, Open Blink: Low-cost TIRF microscopy for super-resolution imaging via μManager. (Under revision)

2. M. Tekpınar, J. Komen, H. Valenta, **R. Huo**, K. de Zwaan, P. Dedecker, N. Tomen, and K. Grußmayer, A Lightweight Deep Learning Framework for Fast, Real-Time Super-Resolution Fluctuation Imaging. Biophysical Reports 6 (2026).

1. K. de Zwaan* ,**R. Huo***, M. N. F. Hensgens, H. L. Wienecke, M. Tekpınar, H. Geertsema, and K. Grußmayer, High-Throughput Single-Molecule Microscopy with Adaptable Spatial Resolution Using Exchangeable Oligonucleotide Labels, ACS Nano 19 (2025).

* Denotes equal contribution



ISBN 978-94-6518-424-1